The Pennsylvania State University

The Graduate School

College of Earth and Mineral Sciences

ILLUMINATING BASINAL FLUID FLOW IN EUGENE ISLAND 330 (GULF OF MEXICO) THROUGH *IN SITU* OBSERVATIONS, DEFORMATION EXPERIMENTS, AND HYDRODYNAMIC MODELING

A Thesis in

Geosciences

by

Beth Bishop Stump

Submitted in Partial Fulfillment
of the Requirements
for the Degree of

Master of Science

December 1998

_____

Beth Bishop Stump

We approve the thesis of Beth Bishop Stump.

Date of Signature

_____ _____

Peter B. Flemings
Associate Professor of Geosciences
Thesis Advisor

_____ _____

Derek Elsworth
Associate Professor of Mining Engineering

_____ _____

Terry Engelder
Professor of Geosciences

_____ _____

Lee R. Kump
Associate Professor of Geosciences
Associate Head for Graduate Programs and Research

_____ _____

Mark D. Zoback
Professor of Geophysics, Stanford University
Special Signatory

_____ _____

Daniel E. Karig
Professor of Geological Sciences, Cornell University
Special Signatory

Abstract

Porosity is a predictor of fluid pressure in young, rapidly-deposited basins. Uniaxial strain experiments on uncemented samples provide information about the strain history of these basins. In the Eugene Island 330 area (offshore Louisiana) porosity-predicted fluid pressures in muds differ from *in situ* measurements in adjacent sands. Deformation experiments on mud samples from this area reveal a history of uni-directional strain (e.g. increasing effective stress). These experimental results imply that effective stress has not decreased (e.g. fluid pressure has not increased) following compaction, and, therefore, porosity should be an accurate indicator of *in situ* fluid pressure. In this analysis, observed differences between porosity-predicted pressures and *in situ* measurements are interpreted as real pressure differences between adjacent sand and mud layers. Two physical models describe the origin of these observed pressure differences. Rapid burial can cause the fluid pressure in a dipping, permeable sand to differ from pressure in the surrounding low-permeability mud. During steady burial, fluid expelled from low-permeability mud will preferentially flow through a dipping, high-permeability sand. Fluid flows from the more highly pressured mud into the sand at the structural low and from the sand into the surrounding mud at the structural high. Both the rapid-loading and steady-flow mechanisms generate pressure differences between a dipping sand lens and the surrounding mud.

Table of Contents

List of Figures

List of Tables

Acknowledgments

Many people have shaped my academic life and I would like to recognize them and thank them for helping me get this far. Joe Madri, at Yale Comprehensive Cancer Center, was the first to show me that research can, at times, be both tremendously frustrating and incredibly rewarding. Tom Ackerman and John Cahir convinced me that Penn State was the right place for me to pursue an undergraduate degree and both continued to guide and encourage me throughout my stay here.

I thank Eric Barron for hiring me to run climate simulations, even though I had no workstation experience, and I thank Bill Peterson, Jim Leous, and Jeff Buechler for teaching me everything I know about Unix. Trudy Campbell, Dick Andre, Jim Beer, Laurel Alexander, Kent Rinehart, and John Austin taught me valuable lessons about geology, seismic, and well data. I thank them for not only their time and support of my thesis work, but also for showing me the scientific appeal of a career in the oil industry.

I thank my committee members and special signatories for taking an active role in my thesis research. Discussions with Mark Zoback aided in my understanding of basin-scale pressure and stress relationships. Dan Karig has been an invaluable resource. He not only conducted all of the deformation experiments, but also taught me how to relate experimental data to geologic deformation. Derek Elsworth patiently answered numerous questions about soil compaction and fluid flow. Terry Engelder taught me many lessons about pressure and stress and his critical review of this thesis has improved it markedly.

My research benefited greatly from discussions with Glenn Bowers, Martin Traugott, Jim Niemann, Thomas Finkbeiner, and Brandon Dugan. Heather Johnson helped type up some of the Appendices.

My parents, Paul and Nancy Bishop, have provided unconditional support throughout my academic career and I recognize that I could not have achieved success without them.

Throughout the five years that I have known my advisor, Peter Flemings, he has continued to surprise and amaze me with his boundless energy and quest for deeper scientific understanding of a myriad of problems. Peter has helped me accomplish things that I did not think were possible. I thank him for his endless patience, his sage advice, and his friendship.

Finally, I thank my husband, Brad, for his love and support, and for never once complaining about all of the time I spent working on my research.

This research was funded by Gas Research Institute, the P.D. Krynine Fund, and a fellowship from Exxon Production Research Company.

CHAPTER 1
Introduction

OVERVIEW

Undercompaction is a significant source of overpressure in young rapidly-deposited basins (Dickinson, 1953; Bredehoeft and Hanshaw, 1968; Bethke, 1986). During rapid burial, low-permeability prevents mud from expelling fluids at a sufficient rate to dissipate excess pressure. Upon burial, other mechanisms may increase fluid pressure. Late-stage pressure generation mechanisms include aquathermal pressuring (Barker, 1972), hydrocarbon maturation (Barker, 1990), and clay dehydration (Powers, 1967; Burst, 1969). Gordon and Flemings (1998) developed a model to quantify the contributions of various mechanisms in the Eugene Island 330 area. Overpressure due to undercompaction comprised 80 - 94% of the total, depending upon the assumed deformation behavior of the soil matrix.

Many previous authors have characterized the relationship between porosity and fluid pressure (Athy, 1930; Terzaghi and Peck, 1948; Rubey and Hubbert, 1959). Commonly, porosity-predicted fluid pressures in muds are compared with *in situ* measurements in sands. Differences between porosity-derived predictions and measurements can be interpreted in two ways. First, the porosity model may be failing to accurately predict *in situ* fluid pressure. Failure of the porosity model has been attributed to late-stage increases in fluid pressure which are not recorded in the porosity signature (Scott and Thomsen, 1993; Bowers, 1994; Hart et al., 1995). Second, the observed differences could

represent actual pressure differences between sands and muds.

In this thesis, I extend work on this problem by first examining the relationship between fluid pressure in muds and sands in an overpressured field (Chapter 2). I then use uniaxial strain experiments on these muds to further understand the deformation history of this area.

In Chapter 2, I present an analysis of fluid pressures in muds and adjacent sands for fifteen wells in the Eugene Island 330 area. I document fluid pressure differences between sands and muds and draw implications for fluid flow. Two physical models, rapid-loading and steady-flow, describe the generation of the pressure differences observed in this field. I apply these models specifically to three overpressured sands and discuss conceptual models for the evolution of pressure in these sands.

In order for porosity to accurately record *in situ* pressure, sediments must have undergone a history of uni-directional strain (e.g. increasing effective stress). Chapter 3 details results of uniaxial strain experiments on sand and mud samples from this area. Experimental results on the mud samples indicate that effective stress has not decreased significantly at depth. This result implies that late-stage pressure generation mechanisms have not contributed significantly to the overpressuring of these sediments. Therefore, porosity should be an accurate indicator of fluid pressure.

A second result of the deformation experiments that relates back to the models for pressure evolution is the estimation of mud permeability. Direct laboratory measurements at *in situ* levels of effective stress yielded mud permeability estimates on the order of 10^{-19} m^2 (10^{-4} mD). Estimates of permeability are used to determine the time-scales of pressure

diffusion.

DESCRIPTION OF FIELD AREA

The focus of this study was the Eugene Island 330 field. The Eugene Island 330 (E.I. 330) field (Figure 1.1) is located in the Gulf of Mexico, 272 km (169 mi) southwest of New Orleans at a water depth of 77 m (253 ft). The E.I. 330 area is a prolific oil and gas field. Recoverable reserves have been estimated at 307 million bbl hydrocarbon liquids and 1.65 tcf of gas (Holland et al., 1990). More than 270 wells have been drilled in the 9 block study area since 1971. The extent of drilling activity in this area makes it conducive for scientific study, because of the multitude of data available. Well logs, pressure surveys, drilling reports, and conventional core samples provided the data used in these analyses.

The E.I. 330 area is a salt-withdrawal minibasin (Alexander and Flemings, 1995) comprised of interbedded Plio-Pleistocene sands and muds. Preferential removal of salt from beneath this basin generated structural relief on the stratigraphically deeper sands. The strata record a progradational history. The deepest sand discussed in this paper, the Lentic 1, was deposited in a proximal deltaic environment (Alexander and Flemings, 1995). The Lentic 1 sand lacks laterally continuity and is overlain by a thick marine mud. These two characteristics contributed to the severe overpressuring of this sand. The OI-1 and JD sands are laterally-extensive, permeable, prodelta deposits (Alexander and Flemings, 1995) which record moderate overpressure.

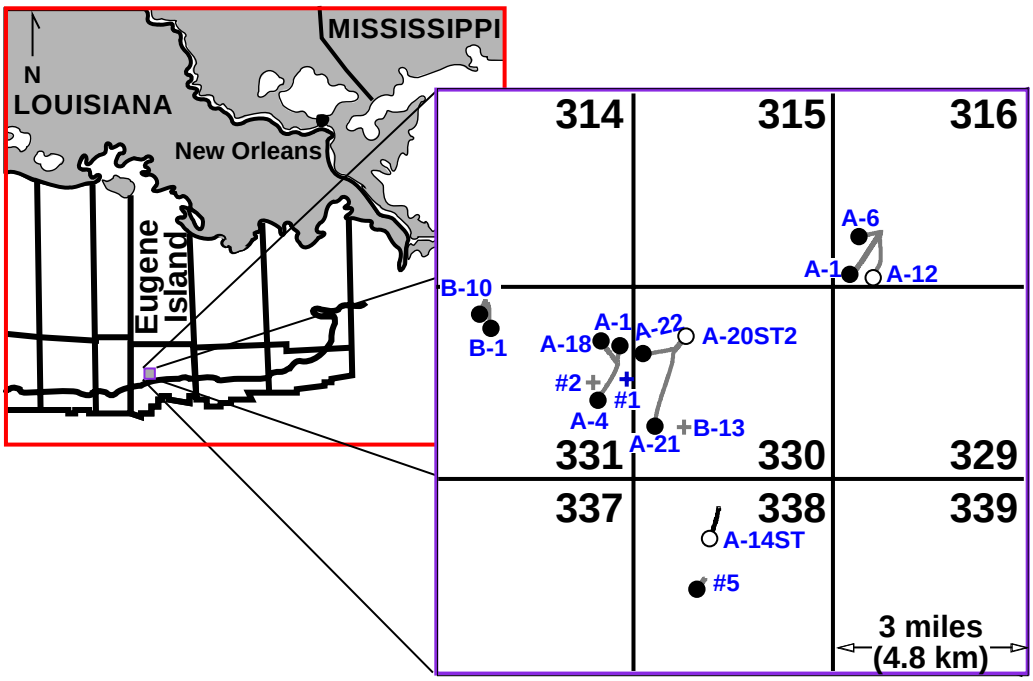

Figure 1.1: The Eugene Island 330 area is located in the Gulf of Mexico, on the outer continental shelf. Basemap locates all of the wells used in these analyses. Filled circles denote the wells analyzed for porosity and pressure (Chapter 2); empty circles represent wells from which core was taken and used in deformation experiments (Chapter 3).

REFERENCES

Alexander, L.L. and P.B. Flemings, 1995, Geologic evolution of a Plio-Pleistocene salt-withdrawal minibasin: Eugene Island block 330, offshore Louisiana: American Association of Petroleum Geologists Bulletin, v. 79, p. 1737-1756.

Athy, L.F., 1930, Density, porosity, and compaction of sedimentary rocks: American Association of Petroleum Geologists Bulletin, v. 14, p. 1-22.

Barker, C., 1972, Aquathermal pressuring - role of temperature in development of abnormal-pressure zones: American Association of Petroleum Geologists Bulletin, v. 56, p. 2068-2071.

Barker, C., 1990, Calculated volume and pressure changes during the thermal cracking of oil to gas in reservoirs, American Association of Petroleum Geologists Bulletin, v. 74, p. 1254-1261.

Bethke, C.M., 1986, Inverse hydrologic analysis of the distribution and origin of Gulf Coast-type geopressured zones, Journal of Geophysical Research, v. 91, p. 6535-6545.

Bowers, G.L., 1994, Pore pressure estimation from velocity data: Accounting for overpressure mechanisms besides undercompaction: Society of Petroleum Engineers, SPE 27488, p. 515-529.

Bredehoeft, J.D., Hanshaw, B.B., 1968, On the maintenance of anomalous fluid pressures: 1. Thick sedimentary sequences, Geological Society of America Bulletin, v. 79, p. 1097-1106.

Burst, J.F., 1969, Diagenesis of Gulf Coast clayey sediments and its possible relation to petroleum migration: AAPG BUlletin, v. 53, p. 73-93.

Dickinson, G., 1953, Geological aspects of abnormal reservoir pressures in Gulf Coast Louisiana: American Association of Petroleum Geologists Bulletin, v. 37, p. 410-432.

Gordon, D.S. and P.B. Flemings, 1998, Generation of Overpressure and Compaction-Driven Fluid Flow in a Plio-Pleistocene Growth-Faulted Basin, Eugene Island 330, Offshore Louisiana: Basin Research, v. 10, p. 177-196.

Hart, B.S., P.B. Flemings, and A. Deshpande, 1995, Porosity and pressure: Role of compaction disequilibrium in the development of geopressures in a Gulf Coast Pleistocene basin: Geology, v. 23, p. 45-48.

Holland, D.S., W.E. Nunan, and D.R. Lammlein, 1990, Eugene Island Block 330 field-U.S.A., offshore Louisiana, *in* E.A. Beaumont and N.H. Foster, eds. Structural traps III, tectonic fold and fault traps: American Association of Petroleum Geologists

Treatise of Petroleum Geology, Atlas of Oil and Gas Fields, p. 103-143.

Powers, M.C., 1967, Fluid release mechanisms in compacting marine mudrocks and their importance in oil exploration: AAPG BUlletin, v. 51, p. 1240-1254.

Rubey, W.W. and M.K. Hubbert, 1959, Overthrust belt in geosynclinal area of western Wyoming in light of fluid pressure hypothesis, 2: Role of fluid pressure in mechanics of overthrust faulting: Geological Society of America Bulletin, v. 70, p. 167-205.

Scott, D., and Thomsen, L.A., 1993, A Global Algorithm for Pore Pressure Prediction: Society of Petroleum Engineers, SPE 25674.

Terzaghi, K. and R.B. Peck, 1948, Soil mechanics in engineering practice: New York, John Wiley and Sons, Inc., 566 p.

CHAPTER 2

Overpressures in Sands and Bounding Muds in the Eugene Island 330 field (Offshore Louisiana, U.S.A.): Implications for Trap Integrity, Fluid Migration, and Borehole Stability

ABSTRACT

Porosity-predicted fluid pressures in overpressured Plio-Pleistocene muds of the Eugene Island 330 (E.I. 330) field (offshore Louisiana) differ from pressure measurements in adjacent sands. Observed pressure differences between a sand layer and the overlying mud change with position on structure. At structural highs, fluid pressure in the sand exceeds pressure in the adjacent mud; at structural lows, the relationship is reversed. Two physical models describe the origin of these pressure differences: rapid-loading and steady-flow. Rapid, differential burial of a high-permeability sand lens by low-permeability mud can generate pressure differences at the sand-mud interface. Alternatively, following slow, steady burial, fluid flow through a low-permeability mud is diverted into a dipping sand lens, such that at the structural low, fluid flows from the mud into the sand and at the structural high, fluid migrates from the sand into the adjacent mud. In either case, the magnitude of the fluid pressure difference between the dipping sand and the surrounding mud is dependent upon the three-dimensional geometry of the sand, total relief on structure, and the minimum principal stress of the bounding mud layer. Excess pressure generated in the sand by differential sediment loading could cause the fluid pressure in the sand to converge on the minimum principal stress in the mud and result in fracture-driven fluid flow.

INTRODUCTION

Porosity or some proxy of porosity (e.g. resistivity) has long been used to estimate *in situ* fluid pressure in young sedimentary basins (Athy, 1930; Rubey and Hubbert, 1959; Wallace, 1965; Hottman and Johnson, 1965; Eaton, 1975). Typically, workers examine the mud porosity profile in a zone of known fluid pressure (i.e. hydrostatic zone) and then use this empirical relationship to calculate fluid pressure from porosity in the overpressured zone. Fluid pressure predictions in the mud are then compared with measurements in sands.

In this paper, mud refers to unlithified sediments with high gamma ray response. Conventional core samples taken adjacent to the KE and Lentic 1 sands indicate that these sediments generally consist of approximately 40% quartz, 40 to 50% clay (primarily smectite and illite with lesser amounts of kaolinite and chlorite), and less than 10% plagioclase and potassium feldspar (Chapter 3). Grain sizes range from silt-clay sized particles (~80% by volume) to very fine-grained particles.

Previous studies have presented differences between predicted and measured pressures as a failing of the porosity model to estimate *in situ* pressure. Specifically, workers have interpreted differences between porosity-derived pressures and observed *in situ* pressures as late-stage increases in fluid pressure which were not recorded in the mud porosity signature. This effect, termed unloading because it results in a net decrease in effective stress, was investigated by Scott and Thomsen (1993) and Bowers (1994) and further explored by Hart et al. (1995) and Gordon and Flemings (1998). According to the unloading model, a late-stage decrease in effective stress does not result in decompaction (i.e. porosity rebound) along the initial compaction (porosity-effective stress) curve. As a result, the porosity-effective stress model does not successfully predict fluid pressures in sediments with this unloaded deforma-

tion path.

This study continues to explore the differences between predicted fluid pressures in muds and *in situ* fluid pressures in adjacent sands. Unlike previous work, we document pressure differences and explore the hypothesis that the observed differences are real. We present two models to describe the origin of these pressure differences: rapid-loading and steady-flow. In the rapid-loading model, sediment loading occurs so quickly that it is not possible for low-permeability muds to equilibrate with this loading. As a result, sharp pressure differences occur between the sand and the mud at the structural high and low. In the steady-flow model, vertical flow occurs in response to sediment loading. The permeability contrast between the sand and mud causes flow to be focused through the dipping sand. Once again, pressures in the sand at the structural high and low differ from pressures in mud at equivalent depths some distance from the sand. However, the pressure transition at the sand-mud interface is more gradual than predicted by rapid-loading.

We examine fluid pressures in mud predicted by the porosity-effective stress method with *in situ* fluid pressures measured in the reservoir sands of the Eugene Island 330 (E.I. 330) field. We show that the pressure regime in the mud adjacent to the deepest and most highly overpressured sand (Lentic 1) appears most compatible with the steady-flow model. A comparison of predicted pressure in the mud with *in situ* pressure measurements in the shallower OI-1 sand reveals a more complex behavior, suggesting a history of fluid migration and recharge.

We close by summarizing the implications of both theory and observation for the evolution of fluid flow. This understanding can be used to characterize hydrocarbon migration and entrapment as well as to recognize potential problems of drilling in overpressured strata.

THE ORIGIN OF PRESSURE DIFFERENCES BETWEEN SANDS AND MUDS

It has long been recognized that a permeable water-saturated sand encased in mud can have a different pressure than the adjacent mud (Dickinson, 1953; England, 1987; Mann and Mackenzie, 1990; Traugott and Heppard, 1994). Traugott and Heppard (1994) refer to the mechanism as the centroid effect. Below, we explore two theoretical models to understand this phenomenon: rapid-loading and steady-flow.

Rapid-Loading

Consider a sand which is buried slowly to 2042 m (6700 feet) (Figures 2.1a,b,c). Initially, burial rate is sufficiently slow to facilitate fluid expulsion and dissipation of excess pressure. If burial rate then increases significantly as the sand subsides differentially, the sand and mud become overpressured. When loading is very rapid, the mud will remain undrained and the fluid pressure increase in the mud will be lithostatic. The pressure gradient in the dipping, permeable sand will equilibrate to hydrostatic (Figure 2.1d). In both the sand and mud, the overpressure (DP*) is the pressure necessary to support the overburden load ($DP^* = P_f - P_h$). As shown in Appendix A, overpressure is a function of the overburden, and the fluid and bulk compressibility (Equation 2.1a,b). Table 2.1 defines all of the variables and constant used in this paper.

$$DP^*_{mud} = \left(\left(\frac{\beta}{\beta + \beta_f(1-\phi)}\right)\rho_b - \rho_f\right) g\,dz \qquad (2.1a)$$

$$DP^*_{sand} = \left(\left(\frac{\beta}{\beta + \beta_f(1-\phi)}\right)\rho_b - \rho_f\right) g \int_0^L z(x)\,dx \qquad (2.1b)$$

The key difference between Equations 2.1a and 2.1b is that the overpressure at any

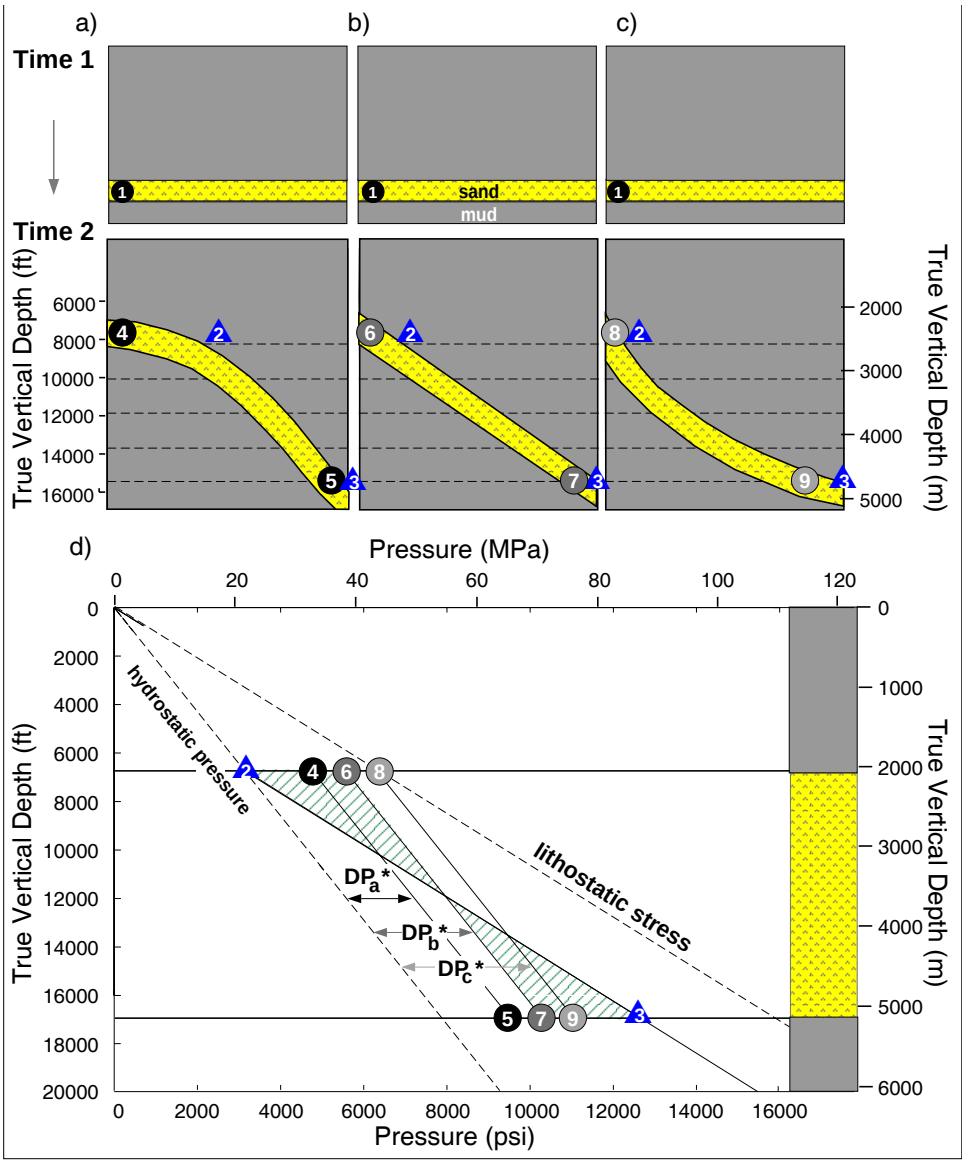

Figure 2.1: A sand is buried at a rate that allows it to completely dissipate fluids and remain hydrostatically pressured to a depth of 2042 m (6700 ft). The sand then subsides differentially and is rapidly buried to form three different structures: a) anticlinal, b) homoclinal, c) synclinal. Overpressure in the is a linear function of depth (Equation 2.1a), therefore overpressure contours (dashed lines) in the mud are horizontal. d) Fluid pressure from the surface to 2042 m is hydrostatic in both the sand and mud. Upon differential burial, fluid pressures in the sand diverge from pressures in the adjacent mud. Overpressure in the sand (DP*) is dependent on the overburden load (Equation 2.1b). Dashed lines represent hydrostatic pressure (10.5 MPa/km; 0.465 psi/ft) and lithostatic stress (21 MPa/km; 0.94 psi/ft). Circles 4,6,8 represent pressures in the sand at the structural highs; points 5,7,9 represent pressures in the sand at the structural lows. Triangles 2 and 3 represent fluid pressure in the mud at the structural high and low, respectively. Fluid pressure gradient in the mud is parallel to lithostatic stress gradient; the pressure gradient in the sands is hydrostatic.

Table 2.1: Nomenclature

Name	Description	Units
a	half-length of sand	L
b	half-thickness of mud layer	L
f	acoustic formation factor	dimensionless
g	gravitational acceleration	L/T^2
k	intrinsic permeability	L^2
L	length of sand	L
P^*_{md0}	initial overpressure in mud (fluid flow model)	M/LT^2
P^*_{mud}	overpressure in mud layer	M/LT^2
P^*_{sand}	overpressure in sand layer	M/LT^2
P^*_{sd0}	initial overpressure in sand (fluid flow model)	M/LT^2
P_f	fluid pressure	M/LT^2
P_g	gas phase pressure	M/LT^2
P_h	hydrostatic fluid pressure	M/LT^2
P_o	oil phase pressure	M/LT^2
P_w	water phase pressure	M/LT^2
q_x	horizontal flow velocity	L/T
q_z	vertical flow velocity	L/T
S_v	vertical (lithostatic) stress	M/LT^2
t	time	T
u	undisturbed velocity	L/T

Table 2.1: Nomenclature

v_x	horizontal flow velocity	L/T
v_z	vertical flow velocity	L/T
x	horizontal position	L
y	position in fluid flow model	L
z	depth	L
α	mud conductivity	M/T^3
β	matrix compressibility	LT^2/M
β_f	fluid compressibility	LT^2/M
β_s	grain compressibility	LT^2/M
Δt_{ma}	matrix travel time	T/L
Δt	wireline travel time	T/L
η	elliptical coordinate	dimensionless
λ	ratio of P_f to S_v	dimensionless
ϕ	wireline-derived porosity	L^3/L^3
ϕ_0	reference porosity	L^3/L^3
μ	fluid viscosity	M/LT
Θ	dip of sand lens	radians
ρ_b	bulk density	M/L^3
ρ_f	fluid density	M/L^3
σ_v	vertical effective stress	M/LT^2
ξ	elliptical coordinate	dimensionless
Ψ	stream function	L^2/T

point in the mud (DP^*_{mud}) is a function of the overlying load at that point (Equation 2.1a), while the overpressure in the sand (DP^*_{sand}) is controlled by the integrated area over the sand (Equation 2.1b). The overpressure cross-section predicted by the undrained instantaneous loading model consists of horizontal overpressure contours which abut against the dipping sand (Figure 2.1a,b,c). The rapid-loading model therefore predicts a pressure discontinuity at the sand-mud interface.

The magnitude of overpressure within the sand and the depth at which the fluid pressures in the sand and mud are equal are affected by the geometry of the overlying load (Figure 2.1d). A synclinal sand (Figure 2.1c) sustains more overpressure than an anticlinal sand (Figure 2.1a), because the synclinal sand supports a greater sediment load. As a result, the depth at which the sand and mud pressures are equal (termed the centroid depth by Traugott and Heppard, 1994) varies with structural geometry. The pressure difference between sand and mud changes with position on structure. At the structural high, fluid pressure in the sand is greater than pressure in the mud; at the structural low, pressure in the mud is greater than pressure in the sand.

Three-dimensional geometry also plays an important role in controlling the degree of overpressuring in sands. A three-dimensional dome structure (Figure 2.2b) sustains greater overpressure than a planar structure (Figure 2.2a) dipping at the same angle. Therefore, the centroid depth is deeper in the three-dimensional case (Figure 2.2c). In general, if a sand fans out downdip, the degree of overpressuring in the sand will be greater than if the sand width were constant. For example, Iliffe (1998) describes a situation where sheet geometry basin-floor sands merge updip with narrower channelized sands at structural highs. Loading of the

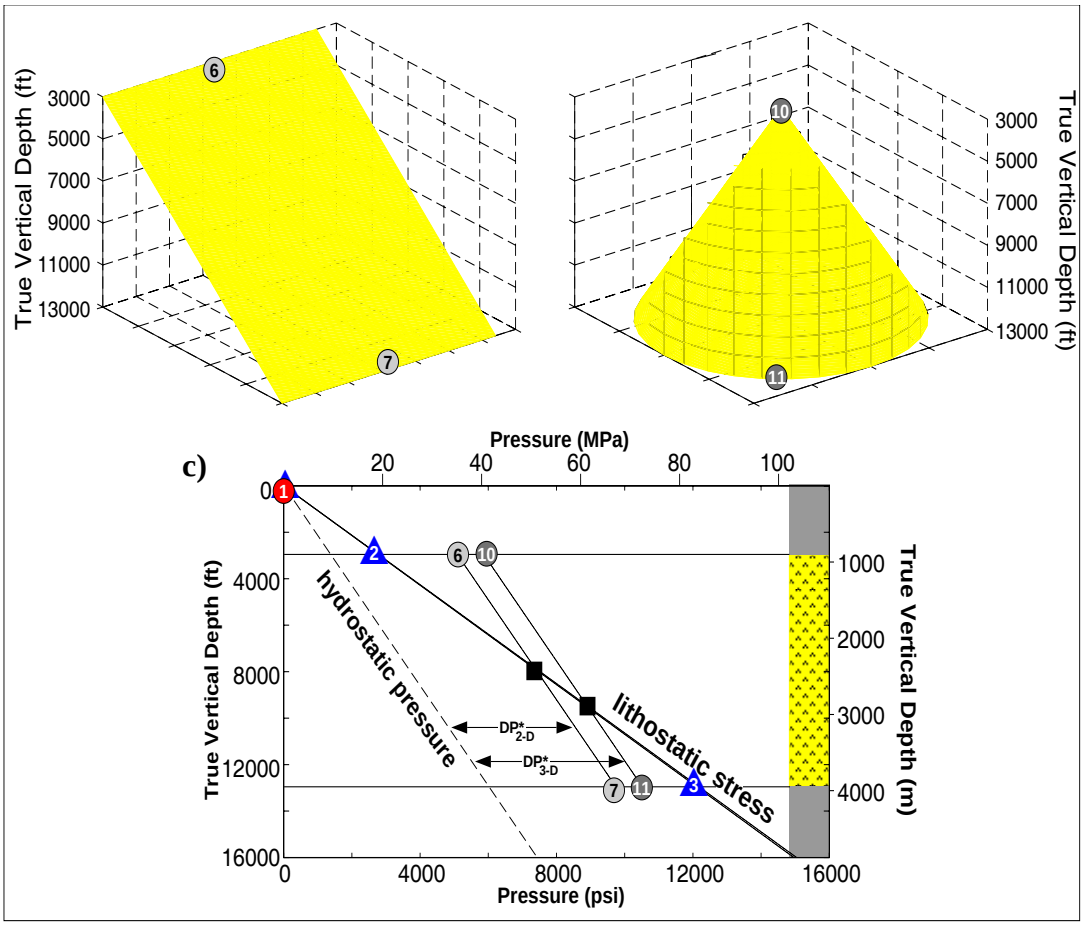

Figure 2.2: Three-dimensional geometry affects the pressure regime predicted by rapid-loading. a) The two-dimensional problem (Figure 2.1b) is shown as a planar structure in three dimensions. b) A three-dimensional structure with the same dip is shown as a dome. c) A greater pressure differential is generated at the structural high and the centroid depth is deeper for the dome-like structure. Circles 6 and 7 represent the fluid pressures in the planar sand; circles 10 and 11 denote fluid pressure in the dome-shaped sand.

sheet sands amplifies fluid pressure in the sand at the structural high.

One of the obvious results of this model is that rapid loading can cause the fluid pressure in the sand at structural highs to converge on the minimum principal stress of the overlying mud. If this occurs, fluid migrates out of the sand by fracture permeability. Finkbeiner (1998) and Finkbeiner et al. (in review) explore this phenomenon in the E.I. 330 field.

Steady-flow

We consider a similar geometry to that illustrated in Figure 2.2 (Figure 2.3). However, we now assume that flow is occurring through both the mud and the sand and that the sand permeability is much greater than mud permeability. Phillips (1991) presented a mathematical description of this problem. We extend this model and describe its implications for overpressured sands. Details are presented in Appendix B.

In steady vertical flow, if no sand is present, all of the flow is vertical and described by Darcy's Law. If a horizontal sand is present, the flow field is unchanged.

$$q_z = -\frac{k}{\mu}\frac{\partial}{\partial z}P^* \tag{2.2a}$$

$$q_x = -\frac{k}{\mu}\frac{\partial}{\partial x}P^*=0 \tag{2.2b}$$

However, the presence of a dipping and relatively more permeable sand lens results in a focusing of flow toward the sand at the structural low and away from the sand at the structural high (Figure 2.3a).

The vertical overpressure gradient ($\frac{\partial}{\partial z}P^*$) far from the sand is constant and described by Equation 2.2a. The constant gradient is illustrated by the evenly-spaced contour lines at the left and right margins of Figure 2.3b. However, close to the structural low, the pressure con-

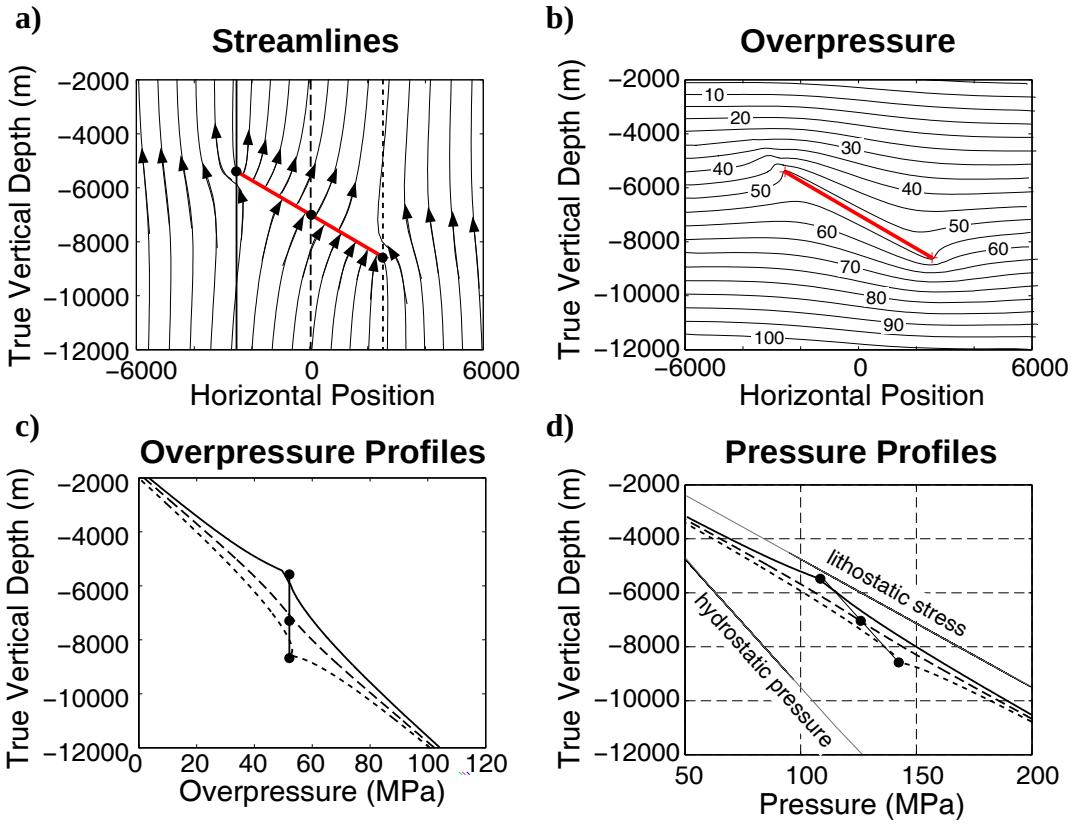

Figure 2.3: The steady-flow model (derivation: Appendix B) was run for a dipping permeable sand surrounded by low-permeability mud. a) Streamlines indicate primarily vertical flow, with enhanced flow into the sand lens at the structural low and out of the sand at the structural high. Thick vertical lines locate pressure profiles shown in parts c and d. b) Overpressure contours, which are horizontal in the mud far away from the sand, are elevated adjacent to the sand near the structural high; contours are depressed near the structural low. c) Profiles show the effect of the sand lens on overpressure in the adjacent mud at the structural high (solid line), midpoint (dashed line), and low (dotted line). Circles denote the intersection of the profile with the sand lens. Overpressure within the sand is constant, because the fluid pressure gradient is hydrostatic. d) The pressure profiles at three locations show that at the structural midpoint (dashed line), fluid pressure follows a lithostatic gradient, and is undisturbed by the presence of the sand lens. At the structural high (solid line), pressure increases sharply from the mud into the sand. At the structural low (dotted line), the fluid pressure increases from the sand into the underlying mud.

tours are depressed; at the structural high, they are elevated (Figure 2.3b). This pressure distribution focuses fluid into the sand at the structural low and out of the sand at the structural high (Figure 2.3a).

Three vertical pressure profiles extracted from the structural high, midpoint, and low demonstrate the effect of the sand lens on overpressure in the adjacent mud (Figure 2.3c). Overpressure in the sand is constant (e.g. hydrostatic pressure gradient). At the structural high (solid line), overpressure in the mud underlying the sand is greater than overpressure in the sand, indicating that fluid flows into the structural high. However, the gradient (i.e. slope of the overpressure-depth curve) in the underlying mud is much lower than the gradient in the overlying mud. Therefore, the net flow direction is from the sand to the mud. Likewise, at the structural low (dotted line), the overlying mud has a slightly lower overpressure, indicating minimal flow out of the sand. The underlying mud is significantly more overpressured than the sand at the structural low and therefore most of the flow is from the shale into the sand.

Profiles at the three structural positions show the effect of the dipping sand lens on the pressure gradient in the mud adjacent to the sand (Figure 2.3d). At the structural midpoint (dashed line), the fluid pressure in sand and mud are equal. The pressure gradient is constant and described by Equation 2.2a. At the structural high (solid line), the pressure gradient in the mud increases until it intersects the sand and then decreases below the sand. In contrast, at the structural low, the pressure gradient in the mud decreases above the sand. In the mud beneath the sand, the pressure gradient increases until it converges on the gradient predicted by Equation 2.2a.

The magnitude of the difference between fluid pressure in the sand at the structural high and the pressure in the mud far away from the sand is identical to that presented for the

rapid-loading case.

$$P^*_{sand}\Big|_{\text{structural high}} - P^*_{mud}\Big|_{\text{structural high}} = \rho_f g\left(\frac{\text{vertical relief}}{2}\right) \quad (2.3)$$

We have modeled only the effect of a sand dipping at a constant angle. However, we can qualitatively predict the behavior for a more complex geometry, as explored in Figures 2.1 and 2.2 for the rapid-loading model. If the sand has a synclinal geometry, a greater surface area of the sand is exposed to more overpressured muds beneath the structural midpoint, and, similar to the rapid-loading case, the sand sustains a greater overpressure. In contrast, if the sand is anticlinal, it sustains less overpressure. The argument is identical for three-dimensional structures. As in Figure 2.2, domed structures generate greater overpressures than planar structures with equivalent dips. Furthermore, if the sand geometry pinches toward the structural high, as Iliffe (1998) observed, then greater overpressure will be present in the sand.

Comparison of the two models

The two models presented here can be viewed as end member cases. Following rapid deposition, the pressure regime is described by the rapid-loading model and there are abrupt differences in fluid pressure at the sand-mud interface. Conversely, following slow, steady burial, the pressure distribution is predicted by the steady-flow model. Pressure diffusion generates a pressure boundary layer around the sand lens.

Time-Scales of Pressure Diffusion

We can better understand the extent of pressure evolution in this area by assessing the time-scales of pressure diffusion. A simple fluid flow model simulates pressure dissipation from an analytical solution to a diffusion equation which is based on Darcy's Law (Appendix

C). In this model, conductivity in the mud is a function of permeability, porosity, fluid density and viscosity and fluid and matrix compressibility. Mud permeability is difficult to estimate *in situ*, but laboratory experiments on mud samples from the E.I. 330 area (Chapter 3) indicate a mud permeability of 3.2×10^{-16} m^2 (3.2×10^{-4} mD). Gordon and Flemings (1998) estimate permeability as a function of porosity for the E.I. 330 area, and calibrate their porosity-permeability relationship in order to replicate the observed pressure regime. They estimate a permeability of 1.7×10^{-21} m^2 (1.7×10^{-6} mD) for a mud with 25% porosity. Neuzil's (1994) mud permeability values for the Gulf of Mexico range from 5×10^{-22} m^2 (5×10^{-7} mD) to 1×10^{-19} m^2 (1×10^{-4} mD) for 25% porosity.

Results from our fluid flow model, run with typical mud permeability, help us to assess the extent of pressure diffusion in this area over the time-scale of basin evolution. The model predicts that for a permeability of 10^{-21} m^2 (10^{-6} mD), after 1.5 M.y., pressure differences still exist between adjacent sand and mud layers (Figure 2.4). Some of the overpressure from the sand has dissipated into the mud, creating a gradual pressure decline from the sand-mud interface to the center of the mud layer. However, the overpressure at the center of the mud remains less than the overpressure in the sand, due to the low permeability of the mud (Figure 2.4b).

Other authors have suggested that relative permeability effects such as 'capillary seal' are necessary to impede flow and prevent fluid pressures in adjacent layers from equilibrating (Shosa and Cathles, 1996). Our model results suggest that intrinsic mud permeability on the order of 10^{-21} m^2 (10^{-6} mD), typical of observations of Gulf Coast muds, is sufficiently low to maintain fluid pressure differentials between sands and muds.

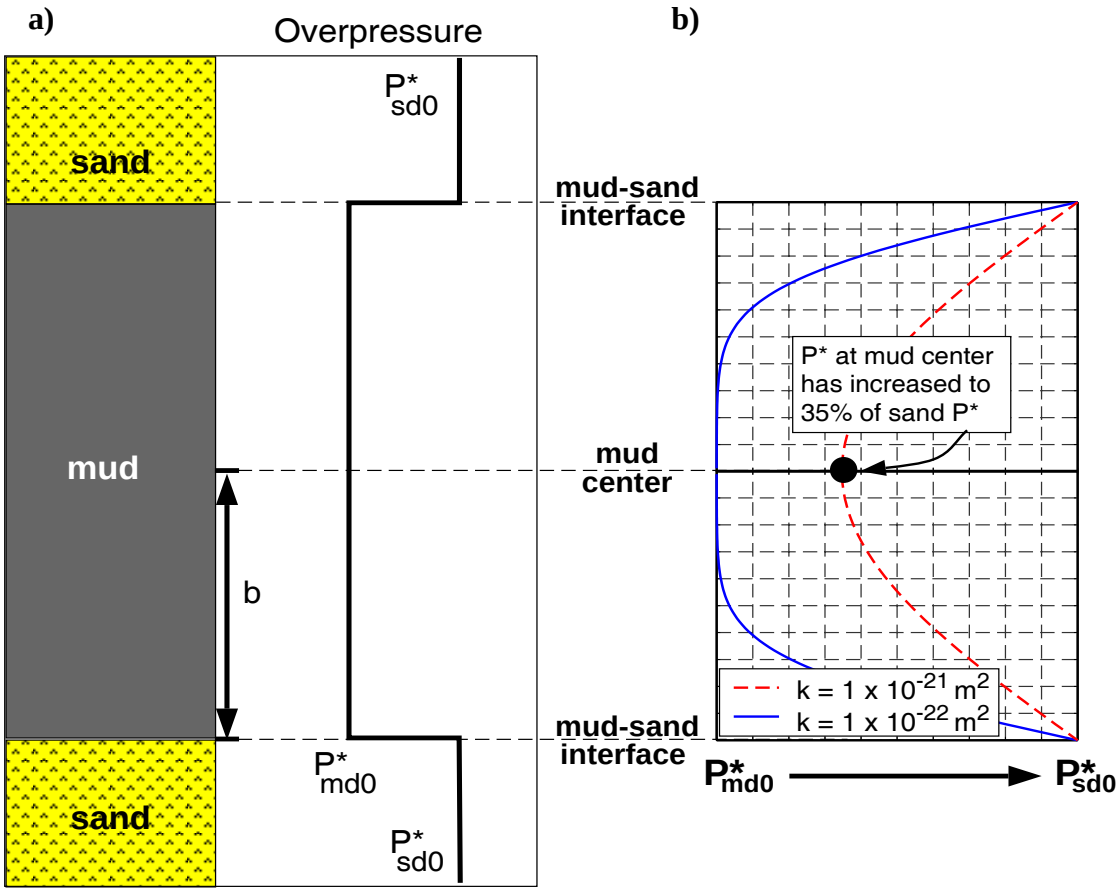

Figure 2.4: a) Fluid flow model (Appendix C) consists of a low-permeability mud between 2 permeable, more highly overpressured sands. Overpressure at the sand-mud interface is held constant (P^*_{sd0}), and overpressure in the mud increases due to fluid dissipation from the sand. b) Model indicates that after 1.5 m.y., the overpressure at the center of the mud layer is less than the overpressure in the sand.

Fluid Pressure Analysis in Mud

In low-permeability mud, it is not possible to efficiently measure fluid pressure directly. For this reason, indirect methods are generally used. By far the most common methods rely on an empirical relationship between porosity and effective stress. Terzaghi and Peck (1948) proposed a relationship between porosity and vertical effective stress, and a variety of workers have quantified this relationship (Rubey and Hubbert, 1959; Palciauskas and Domenico, 1989). This approach can be applied directly (Boatman, 1967) and through wireline methods (Hottman and Johnson, 1965; Ham, 1966; Macgregor, 1965) or even with seismic data (Pennebaker, 1968; Weakley, 1989). Each method has strengths and weaknesses which depend on both the ability of the tool to measure porosity and the extent to which the proposed porosity-effective stress relationship is valid.

We combine the definition of effective stress (Equation 2.4) and an empirical porosity-effective stress relationship proposed by Rubey and Hubbert (1959) (Equation 2.5) to calculate fluid pressure from porosity in muds (Equation 2.6) as described by Hart et al. (1995).

$$\sigma_v = S_v - P_f \tag{2.4}$$

$$\phi = \phi_0 e^{-\beta\sigma_v} \tag{2.5}$$

$$P_f = S_v - \left(\frac{1}{\beta}\ln\left(\frac{\phi_0}{\phi}\right)\right) \tag{2.6}$$

Lithostatic (overburden) stress (S_V) is calculated by integrating the wireline bulk density log. As shown by Finkbeiner et al. (1996), this varies from an overburden gradient (S_v/TVD) of 0.90 to 0.93 psi/ft (20.3 to 21.0 MPa/km) in the E.I. 330 field. The coefficients β and ϕ_0 are determined in the hydrostatic zone where fluid pressure, and therefore effective stress,

are known (Figure 2.5).

Porosity is calculated from the wireline sonic (travel time, Δt) log through an empirical relationship (Equation 2.7), developed by Raymer et al. (1980) and enhanced by Raiga-Clemenceau et al. (1986) (Equation 2.7). Porosity values calculated from the wireline bulk density logs generated similar estimates of fluid pressure (Stump and Flemings, 1998).

$$\phi = 1 - \left(\frac{\Delta t_{ma}}{\Delta t}\right)^{1/f} \tag{2.7}$$

Issler (1992) determined that for non-calcareous, low total organic carbon shale the matrix travel time (Δt_{ma}) is 220 μs/m (67 μs/ft) and the acoustic formation factor (*f)* is 2.19. Travel time measurements taken during deformation experiments on mud core from E.I. 330 indicate similar values for acoustic formation factor (Chapter 3).

Fluid Pressure Analysis in Sands

We compare porosity-predicted fluid pressure in muds with direct pressure measurements in adjacent sands (Figure 2.6a, points a and b). Pressure data were gathered during Repeat Formation Tests (RFTs) and shut-in bottom hole pressure surveys. In all cases, we used only virgin (pre-production) pressures in our analysis. In hydrocarbon-bearing sands the pressure of the hydrocarbon phase (e.g. P_g, P_o) exceeds the water phase pressure (P_w), due to fluid density differences. We calculate P_w for comparison with our predicted fluid pressure in the mud. Our results show that even after removing the buoyant effect of the hydrocarbon column, pressure in geopressured sands sometimes exceeds that in the bounding muds (Figure 2.6b).

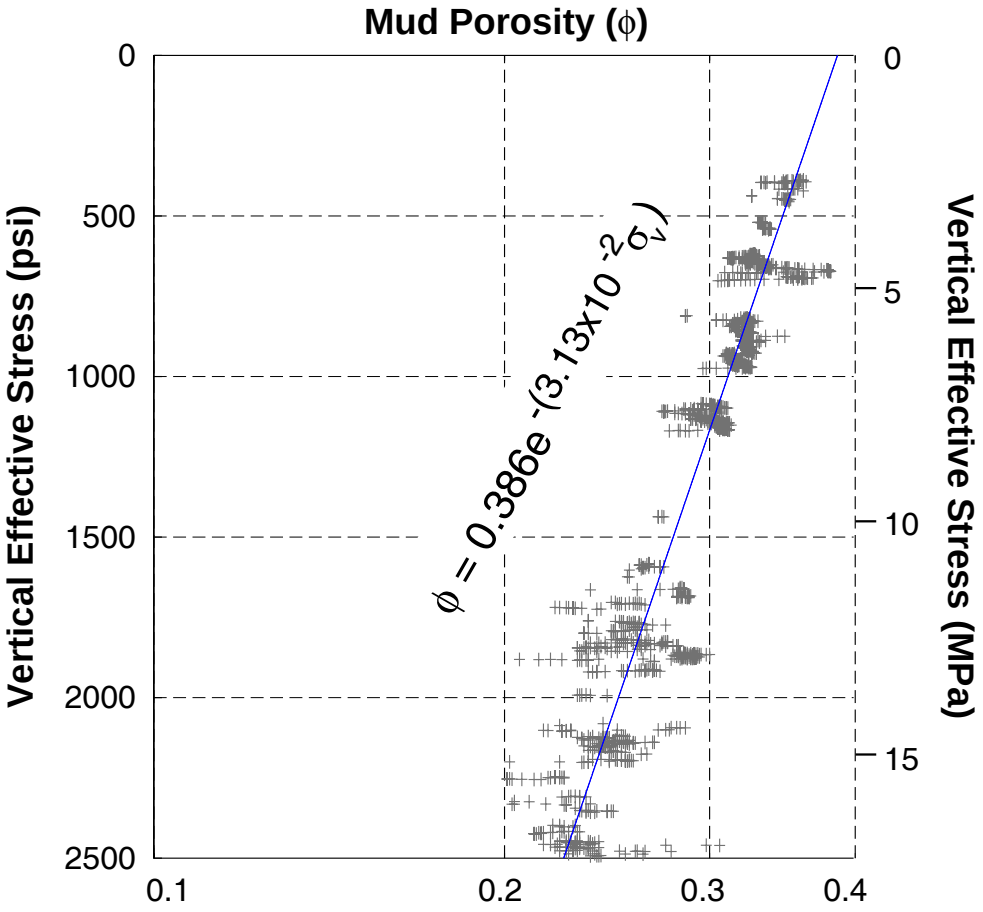

Figure 2.5: A log-linear plot of sonic-derived porosity (ϕ) versus vertical effective stress (σ_V) in the hydrostatic zone for the 331 #1 well (located in Figure 2.9) is used to establish a relationship to calculate fluid pressure in the overpressured zone. Lithostatic stress (S_v) is calculated by integrating the bulk density log; hydrostatic pressure is calculated from a gradient of 10.5 MPa/km (0.465 psi/ft) for sea water. Solid line represents the regression fit to the data.

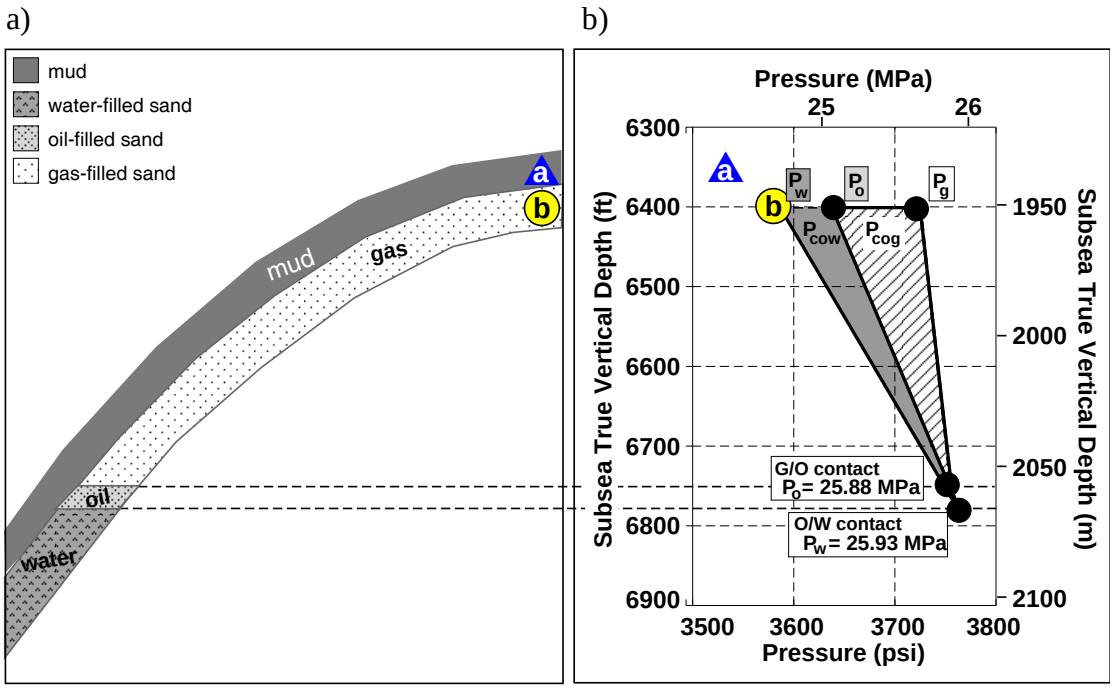

Figure 2.6: In this study we compare porosity-predicted fluid pressure in mud (triangle, point a) with water phase pressure (circle, point b) in the adjacent sand. Water phase pressures are used in order to negate the buoyant effect of the hydrocarbon column.

FLUID PRESSURES IN SANDS AND MUDS OF THE E.I. 330 FIELD

Field Characterization

The Eugene Island 330 (E.I. 330) field is located within a salt-withdrawal mini-basin (Figure 2.7). Plio-Pleistocene strata record a progradational history (Alexander and Flemings, 1995). Mud-prone prodelta deposits are overlain by sand-prone proximal deltaic strata. Salt-withdrawal during the prodelta and proximal deltaic phases created accommodation space (Rowan et al., 1998). A large regional growth fault developed to the north and northwest of this basin. Stratigraphic offset increases with depth as a result. In addition, differential salt-withdrawal from beneath the basin generated structural relief on the deeper sands (Figure 2.7).

The deepest reservoir, the Lentic 1 sand (Holland et al., 1990), was deposited during the prodelta phase (Alexander and Flemings, 1995). This sand lacks lateral continuity and is overlain by a thick mud section. The overlying OI through JD sands were deposited in the proximal deltaic environment (Figure 2.7). The majority of production in this field is from these laterally extensive sands (Holland et al., 1990).

Pressures record a transition from hydrostatic within fluvial strata to nearly lithostatic within the prodelta strata (Figures 2.8a,b). We characterize this pressure with the parameter, λ, which is the ratio of fluid pressure to overburden (P_f/S_v). The Lentic 1 sand is severely overpressured ($\lambda = 0.9$; pressure gradient = 0.83 psi/ft). The overlying OI-1 sand is moderately overpressured ($\lambda = 0.7$; pressure gradient = 0.63 psi/ft). The JD sand is slightly overpressured ($\lambda = 0.6$; pressure gradient = 0.55 psi/ft). Hart et al. (1995) and Gordon and Flemings (1998) characterize this pressure field in detail. In general, a key factor controlling the degree of overpressure is thought to be the ability of the deeper strata to expel fluids. The Lentic 1 sand is both laterally discontinuous and overlain by a thick mud section and, as a result, is

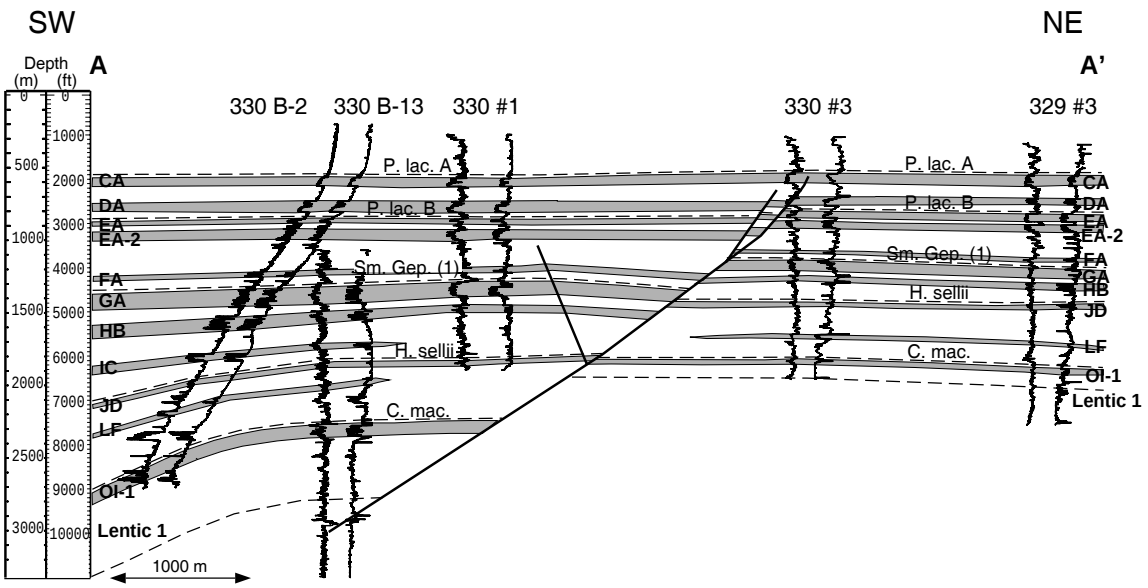

Figure 2.7: Wireline cross-section (reprinted from Gordon and Flemings, 1998) shows interbedded sands (gray areas) and mud of the E.I. 330 area. A regional growth fault dips to the southwest. The deeper sands (e.g. OI) have greater vertical relief than shallower sands.

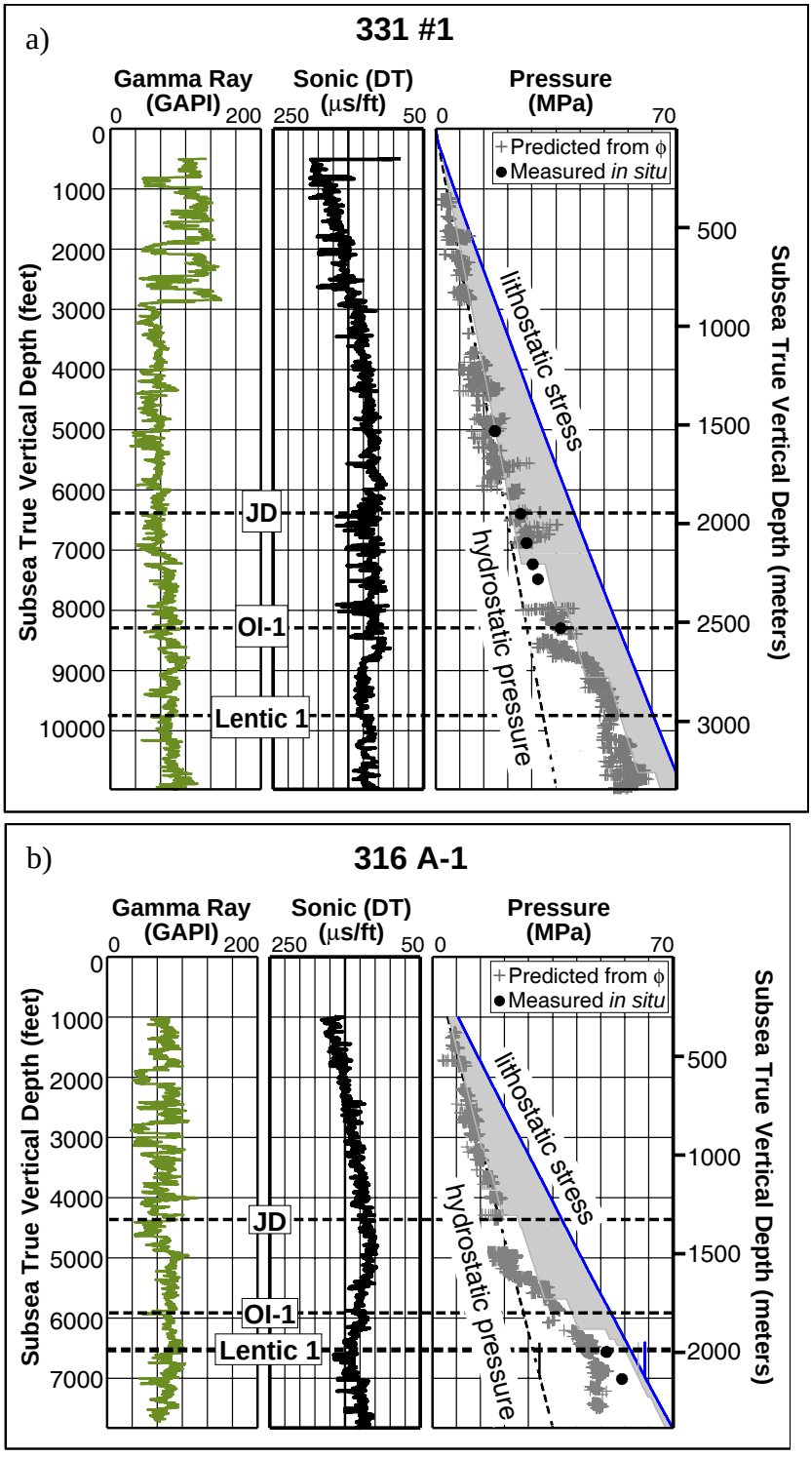

Figure 2.8a,b: Well logs and pressure profiles for the 331 #1 and 316 A-1 wells (located in Figure 2.9) locate the JD, OI-1, and Lentic 1 sands. The #1 well is on the downthrown side of the regional growth fault (Figure 2.7), while the A-1 is upthrown. On the pressure track, overpressure calculated from drilling mud weights is shown by white fill; vertical effective stress is light gray area.

severely overpressured. As explored in Gordon and Flemings (1998), overpressures are encountered at a much shallower level on the upthrown side of the fault (Figure 2.8b) than on the downthrown side (Figure 2.8a).

Characterization of the Lentic 1, OI-1, and JD Sands

Mud pressures were evaluated for fifteen wells in the E.I. 330 area (Figure 2.9). We examine fluid pressure in sands and bounding muds at three stratigraphic levels: Lentic 1, OI-1, and JD.

Lentic 1 Sand

The Lentic 1 is produced on the upthrown side of a regional growth fault in Blocks 330 and 316 (Figure 9). Finkbeiner (1998) and Finkbeiner et al. (in review) present a structure map of this horizon. Three wells which penetrate the Lentic 1 at different structural positions are used to predict the fluid pressure in the mud directly above the sand (Figure 2.10a). Near the sand-mud interface, fluid pressures in the mud are all less than the water phase pressure in the sand (Figure 2.10a). When these pressures are plotted on a depth-pressure plot, the vertical pressure gradient appears to be approximately lithostatic. At the structural high, the pressure in the sand is 4.2 MPa (612 psi) greater than that in the overlying mud. Fluid pressures converge at the structural low (2316 m; 7600 ft).

An overpressure cross-section through two of these wells provides a better sense of the spatial variability of fluid pressure (Figure 2.10b). Overpressure is constant and equal to 16.3 MPa (2363 psi) throughout the sand. The overpressure in the mud is less than the overpressure in the sand both above and below the sand (Figure 2.10b). In fact, the overpressure in the mud above and below the sand is nearly identical (Figure 2.10b, points A and B). The overpressure

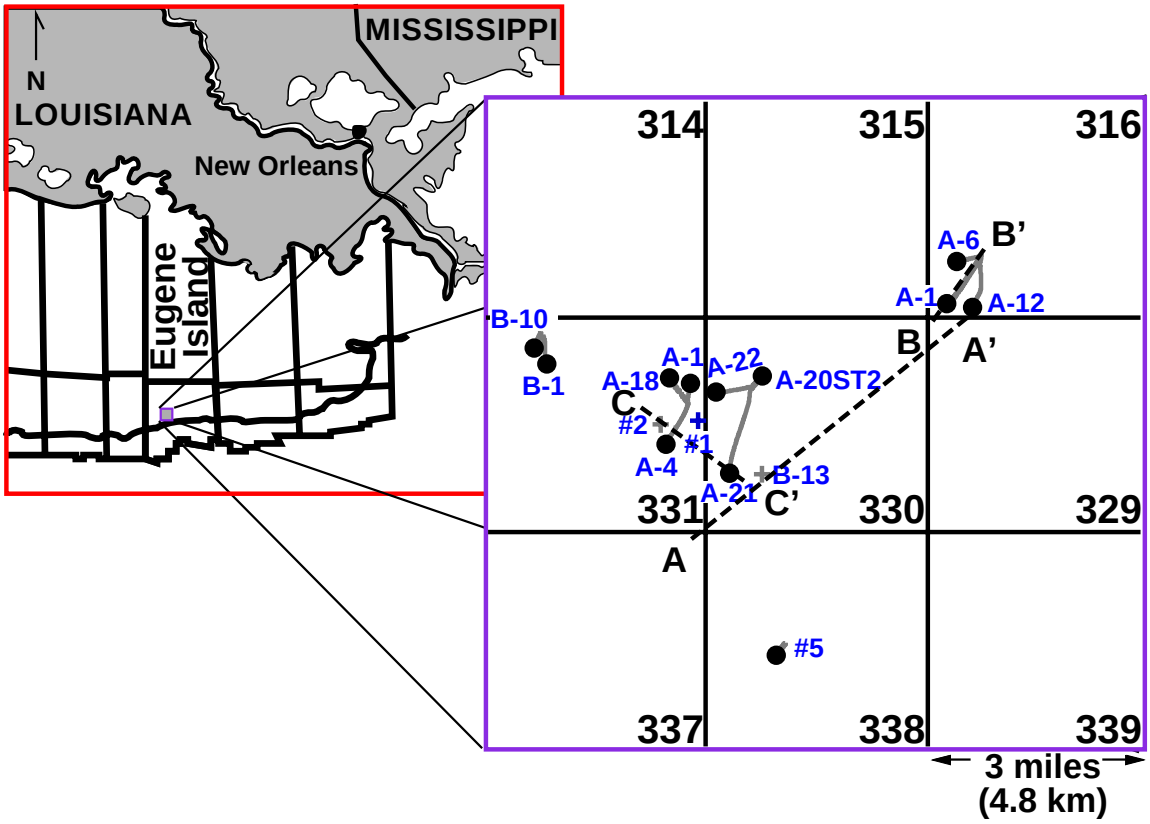

Figure 2.9: The E.I. 330 field is in the Gulf of Mexico, 272 km (169 mi) southwest of New Orleans, LA, U.S.A. at a water depth of ~77 m (253 ft) (Holland et al., 1990). We use wireline and pressure data from 15 wells in this field. Plus symbols indicate straight holes; solid lines represent deviated well paths; filled circles show the bottom hole locations of deviated wells. Dashed lines locate overpressure cross-sections (Figures 2.10b, 2.12a).

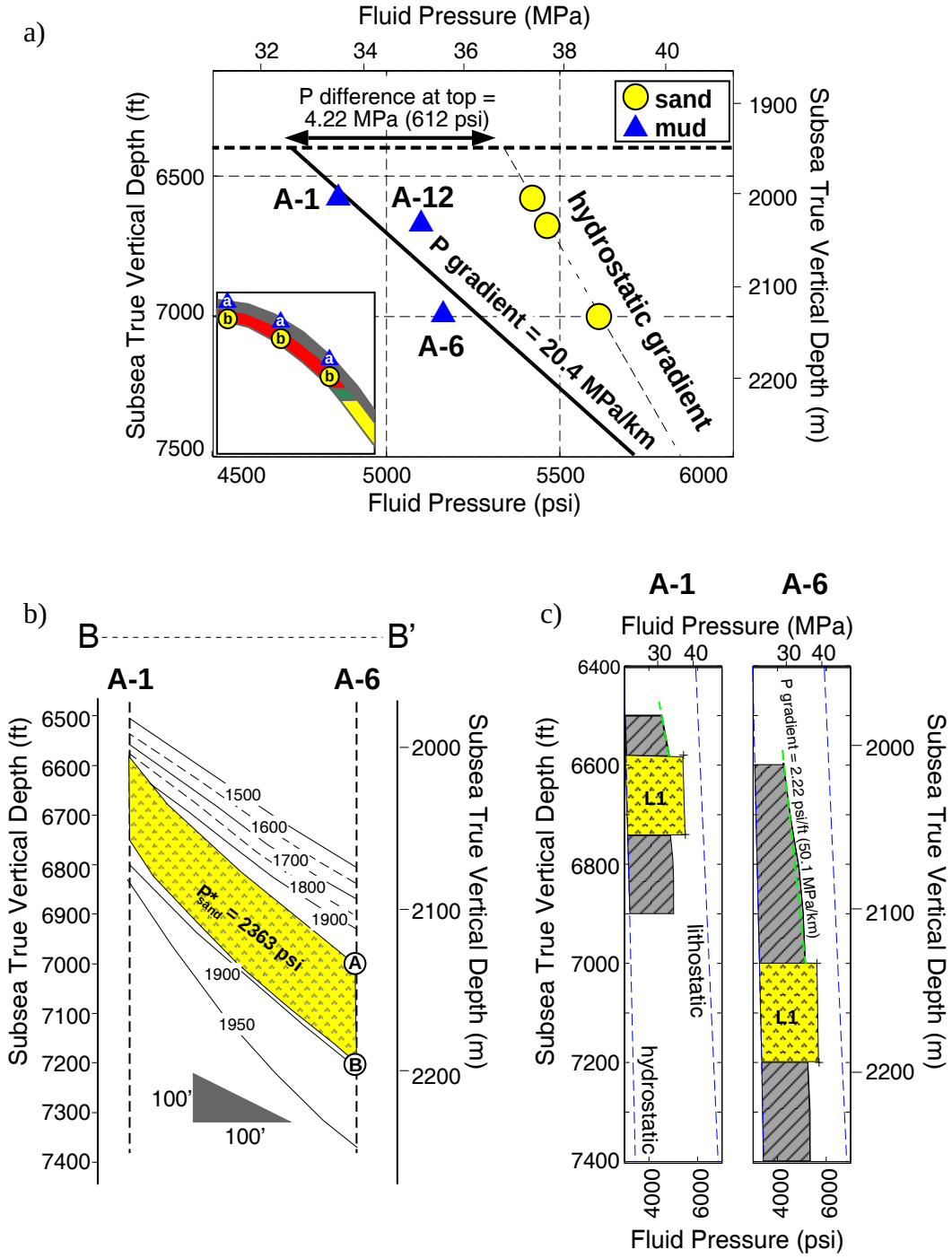

Figure 2.10: a) The Lentic 1 sand dips from 1950 m (6400 ft) to 2316 m (7600 ft) in Block 316. Fluid pressures in the sand (circles) are greater than pressures in the mud (triangles) at most depths; pressures converge near the structural low. The pressure gradient in the mud is approximately lithostatic. b) Overpressure cross-section B-B' (located in Figure 2.9) shows overpressure contours dipping parallel to structure. c) Well profiles through the Lentic 1 sand demonstrate that fluid pressure in the sand exceeds the fluid pressure in the overlying and underlying mud. The fluid pressure gradient in the mud, measured in a vertical profile, is significantly greater than the lithostatic gradient (50.1 MPa/km vs. 21.3 MPa/km).

contours in the mud are sub-parallel to the sand and converge slightly near the structural high.

Pressure profiles of the two wells (Figure 2.10c) reveal that the true vertical pressure gradient (50.1 MPa/km, 2.22 psi/ft) in the mud overlying the Lentic 1 sand is significantly greater than the lithostatic gradient. The apparent pressure gradient of 20.4 MPa/km (0.90 psi/ft) at the sand-mud interface (Figure 2.10a) is due to the laterally variability of overpressure in the mud.

In the mud overlying the Lentic 1 sand, overpressure contours are sub-parallel to the dip of the sand (Figure 2.10b). This observation correlates well with the overpressure profile predicted by the steady-flow model (Figure 2.3b). The steep pressure gradient in the mud overlying the sand appears to imply fluid flow from the highly overpressured sand into the mud, also predicted by the steady-flow model (i.e. at the structural high).

OI-1 Sand

Fluid pressures in the OI-1 sand exceed porosity-predicted pressures in the overlying mud above 2500 m (8200 ft) and are less than pressures in the mud below that depth (Figure 2.11). The pressure gradient in the mud calculated along structure is 26.0 MPa/km (1.15 psi/ft), slightly greater than the lithostatic gradient.

In the mud underlying the OI-1 sand, the overpressure gradient is largest near the sand-mud interface and then decreases with depth, as shown as a cluster of overpressure contours just beneath the sand (Figure 2.12a). In the B-10 well pressure profile (Figure 2.12b), the pressure gradient in the mud underlying the OI-1 is 55.8 MPa/km (2.47 psi/ft), significantly greater than the lithostatic gradient. In the #1 and A-21 wells, this behavior is observed in the few hundred feet of sediment directly below the OI-1 sand (e.g. to 2591 m (8500 ft) in the A-21, 2713 m (8900 ft) in the #1), and then the pressure gradient becomes approximately lithos-

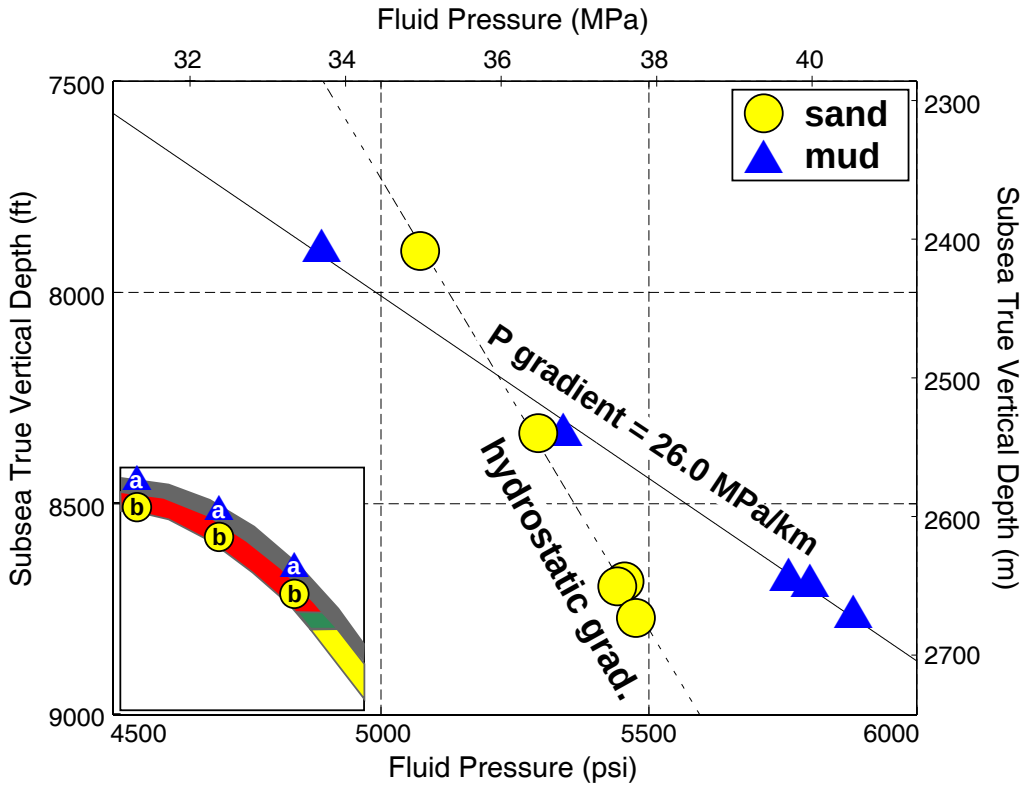

Figure 2.11: The OI-1 sand (structure map published in Finkbeiner, 1998) dips from 2073 m (6800 ft) to an estimated 2713 m (8900 ft). Porosity-predicted pressures in overlying mud (triangles) and fluid pressure measurements in the OI-1 sand (circles) are shown for the A-21, #1, B-1, A-4, and #2 wells. Fluid pressure in the OI-1 sand is equal to the fluid pressure in the overlying mud at 2500 m (8200 ft).

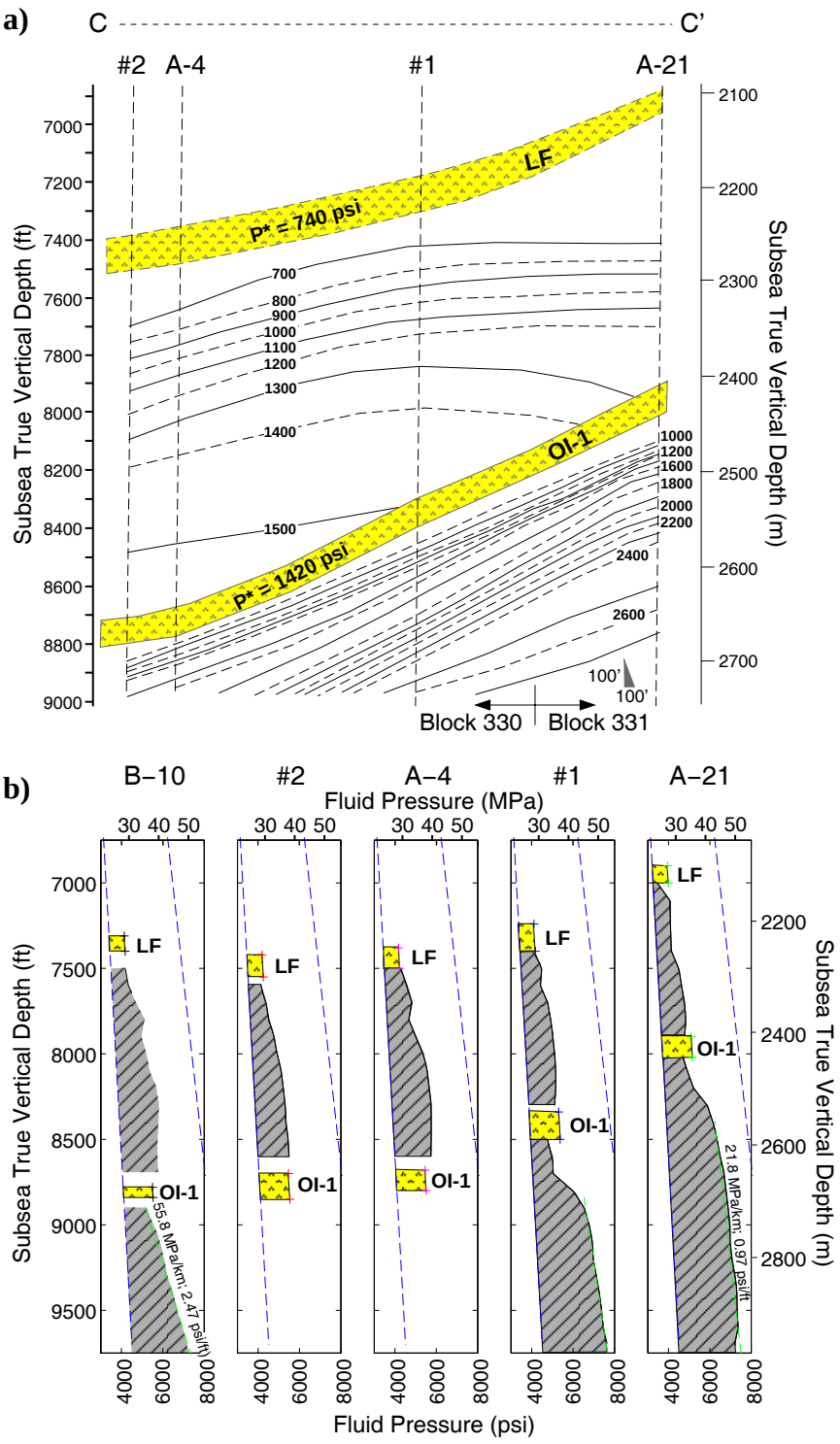

Figure 2.12: a) Overpressure cross-section through Blocks 330 and 331 (C-C', located on Figure 2.9) shows that beneath the OI-1 sand, overpressure contours dip sub-parallel to structure. In the mud above the OI-1 sand, overpressure contours are nearly horizontal. b) Well profiles of fluid pressure in the sands (dotted areas) and surrounding mud (striped areas) show the change in pressure gradient in the mud underlying the OI-1.

tatic (21.8 MPa/km, 0.97 psi/ft).

Between the LF and the OI-1 sands, pressure in the mud increases with depth and then decreases slightly in the sediment adjacent to the OI-1 sand (Figure 2.12b). The pressure in the mud overlying the OI-1 sand is greater for wells lower on structure (B-10, #2, A-4), approximately equal to the pressure in the sand at the #1 well, and less than the pressure in the sand at the A-21.

The fluid pressure in the mud just below the LF is approximately equal to the pressure in LF sand for wells which are lower on structure (Figure 2.12b). At the #1 well, pressure in the underlying mud is slightly less (0.97 MPa, 140 psi) than the pressure in LF sand. In the highest well on structure, the A-21, the pressure difference between the LF sand and underlying mud is greatest (3.7 MPa, 540 psi).

The muds beneath the OI-1 sand appear to record a complex history of fluid flow. The dipping overpressure contours in the mud underlying the OI-1 sand resemble the overpressure regime predicted by the steady-flow model. The steep pressure gradients in this mud layer appear to indicate fluid flow from the mud into the sand. However, current *in situ* fluid pressure measurements indicate that the sand is more highly overpressured (P^*_{sand} = 1420 MPa, 9.8 MPa) than the underlying mud (P^*_{mud} = 1000 psi; 6.9 MPa).

In the mud well below the OI-1 sand, fluid pressure gradient is lithostatic. The pressure behavior in this thick low-permeability mud is best described by the rapid-loading model.

JD Sand

Pressure measurements in the JD sand are less than pressures predicted in the overlying mud at most positions on structure (Figure 2.13). The pressure gradient in the mud (34.6 MPa/km, 1.53 psi/ft) exceeds the lithostatic gradient (Figure 2.13). Pressure predictions in the

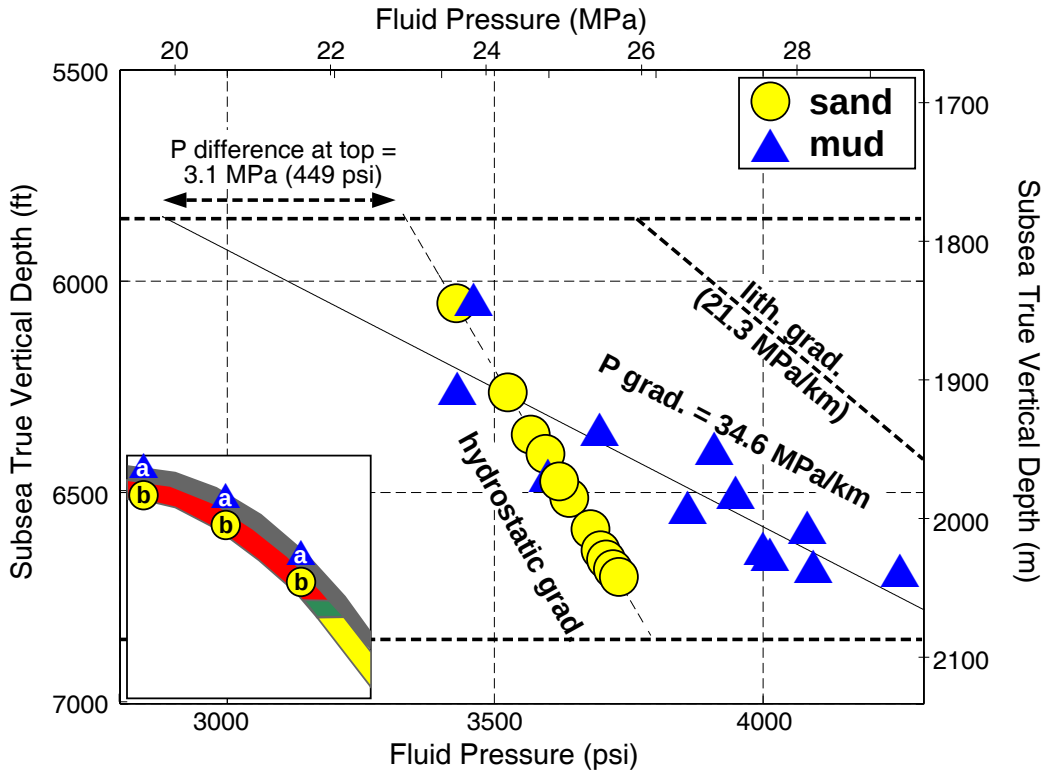

Figure 2.13: The shallowest sand we characterize, the JD, dips from 1780 m (5850 ft) to 2070 m (6800 ft), for a total relief of 290 m. Fluid pressure in the JD sand is less than pressure in the overlying mud at most points on structure. Pressure gradient within JD sand is hydrostatic; pressure gradient in the overlying mud is approximately lithostatic.

bounding mud exceed pressure measurements in the JD sand at most depths on structure. Based on the calculated gradients, at the structural high, fluid pressure in the sand exceeds pressure in the mud by approximately 3.1 MPa (449 psi). At the structural low, pressure in the mud is 3.9 MPa (562 psi) greater than pressure in the sand. Fluid pressures are equal at 1905 m (6250 ft).

DISCUSSION

Evolution of Pressure and Stress During Burial of Reservoir Sands

When viewed together, the pressure regimes in the Lentic 1, OI-1, and JD sands reveal similarities and differences. In all cases, the fluid pressures in the sands follow the hydrostatic gradient and the fluid pressures in the mud follow some gradient greater than hydrostatic. As a result, fluid pressures in the sand and the adjacent mud differ. A difference among the three sands is the location of the centroid depth. The centroid depth becomes shallower as one moves upward stratigraphically. Also, in the shallower sands (e.g. OI-1 and JD), there is much more evidence of pressure diffusion adjacent to the sand than there is at the deeper, Lentic 1 horizon. Not all of these observations can be easily explained with the rapid-loading or steady-flow models presented. However, the concepts can be used to build a model to describe how these sands may have evolved to their present state.

Modified Sediment Loading Model

Our modified sediment loading model considers variability in the depth at which the system becomes effectively sealed and accounts for pressure evolution following burial. Similar to the rapid-loading model, as a sand is initially buried by mud, both layers expel pore fluids and remain hydrostatically pressured (Figure 2.14a). Fluid expulsion is possible because

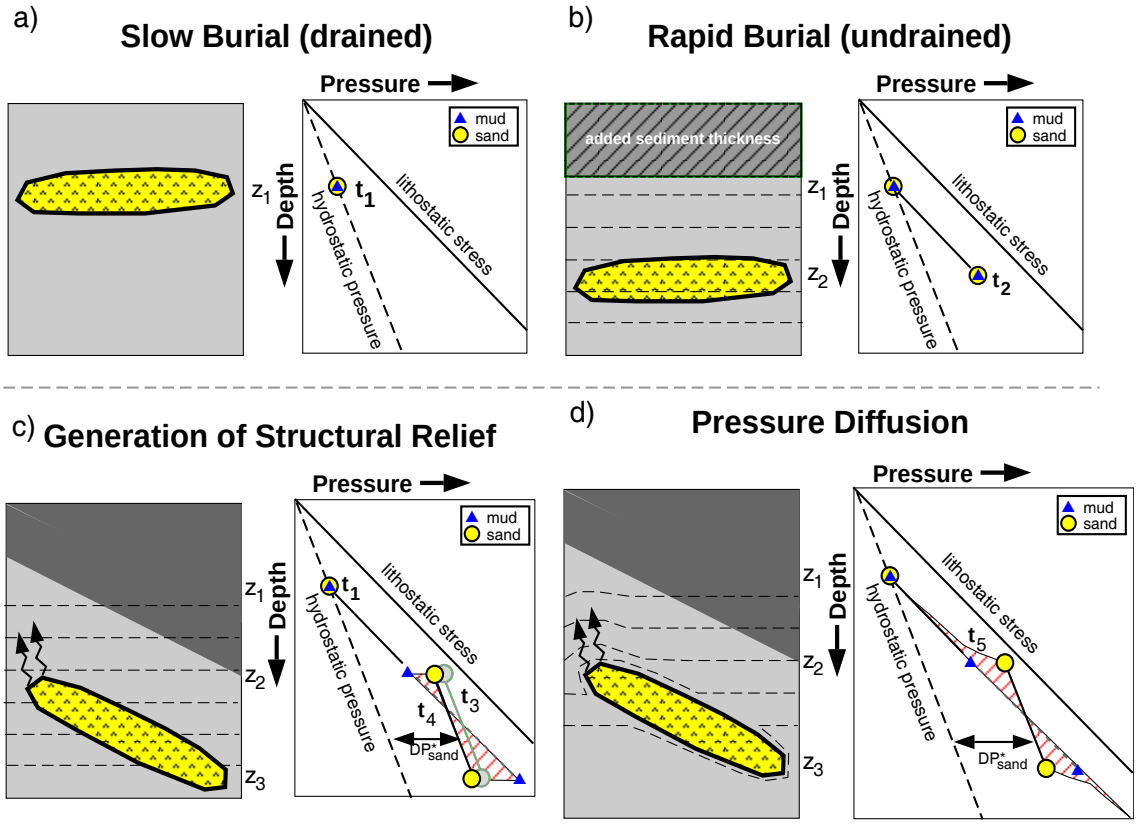

Figure 2.14: Pressure evolution in sand and bounding mud shows the effects of slow, then rapid burial, and eventual pressure diffusion at the structural high and low. a) At time 1, sand and mud are hydrostatically pressured at some depth, z_1. b) Sand layer is buried rapidly from z_1 to z_2; pressures in both sand and mud increase at lithostatic gradient. c) Differential subsidence causes sand to dip; fluid pressures in the sand and mud diverge at the structural high (t_3). Fluid migrates from the sand; pressure in the sand decreases and converges on pressure in the mud at the structural high (t_4). d) Over time, pressure diffusion occurs. Fluid pressure increases in the mud adjacent to the structural high; fluid pressure decreases in the mud adjacent to the structural low.

the sedimentation rate is low (Alexander and Flemings, 1995), and the newly deposited material has sufficiently high permeability. At a critical depth, the system becomes effectively sealed and ceases to expel fluids (Figure 2.14b). This transition may be caused by a sudden decrease in mud permeability as porosity drops beneath a critical level (Mello et al., 1994; Gordon and Flemings, 1998), or it may be due to an increase in sedimentation rate (Alexander and Flemings, 1995). The depth at which this transition occurs may vary (i.e. as sedimentation rate varies) during basin evolution.

Once the system becomes sealed, fluid pressures in both the sand and bounding mud increase at a nearly lithostatic gradient (Figure 2.14b) (Hart et al., 1995). Overpressure contours in the mud (Figure 2.14, dashed lines) are horizontal. Ultimately, subsidence occurs and creates a spatial variation in sedimentation. Fluid pressure within the permeable sand equilibrates to a hydrostatic gradient; the pressure gradient in the undrained mud is lithostatic. Therefore, as the sand begins to dip, the fluid pressure in the sand at the structural high begins to exceed pressure in the bounding mud (Figure 2.14c, t_3).

At that point, two things may occur. If the top of the sand is permeable and connected to other permeable layers, overpressured fluids flow out of the sand. If the pressure in the sand exceeds the minimum principal stress of the bounding mud, fluids hydrofracture the overlying mud and migrate via fracture permeability. Regardless of the mechanism, fluid migration causes a decrease in the sand overpressure (Figure 2.14c, t_4).

Eventually fluid flow and pressure diffusion occur (Figure 2.14d, t_5). At the structural high, where the pressure difference, and therefore fluid flow, is greatest, sand pressure diffuses into the mud (Figure 2.14d). At low points on structure, fluid flows into the sand,

thereby decreasing the fluid pressure in the mud. As a result of the pressure diffusion between the sand and mud, the overpressure contours around the sand lens are elevated near the top of structure and depressed at the structural low (Figure 2.14d).

We apply this modified sediment loading model to the Lentic 1, OI-1, and JD sands (Figure 2.15). At the Lentic 1, the centroid depth is low on structure (i.e. deeper than the depth midpoint of the structure), indicating that pressure dissipation (Figure 2.15a) has been negligible. However, Finkbeiner (1998) suggests that fluid pressure in the Lentic 1 sand is controlled by the minimum horizontal stress in the overlying mud. Any pressure greater than the current level would result in fluid flow via fracture in the overlying shale.

The muds adjacent to the OI-1 sand appear to record a complex history of fluid flow. The observed pressure regime suggests that fluid once migrated from the mud into the sand, and, at some later time, fluid pressure increased in the sand (Figure 2.15b, t_4). Fluid expulsion from the mud would have facilitated compaction, thereby decreasing permeability in the mud near the sand-mud interface. As fluid pressure in the sand increased, the low-permeability zone in the mud adjacent to the sand would hinder flow and prevent pressure from dissipating into the mud.

The JD sand appears to record a greater pressure bleed-off (Figure 2.15c), even though fluid pressures in the sand are well below the fracture gradient of the overlying mud (Finkbeiner 1998; Finkbeiner et al., in review). This observation implies that fluid migration occurred along permeable pathways (Alexander and Handschy, 1998), rather than by hydrofracture. The sediments which overlie the JD have a higher permeability than the sediments which directly overlie the Lentic 1, allowing potentially more vertical fluid flow and greater pressure dissipation.

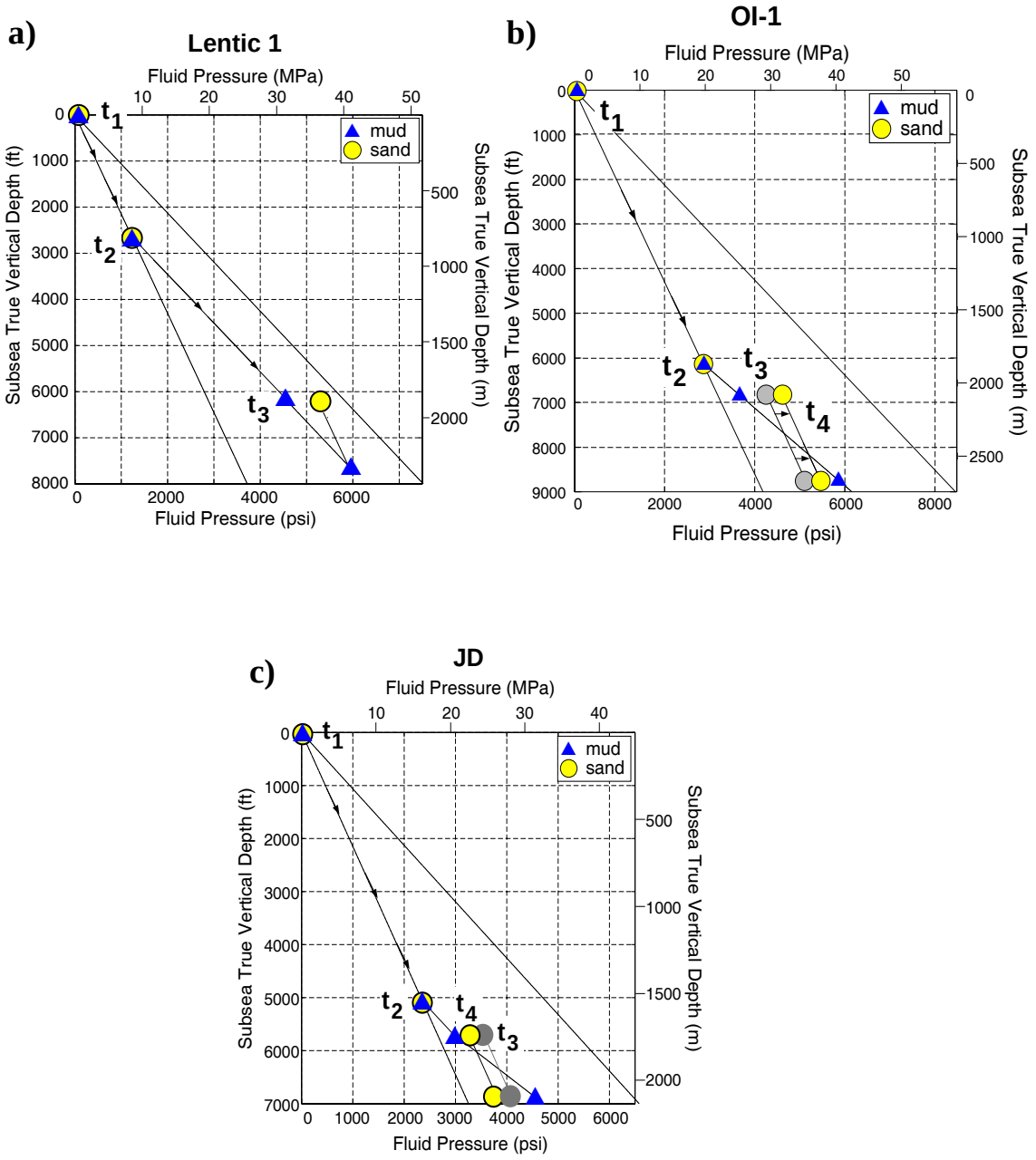

Figure 2.15: Model for pressure evolution in the Lentic 1, OI-1, and JD sands shows a hydrostatic increase in pressure from t_1 to t_2, and a nearly lithostatic increase in pressure from t_2 to t_3. Following t_3, as structure is generated, fluid pressure in the sand begins to exceed pressure in the overlying mud. a) Fluid pressure in the Lentic 1 sand remains greater than pressure in overlying mud (no dissipation is observed). b) OI-1 sand appears to record drainage and then a fluid pressure increase (t_4). c) Fluid pressure in the JD sand appears to have decrease as fluid migrated from the sand (t_3 to t_4).

Assessment of Observed Pressure Differences

We have combined theory and observation to suggest that fluid pressures in dipping sands are not necessarily in equilibrium with their bounding muds and that pressures differ in a predictable manner. Our observations rely critically upon the assumption that porosity can be used as a proxy for the pressure field. However, there are times when the porosity-derived pressure in muds may not record the actual fluid pressure in the mud. Bowers (1994) proposed that late-stage decreases in effective stress which are not recorded in the porosity signature will cause porosity-predicted pressure to underestimate *in situ* fluid pressure. The decrease in effective stress may be due to fluid pressure increases from aquathermal expansion (Barker, 1972), clay dehydration (Powers, 1967; Burst, 1969), biogenic gas production, or matrix relaxation. As mud compaction is largely irreversible (i.e. plastic deformation), the decrease in effective stress does not cause the sediment to decompact along the initial compaction curve. Therefore, porosity underpredicts the current fluid pressure.

In geologic basins, increased fluid pressure in a dipping sand, due to rapid-loading or steady-flow mechanisms, could result in increased pressure in the mud adjacent to the structural high. As a result, a porosity-derived pressure prediction would underestimate fluid pressure in the mud at the structural high. Results from deformation experiments on mud samples from this area (Chapter 3) and a wireline analysis by Bowers (1998) indicate no history of late-stage fluid pressure increase in these muds.

A second potential cause for the porosity-predicted pressure to differ from *in situ* pressure in the mud is the failing of the sonic (travel time) log to accurately estimate porosity. In this regard, we emphasize that we had produced similar results with the bulk density logs (Stump and Flemings, 1998).

Implications

Both the instantaneous loading and steady-state flow models predict that cross-stratal (i.e. near-vertical) flow is dominant at structural highs, where the pressure difference between the sand and the mud is a maximum and where the elevated fluid pressure in the sand has the greatest potential to converge on the minimum principal stress in the bounding mud (Figure 2.16). Differential sediment loading or steady-state flow into a permeable sand lens, independent of the presence of a hydrocarbon phase, can, therefore, drive a system to hydrofracture. Cross-stratal flow (e.g. flow via fracture permeability) is most likely to occur soon after basin deposition.

CONCLUSIONS

Differential sediment loading of a permeable sand by an impermeable mud can generate fluid pressure which differs from that in the overlying mud. Additionally, the permeability contrast between a dipping sand lens and surrounding mud causes fluid to preferentially flow into the sand. In either case, the fluid pressure at the top of the dipping sand will exceed the pressure in the adjacent mud, and the pressure difference between the sand and mud will change with position on structure. These pressure differences are documented for fifteen wells in the E.I. 330 area using porosity-derived predictions in muds and *in situ* measurements in sands. Two quantitative models describe the origin of the observed differences and provide methods for calculating fluid pressure in the sand as a function of total relief. The rapid-loading model predicts the pressure regime in the sand as a function of the geometry of the overlying load. The steady-flow model calculates the pressure difference from the flow velocity, which is directly determined from the far-field overpressure gradient in the mud. These mod-

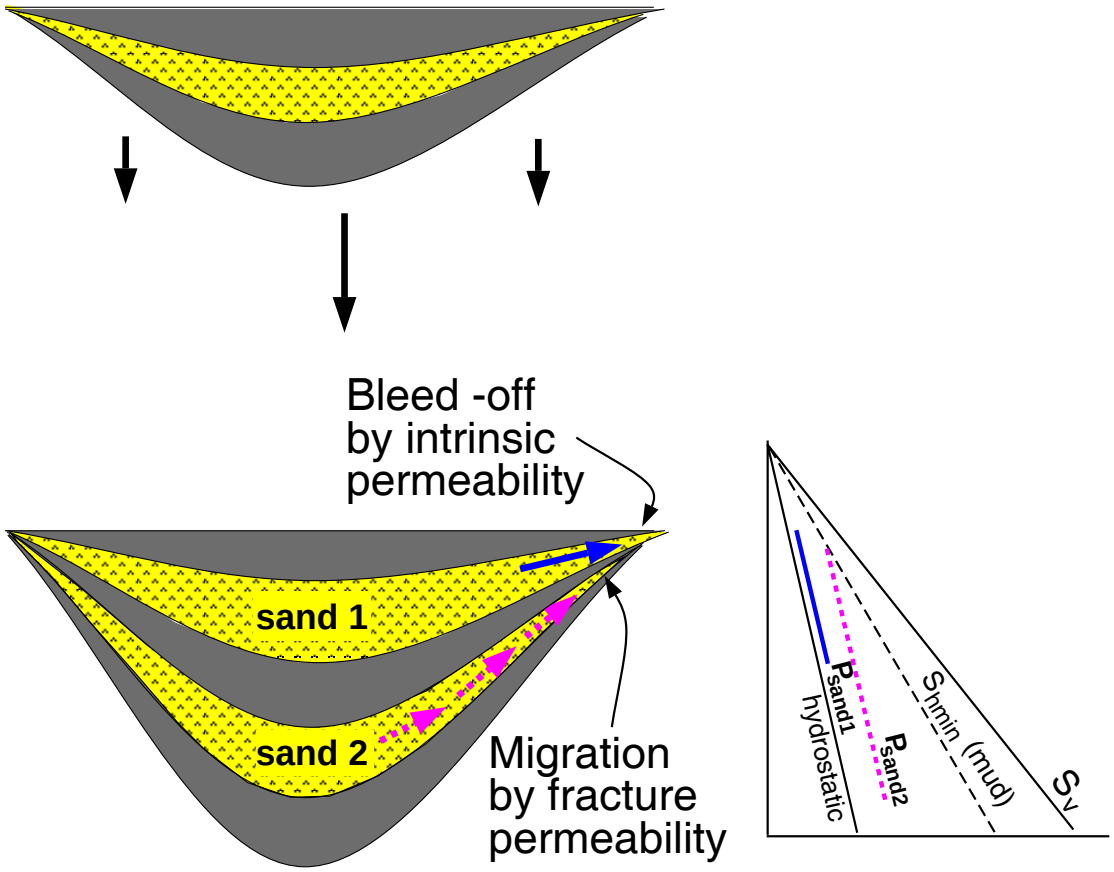

Figure 2.16: Basin-scale fluid migration occurs as a result of two different mechanisms. A shallow sand expels fluids along permeable pathways to the surface, thereby reducing the overpressure in the sand. A deeper sand, with greater structural relief, has a higher overpressure at the structural high than the adjacent sediments. As pressure in the deeper sand converges on the minimum principal stress (S_{hmin}) in the bounding mud, fluid bleeds off along newly-opened fractures.

els provide insight into the evolution of pressure, stress, and fluid flow in the basin. In addition, this approach has the potential to provide insight into trap quality and the history of secondary migration.

ACKNOWLEDGMENTS

This research is supported by the Gas Research Institute (Contract # 5095-260-3558). I would like to thank Pennzoil, Shell, and Texaco for generously providing the data used in this analysis, as well as Martin Traugott and Phil Heppard (Amoco) for their insight into the effect of structural relief on fluid pressure. Discussions with Mike Maler (Shell), Glenn Bowers (AMT), Alan Huffman (Conoco), and Steve Tennant (Shell) helped focus this work. Critical reviews by Derek Elsworth (Penn State), Terry Engelder (Penn State), and Dick Parker (GRI) strengthened this manuscript. Mincom's Geolog^{TM} software was used in this study.

REFERENCES

Alexander, L.L. and P.B. Flemings, 1995, Geologic evolution of a Plio-Pleistocene salt-withdrawal minibasin: Eugene Island block 330, offshore Louisiana: American Association of Petroleum Geologists Bulletin, v. 79, p. 1737-1756.

Alexander, L.L. and J.W. Handschy, 1998, Fluid flow in a faulted reservoir system: fault trap analysis for the block 330 field in Eugene Island South Addition, offshore Louisiana: American Association of Petroleum Geologists Bulletin, v. 82, p. 387-411.

Athy, L.F., 1930, Density, porosity, and compaction of sedimentary rocks: American Association of Petroleum Geologists Bulletin, v. 14, p. 1-22.

Barker, C., 1972, Aquathermal pressuring - role of temperature in development of abnormal-pressure zones: American Association of Petroleum Geologists Bulletin, v. 56, p. 2068-2071.

Bird, R.B., W.E. Stewart, and E.N. Lightfoot, 1960, Transport Phenomena: New York, John Wiley and Sons, Inc., 780 pp.

Boatman, W.A., 1967, Measuring and using shale density to aid in drilling wells in high-pressure areas: Journal of Petroleum Technology, p. 1423-1429.

Bowers, G.L., 1994, Pore pressure estimation from velocity data: Accounting for overpressure mechanisms besides undercompaction: Society of Petroleum Engineers, SPE 27488, p. 515-529.

Bowers, G.L., 1998, A procedure for determining an appropriate pore pressure estimation strategy: American Association of Drilling Engineers industry forum on pressure regimes in sedimentary basins and their prediction, September 2-4, Lake Conroe, TX.

Burst, J.F., 1969, Diagenesis of Gulf Coast clayey sediments and its possible relation to petroleum migration: American Association of Petroleum Geologists Bulletin, v. 53, p. 73-93.

de Marsily, G., 1986, Quantitative Hydrogeology: Groundwater Hydrology for Engineers: San Diego Academic Press, Inc., 592 pp.

Dickinson, G., 1953, Geological aspects of abnormal reservoir pressures in Gulf Coast Louisiana: American Association of Petroleum Geologists Bulletin, v. 37, p. 410-432.

Eaton, B.A., 1975, The equation for geopressure prediction from well logs: Society of Petroleum Engineers, SPE 5544.

England, W.A., A.S. MacKenzie, D.M. Mann, and T.M. Quigley, 1987, The movement and entrapment of petroleum fluids in the subsurface: Journal of the Geological Society, London, v. 144, p. 327-347.

Finkbeiner, T., B.B. Stump, M.D. Zoback, P.B. Flemings, 1996, Pressure (P_p), overburden (S_v), and minimum horizontal stress (S_{hmin}) in Eugene Island Block 330, offshore Gulf of Mexico: Gas Research Institute, GRI-96/0285.

Finkbeiner, T., 1998, In situ stress, pore pressure, and hydrocarbon migration and accumulation in sedimentary basins, Ph.D. dissertation, Stanford University.

Finkbeiner, T., M. Zoback, B. Stump, P. Flemings, in review, Stress, pore pressure, and dynamically constrained hydrocarbon columns in the South Eugene Island 330 field, Gulf of Mexico.

Gordon, D.S. and P.B. Flemings, 1998, Generation of Overpressure and Compaction-Driven Fluid Flow in a Plio-Pleistocene Growth-Faulted Basin, Eugene Island 330, Offshore Louisiana: Basin Research, v. 10, p. 177-196.

Ham, H.H., 1966, A method of estimating formation pressures from Gulf Coast well logs: Transactions Gulf Coast Association of the Geological Society, v. 16, p. 185-197.

Hart, B.S., P.B. Flemings, and A. Deshpande, 1995, Porosity and pressure: Role of compaction disequilibrium in the development of geopressures in a Gulf Coast Pleistocene basin: Geology, v. 23, p. 45-48.

Holland, D.S., W.E. Nunan, and D.R. Lammlein, 1990, Eugene Island Block 330 field- U.S.A., offshore Louisiana, *in* E.A. Beaumont and N.H. Foster, eds. Structural traps III, tectonic fold and fault traps: American Association of Petroleum Geologists Treatise of Petroleum Geology, Atlas of Oil and Gas Fields, p. 103-143.

Hottman, C.E. and R.K. Johnson, 1965, Estimation of formation pressure from log-derived shale properties: Journal of Petroleum Technology, v. 17, p. 717-722.

Iliffe, J.E., C. Wynn, N. Cameron, and A.G. Robertson, 1998, Whoopee cushions and hydrofracture induced vertical migration: implications for shallow prospectivity with reference to UKCS, American Association of Drilling Engineers industry forum on pressure regimes in sedimentary basins and their prediction, September 2-4, Lake Conroe, TX.

Issler, D.R., 1992, A new approach to shale compaction and stratigraphic restoration, Beaufort-Mackenzie basin and Mackenzie Corridor, northern Canada: American Association of Petroleum Geologists Bulletin, v. 76, p. 1170-1189.

Macgregor, J.R., 1965, Quantitative determination of reservoir pressures from conductivity log: AAPG Bulletin, v. 49, p. 1502-1511.

Mann, D.M., and A.S. Mackenzie, 1990, Prediction of pore fluid pressures in sedimentary basins: Marine and Petroleum Geology, v. 7, p. 55-65.

Mello, U.T., G.D. Karner, and R.N. Anderson, 1994, A physical explanation for the positioning of the depth to the top of overpressure in shale-dominated sequences in the Gulf Coast basin, United States: Journal of Geophysical Research, v. 99, p. 2775-2789.

Neuzil, C.E., 1994, How permeable are clays and shales?: Water Resources Research, v. 30, p. 145-150.

Palciauskas, V.V. and P.A. Domenico, 1989, Fluid pressures in deforming porous rocks: Water Resources Research, v. 25, p. 203-213.

Pennebaker, E.S., 1968, Seismic data indicate depth, magnitude of abnormal pressure: World Oil, v. 166, p. 73-78.

Phillips, O.M., 1991, Flow and reactions in permeable rocks: New York, Cambridge University Press, 285 p.

Powers, M.C., 1967, Fluid release mechanisms in compacting marine mudrocks and their importance in oil exploration: American Association of Petroleum Geologists Bulletin, v. 51, p. 1240-1254.

Raiga-Clemenceau, J., J.P. Martin, and S. Nicoletis, 1986, The concept of acoustic formation factor for more accurate porosity determination from sonic transit time data: SPWLA 27th Annual Logging Symposium Transactions, Paper G.

Raymer, L.L., E.R. Hunt, and J.S. Gardner, 1980, An improved sonic transit time-to-porosity

transform: SPWLA 21th Annual Logging Symposium Transactions, Paper P.

Rowan, M.G., B.S. Hart, S. Nelson, P.B. Flemings, B.D. Trudgill, 1998, Three-dimensional geometry and evolution of a salt-related growth-fault array: Eugene Island 330 field, offshore Louisiana, Gulf of Mexico: Marine and Petroleum Geology, v. 15, p. 309-328.

Rubey, W.W. and M.K. Hubbert, 1959, Overthrust belt in geosynclinal area of western Wyoming in light of fluid pressure hypothesis, 2: Role of fluid pressure in mechanics of overthrust faulting: Geological Society of America Bulletin, v. 70, p. 167-205.

Scott, D., and Thomsen, L.A., 1993, A Global Algorithm for Pore Pressure Prediction: Society of Petroleum Engineers, SPE 25674.

Shosa, J. and L.M. Cathles, 1996, Capillary exit pressure as a basin sealing mechanism: American Association of Petroleum Geologists 1996 Annual Convention Abstracts, May 19-22, San Diego CA, p. 129-130.

Stump, B.B. and P.B. Flemings, 1998, Sediment loading and resulting pressure differences between overpressured sands and bounding shales of the Eugene Island 330 field (offshore Louisiana): Gas Research Institute, GRI-97/0266.

Terzaghi, K. and R.B. Peck, 1948, Soil mechanics in engineering practice: New York, John Wiley and Sons, Inc., 566 p.

Traugott, M.O. and P.D. Heppard, 1994, Prediction of pore pressure before and after drilling-- taking the risk out of drilling overpressured prospects: American Association of Petroleum Geologists Hedberg Research Conference, Denver.

Wallace, W.E., 1965, Abnormal surface pressure measurements from conductivity or resistivity logs: Oil & Gas Journal, v. 63, p. 102-106.

Weakley, R.R., 1989, Use of surface seismic data to predict formation pore pressures (sand shale depositional environments): Society of Petroleum Engineers, SPE 18713.

APPENDIX A: DERIVATION OF RAPID-LOADING MODEL

One dimension

Consider a material element that is loaded from above with a stress DS_v. The element contains a constant number of grains and remains undrained (i.e. no fluids escape) during loading. The applied load is balanced by an opposing stress which is the combination of change in fluid pressure (DP_f) and the change in vertical effective stress ($D\sigma_V$) in the material element.

$$\left[\frac{\beta}{(1-\phi)} - \beta_f\right] DS_v = \frac{\beta}{1-\phi} DP_f - (\beta_f - \beta_s) D\sigma_v \tag{2.8}$$

Equation 2.8 is derived in Gordon and Flemings (1998) who built on the derivation of Palciauskas and Domenico (1989). Equation 2.8 assumes: 1) the solid grains are incompressible; 2) fluid and matrix are linearly compressible $\{(1/\rho_f)D\rho_f = \beta_f DP_f;\ D\phi = -\beta\phi D\sigma_V\}$; 3) strain is uniaxial; and 4) there are no temperature effects.

Consider the same material element buried a depth dz:

$$DS_v = \rho_b g dz \tag{2.9}$$

$$DP_f = \rho_f g dz + DP^* \tag{2.10}$$

$$D\sigma_v = \rho_b g dz - (\rho_f g dz + DP^*) \tag{2.11}$$

Substituting Equations 2.9, 2.10, 2.11 into Equation 2.8, and solving for the change in fluid pressure, we find:

$$DP_f = \left(\frac{\beta}{\beta_f(1-\phi) + \beta}\right) \rho_b g dz \tag{2.12}$$

In our work in Plio-Pleistocene strata of the E.I. 330 area, typical bulk compressibility

and porosity values are 3.13 x 10^{-2} MPa^{-1} and 0.3, respectively (Hart et al., 1995, Gordon and Flemings, 1998), while fluid compressibility is 4.88 x 10^{-4} MPa^{-1} (de Marsily, 1986). Using these values, Equation 2.12 reduces to:

$$DP_f = 0.989\rho_b g dz \tag{2.13}$$

Thus, the change in fluid pressure (DP_f) supports ~99% of the change in the overburden load (DS_v). The one dimensional case is analogous to a mud layer which has no updip pressure communication. Therefore, we can write an expression for overpressure in the mud as:

$$DP^*_{mud} = \left(\left(\frac{\beta}{\beta + \beta_f(1-\phi)}\right)\rho_b - \rho_f\right) g dz \tag{2.14}$$

Two dimensions

Consider next the problem of a sand body of length L that has been buried to a variable depth z, where z = f(x) (Figure 2.17). The sand is composed of material elements of length dx. We assume that the fluid can be displaced within the sand (q), but that no fluid leaves the sand body. Under this constraint, balance of stress requires:

$$\left[\frac{\beta}{(1-\phi)} - \beta_f\right] DS_v(x) = \frac{\beta}{1-\phi} DP(x) - \beta_f D\sigma_v(x) + \frac{1}{\rho_f}\nabla\rho_f q(x) \tag{2.15}$$

In this case, the changes in overburden, fluid pressure, and effective stress are:

$$DS_v = \rho_b g dz(x) \tag{2.16}$$

$$DP_f = \rho_f g dz(x) + DP^* \tag{2.17}$$

$$D\sigma_v = \rho_b g dz(x) - (\rho_f g dz(x) + DP^*) \tag{2.18}$$

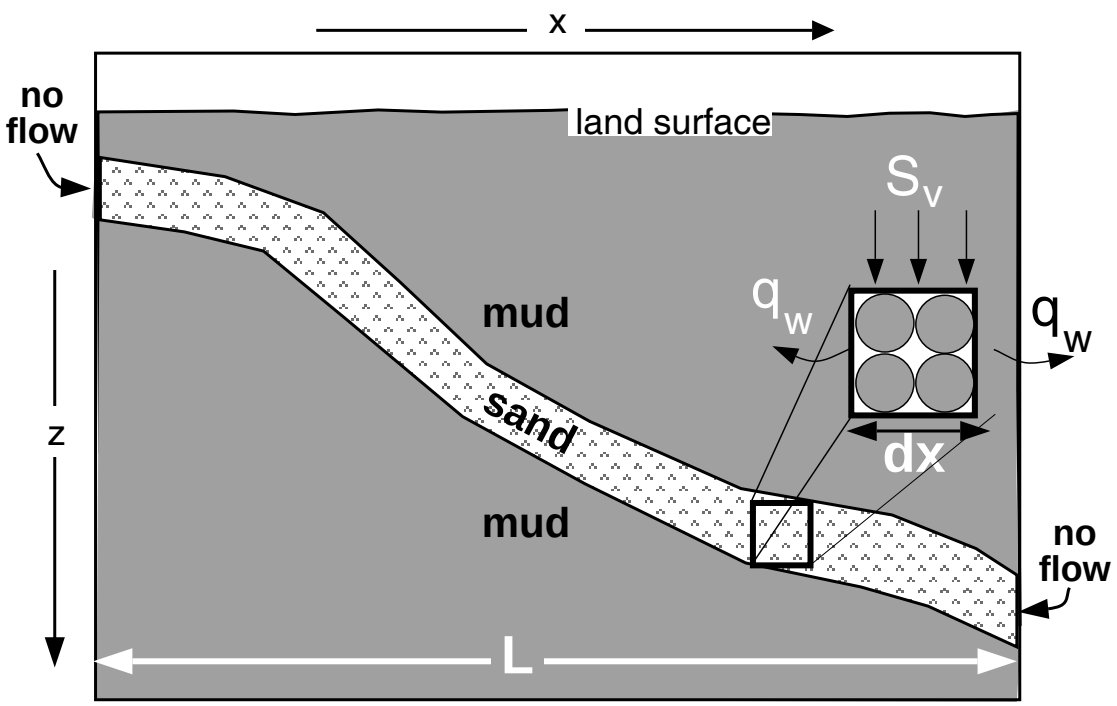

Figure 2.17: The overpressure within a dipping sand of length L is a function of the integrated overlying load (Equation 2.20). No flow boundaries at both ends of the sand layer maintain an undrained state.

Substituting Equations 2.16-2.18 into Equation 2.15 and integrating over the length of the sand body L, we find:

$$\left[\frac{\beta}{(1-\phi)}-\beta_f\right]\int_0^L DS_v(x) \;=\; \frac{\beta}{(1-\phi)}\int_0^L DP_f(x)-\beta_f\int_0^L D\sigma_v(x)-\int_0^L \frac{1}{\rho_f}\nabla\rho_f q(x) \tag{2.19}$$

overburden load fluid pressure effective stress flow term

Because we assume that the entire sand body is undrained, the integral of the flow term is equal to zero. Upon integration, and solving for the change in overpressure resulting from structural relief, we find:

$$DP_{sand}^{*} \;=\; \left(\left(\frac{\beta}{\beta+\beta_f(1-\phi)}\right)\rho_b-\rho_f\right)g\int_0^L z(x)dx \tag{2.20}$$

Equation 2.20 can be solved for any load geometry (z(x) = f(x)) to estimate the over-pressure (DP*) added to the system by sediment loading. For example, in the main body of this paper, we present the results for three possible functions of z(x): linear, hyperbolic, and parabolic (Figure 2.1).

Three dimensions

We consider the problem in three dimensions by calculating the volume of sediment (e.g. rather than the area of sediment) overlying a sand layer. For the case of a homoclinal sand (i.e. 2-D case of z(x) = Ax), this problem reduces to the volume of a cylinder minus the volume of a cone (Equation 2.21) (Figure 2.18).

$$DP_{\text{3-D sand}}^{*} \;=\; \left(\left(\frac{\beta}{\beta+\beta_f(1-\phi)}\right)\rho_b-\rho_f\right)g(V_{cyl}-V_{cone}) \tag{2.21}$$

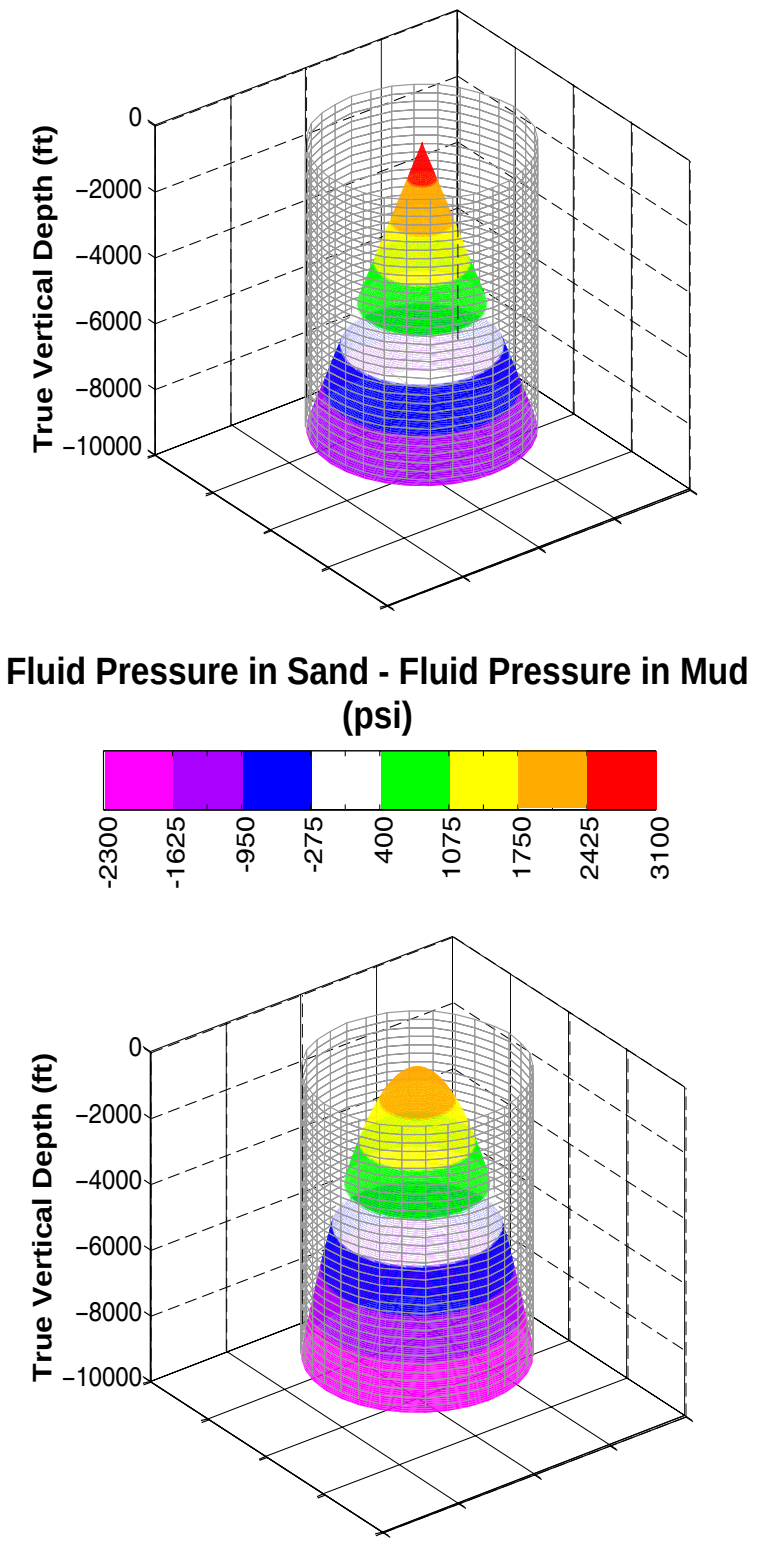

Figure 2.18: Three-dimensional geometry of the overlying load affects the fluid pressure. The pressure difference between sand and mud at the structural high of a steeply dipping sand is higher than for a more gently dipping structure.

As with the two-dimensional case, this problem can be solved for a sand with a more complex geometry by substituting different mathematical functions for V_{cone}. The effect of three-dimensional geometry on the magnitude of the sand-mud pressure differential is demonstrated in Figure 2.18.

APPENDIX B: STEADY-STATE FLOW MODEL

Phillips (1991) presented a mathematical solution for flow through a low permeability medium around a permeable lens. He proposed an elliptical coordinate system such that x and z are functions of ξ, η, and a.

$$x = a\cosh\xi\cos\eta \tag{2.22a}$$

$$z = a\sinh\xi\sin\eta \tag{2.22b}$$

Lines of constant ξ form ellipses, lines of constant η are hyperbolae, and a is the half-length of the sand lens. The stream function (Ψ) is calculated as a function of the transformed coordinates, a, and u, the undisturbed (far-field) velocity.

$$\Psi = ua\cosh\xi\sin\eta \tag{2.23}$$

Velocity is calculated perpendicular to streamlines, such that:

$$v_x = \frac{\partial\Psi}{\partial z} \tag{2.24a}$$

$$-v_z = \frac{\partial\Psi}{\partial x} \tag{2.24b}$$

The derivatives of the stream function are written as:

$$\frac{\partial\Psi}{\partial z} = ua\left[\cosh\xi\cos\eta\left(\frac{\partial\eta}{\partial z}\right) + \sinh\xi\sin\eta\left(\frac{\partial\xi}{\partial z}\right)\right] \tag{2.25a}$$

$$\frac{\partial\Psi}{\partial x} = ua\left[\cosh\xi\cos\eta\left(\frac{\partial\eta}{\partial x}\right) + \sinh\xi\sin\eta\left(\frac{\partial\xi}{\partial x}\right)\right] \tag{2.25b}$$

In order to take the partial derivatives in Equations 2.25a,b, it is first necessary to derive expressions for ξ and η in terms of x and z only. We accomplish this using identities for trigonometric and hyperbolic functions.

$$\frac{x^2}{a^2\cos^2\eta} - \frac{z^2}{a^2\sin^2\eta} = 1 \tag{2.26}$$

$$\cos^2\eta = 1 - \sin^2\eta \tag{2.27}$$

$$x^2a^2\sin^2\eta - z^2a^2(1-\sin^2\eta) = (a^2 - a^2\sin^2\eta)(a^2\sin^2\eta) \tag{2.28}$$

$$a^2\sin^4\eta + (x^2 + z^2 - a^2)\sin^2\eta - z^2 = 0 \tag{2.29}$$

Using the quadratic formula, we can solve for $\sin^2\eta$.

$$\sin^2\eta = \frac{-x^2 - z^2 + a^2 \pm \sqrt{(x^2+z^2-a^2)^2 - 4(a^2)(-z^2)}}{2a^2} = X_\eta \tag{2.30}$$

$$\eta = \sin^{-1}\sqrt{X_\eta} \tag{2.31}$$

This can be differentiated using the chain rule. Recall that any function y = f(x) can be differentiated as follows.

$$\frac{\partial y}{\partial x} = \frac{\partial y}{\partial n}\cdot\frac{\partial n}{\partial x} \tag{2.32}$$

In this case,

$$y = \sin^{-1} n \qquad n = \sqrt{X_\eta} \tag{2.33a}$$

$$\frac{\partial y}{\partial n} = \frac{1}{\sqrt{1-n^2}} \qquad \frac{\partial n}{\partial x} = \frac{1}{2}(X_\eta)^{-\frac{1}{2}}X_\eta' \tag{2.33b}$$

$$n^2 = X_\eta \tag{2.34}$$

$$X_\eta' = \frac{1}{2a^2}\left[-2x + \frac{1}{2}\left((x^4+z^4+a^4+2x^2z^2-2a^2x^2+2a^2z^2)^{-\frac{1}{2}}\cdot(3x^4+4xz^2-4xa^2)\right)\right] \tag{2.35}$$

For brevity of presentation, we can break out two of the larger terms.

$$\text{bsqreta} = x^4 + z^4 + a^4 + 2x^2z^2 - 2a^2x^2 + 2a^2z^2 \tag{2.36}$$

$$\text{quadeta} = (-x^2 - z^2 + a^2 + \sqrt{\text{bsqreta}})/(2a^2) \tag{2.37}$$

$$\frac{\partial \eta}{\partial x} = \frac{1}{\sqrt{1-\text{quadreta}}} \cdot \frac{1}{2}(\text{quadreta})^{-\frac{1}{2}} \cdot \frac{1}{2a^2}\left[-2x + \frac{1}{2}(\text{bsqreta})^{-\frac{1}{2}} \cdot (4x^3 + 4xz^2 - 4xa^2)\right] \tag{2.38}$$

Similarly, we can solve for the partial derivative of η with respect to z.

$$\frac{\partial \eta}{\partial z} = \frac{1}{\sqrt{1-\text{quadreta}}} \cdot \frac{1}{2}(\text{quadreta})^{-\frac{1}{2}} \cdot \frac{1}{2a^2}\left[-2z + \frac{1}{2}(\text{bsqreta})^{-\frac{1}{2}} \cdot (4z^3 + 4zx^2 + 4za^2)\right] \tag{2.39}$$

The process for taking the partial derivatives of ξ with respect to x and z is very similar. We begin with identities, then use the quadratic equation to gain an expression for ξ in terms of x and z only.

$$\frac{x^2}{a^2\cos^2\xi} + \frac{z^2}{a^2\sin^2\xi} = 1 \tag{2.40}$$

$$\cosh^2\xi - \sinh^2\xi = 1 \tag{2.41}$$

$$x^2a^2\sinh^2\xi + z^2a^2(1 + \sinh^2\xi) = a^2(1 + \sinh^2\xi) \cdot a^2\sinh^2\xi \tag{2.42}$$

$$a^2\sinh^4\xi + (a^2 - x^2 - z^2)\sinh^2\xi - z^2 = 0 \tag{2.43}$$

$$\sinh^2\xi = \frac{-a^2 + x^2 + z^2 \pm \sqrt{(a^2 - x^2 - z^2)^2 - 4(a^2 \cdot (-z^2))}}{2a^2} = X_\xi \tag{2.44}$$

$$\xi = \sinh^{-1}\sqrt{X_\xi} \tag{2.45}$$

Once again, using the chain rule, we can easily solve for $\frac{\partial \xi}{\partial x}$.

$$\frac{\partial y}{\partial x} = \frac{\partial y}{\partial n} \cdot \frac{\partial n}{\partial x} \tag{2.46}$$

$$y = \sinh^{-1}\sqrt{n} \qquad n = \sqrt{X_\xi} \tag{2.47}$$

$$\frac{\partial y}{\partial n} = \frac{1}{\sqrt{1+n^2}} \qquad \frac{\partial n}{\partial x} = \frac{1}{2}(X_\xi)^{-\frac{1}{2}} X_\xi' \tag{2.48}$$

$$n^2 = X_\xi \tag{2.49}$$

$$X_\xi' = \frac{1}{2a^2}\left[2x + \frac{1}{2}(a^4 - 2a^2x^2 + 2a^2z^2 + 2x^2z^2 + x^4 + z^4)^{-\frac{1}{2}} \cdot (-4a^2x + 4z^2x + 4x^3)\right] \tag{2.50}$$

$$\text{bsqr} = a^4 - 2a^2x^2 + 2a^2z^2 + 2x^2z^2 + x^4 + z^4 \tag{2.51}$$

$$\text{quad} = \frac{-a^2 + x^2 + z^2 \pm \sqrt{a^4 - 2a^2x^2 + 2a^2z^2 + 2x^2z^2 + x^4 + z^4}}{2a^2} \tag{2.52}$$

$$\frac{\partial \xi}{\partial x} = \frac{1}{\sqrt{1+\text{quad}}} \cdot \frac{1}{2} \cdot (\text{quad})^{-\frac{1}{2}} \cdot \frac{1}{2a^2}\left(2x + \frac{1}{2}(\text{bsqr})^{-\frac{1}{2}} \cdot (-4a^2x + 4z^2x + 4x^3)\right) \tag{2.53}$$

$$\frac{\partial \xi}{\partial z} = \frac{1}{\sqrt{1+\text{quad}}} \cdot \frac{1}{2} \cdot (\text{quad})^{-\frac{1}{2}} \cdot \frac{1}{2a^2}\left(2z + \frac{1}{2}(\text{bsqr})^{-\frac{1}{2}} \cdot (4a^2z + 4x^2z + 4z^3)\right) \tag{2.54}$$

APPENDIX C: FLUID FLOW MODEL FOR PRESSURE DIFFUSION

Our half-space fluid flow model (Equation 2.55) is based on the heat flow equation (Bird et al., 1960), and consists of a saturated overpressured mud overlying a normally pressured sand (Figure 2.4). Water is the only phase present in the system and there is a constant pressure boundary condition at the sand-mud interface.

$$P^*_{md}(t,y) = (P^*_{md0} - P^*_{sd0}) \cdot 2 \sum_{n=0}^{\infty} \frac{(-1)^n}{\left(n+\frac{1}{2}\right)\pi} e^{-\left(n+\frac{1}{2}\right)^2 \pi^2 \alpha t / b^2} \cos\left(n+\frac{1}{2}\right)\frac{\pi y}{b} \tag{2.55}$$

In Equation 2.55, P^*_{md0} and P^*_{sd0} are overpressure in the mud and sand at initial conditions; b is the half-thickness of the mud layer (Figure 2.4). Conductivity of the mud, α, is calculated from intrinsic permeability, mud porosity, fluid density and viscosity, and fluid and matrix compressibility (Equation 2.56).

$$\alpha = \frac{(1-\phi)^2 k \rho_f g}{\mu\left(\frac{\phi\beta}{1-\phi} + \phi\beta_f\right)} \tag{2.56}$$

CHAPTER 3

Consolidation State, Permeability, and Stress Ratio as Determined from Uniaxial Strain Experiments on Sand and Mud Samples from the Eugene Island 330 area, Offshore Louisiana

ABSTRACT

Uniaxial strain experiments conducted on mud from overpressured horizons in the Eugene Island 330 field (Gulf of Mexico) reveal information about consolidation state, compaction behavior and permeability. Experimentally-derived maximum past stress is within 25 psi of estimated current *in situ* stress for a sample from the A-12 well, indicating that this sediment has undergone uni-directional strain (i.e. a history of increasing effective stress). A second sample, from the A-20ST2 (Pathfinder) well, reveals a maximum past stress which is 200 psi greater than current stress, implying that effective stress may have decreased at depth in this layer. Laboratory measurements of stress ratio, K_0 (0.85, 0.86) compare well with *in situ* measurements made during leak-off and stress tests (0.84, 0.91). The high stress ratio values indicate that these sediments are deforming plastically at *in situ* levels of effective stress. The change in slope of the stress-strain curve following yield supports the observation of plastic deformation. Direct measurements of mud permeability at *in situ* levels of effective stress reveal layer-parallel and layer-perpendicular permeability of 5.32×10^{-4} mD (5.25×10^{-19} m^2) and 1.17×10^{-4} mD (1.15×10^{-19} m^2), respectively. Compression index values (slope of void ratio-vertical effective stress curve)

for mud samples were 0.27, 0.29, significantly lower than the compression index calculated from a wireline relationship (0.5).

INTRODUCTION

A typical assumption is that strain in a geologic basin is uniaxial and net lateral strain is approximately zero (Roegiers, 1989). We use the uniaxial strain assumption to replicate geologic deformation in the laboratory (Karig and Hou, 1992; Karig, 1996).

Deformation behavior of an uncemented sample in the laboratory is controlled by stress history and physical properties. Therefore, deformation experiments give us insight into the state and evolution of *in situ* stress. Uniaxial strain experiments provide an estimate of the maximum past stress an undisturbed sample has been subjected to. Using this estimate of maximum past stress, we assess the consolidation state and stress history of the sample.

Laboratory tests on undisturbed samples provide further insight into compaction behavior and elastic properties by providing continuous measurements of stress ratio, K_0, defined here as the slope of the horizontal effective stress-vertical effective stress curve (Karig and Morgan, 1994). Table 1 shows all of the nomenclature used in this chapter. We compare experimental values of K_0 with stress ratios calculated from leak-off tests and fracture completions in this area.

Direct permeability measurements at *in situ* levels of effective stress indicate that these muds have permeability on the order of 10^{-19} m^2 (10^{-4} mD).

In this chapter, we present methods for uniaxial strain experiments and permeability tests. We then present results of these experiments and compare the experimental

Table 3.1: Nomenclature

Variable	Property	Units
A	sample cross-sectional area	L^2
c	intercept of e-σ_v regression	dimensionless
c_c	compression index	LT^2/M
c_r	recompression index	LT^2/M
c_v	coefficient of consolidation	L^2/T
d	sample drainage length	L
e	void ratio	L^3/L^3
f	acoustic formation factor	dimensionless
g	gravitational acceleration	L/T^2
h	hydraulic head	L
H_0	initial sample height	L
k	permeability	L^2
K	hydraulic conductivity	L/T
K_0	stress ratio, $\Delta\sigma_h / \Delta\sigma_v$	dimensionless
l	sample length	L
m_v	coeff. of volume compressibility	L^2T^2/M
p’	mean effective stress	M/LT^2
P_f	fluid pressure	M/LT^2
q	differential stress	M/LT^2
Q	volumetric flow rate	L^3/T
S_v	vertical stress	M/LT^2
T_{90}	time at which 90% consolidation has occurred	T

Table 3.1: Nomenclature

Variable	Property	Units
v_p	compressional wave velocity	L/T
ΔP_f	P_f difference across the sample	M/LT^2
Δt	wireline-measured transit time	T/L
Δt_{ma}	matrix transit time	T/L
ε	strain	L^3/L^3
γ_w	unit weight of water	M/L^2T^2
ϕ	porosity	L^3/L^3
ϕ_i	initial sample porosity	L^3/L^3
μ	fluid viscosity	M/LT
ν	Poisson ratio	dimensionless
ρ_{bi}	initial sample bulk density	M/L^3
ρ_f	fluid density	M/L^3
ρ_g	grain density	M/L^3
σ_c	preconsolidation stress	M/LT^2
σ_h	horizontal effective stress	M/LT^2
σ_v	vertical effective stress	M/LT^2

results with *in situ* measurements and previous studies. We discuss factors which affect laboratory and *in situ* measurements and close with implications of our findings.

METHODS

Sample Description

Conventional core taken from three wells in the Eugene Island 330 field (Figure 3.1) provided sand and mud samples for the deformation experiments. Samples were taken from two different effective stress regimes. The A-14ST core was taken in moderate overpressure above the KE reservoir sand (Figure 3.2a) (see Alexander and Flemings (1995) for a stratigraphic description of this area). The A-12 and A-20ST2 samples were taken from the severely overpressured zone adjacent to the Lentic 1 sand (Figures 3.2b,c).

At the depth of the A-14ST sample (T99), fluid pressure in the mud, estimated from a porosity-effective stress method (Hart et al., 1995), is 22.9 MPa (3325 psi). Vertical (overburden) stress (S_v) at sample depth, calculated by integrating the bulk density log, is 44.8 MPa (6495 psi). Therefore, *in situ* vertical effective stress (σ_v) at sample depth in the A-14ST is 21.9 MPa (3170 psi). Fluid pressure in the nearby KE-1 sand is 29.6 MPa (4302 psi). Table 2 contains a complete description of all of the core samples.

The A-12 core was subsampled between the severely overpressured Lentic 1 upper and lower sands (Figure 3.2b). Fluid pressure in the mud at the depth of the A-12 (T96) sample is 35.0 MPa (5080 psi; 14.6 lb/gal EMW). Overburden, calculated from wireline bulk density is 42.1 MPa (6105 psi); *in situ* vertical effective stress is 7.1 MPa (1025 psi). The A-12 sand sample, taken from the Lentic 1 lower horizon at a depth of 2082 m (6830 ft), has an *in situ* fluid pressure of 36.2 MPa (5254 psi; 15.0 lb/gal EMW).

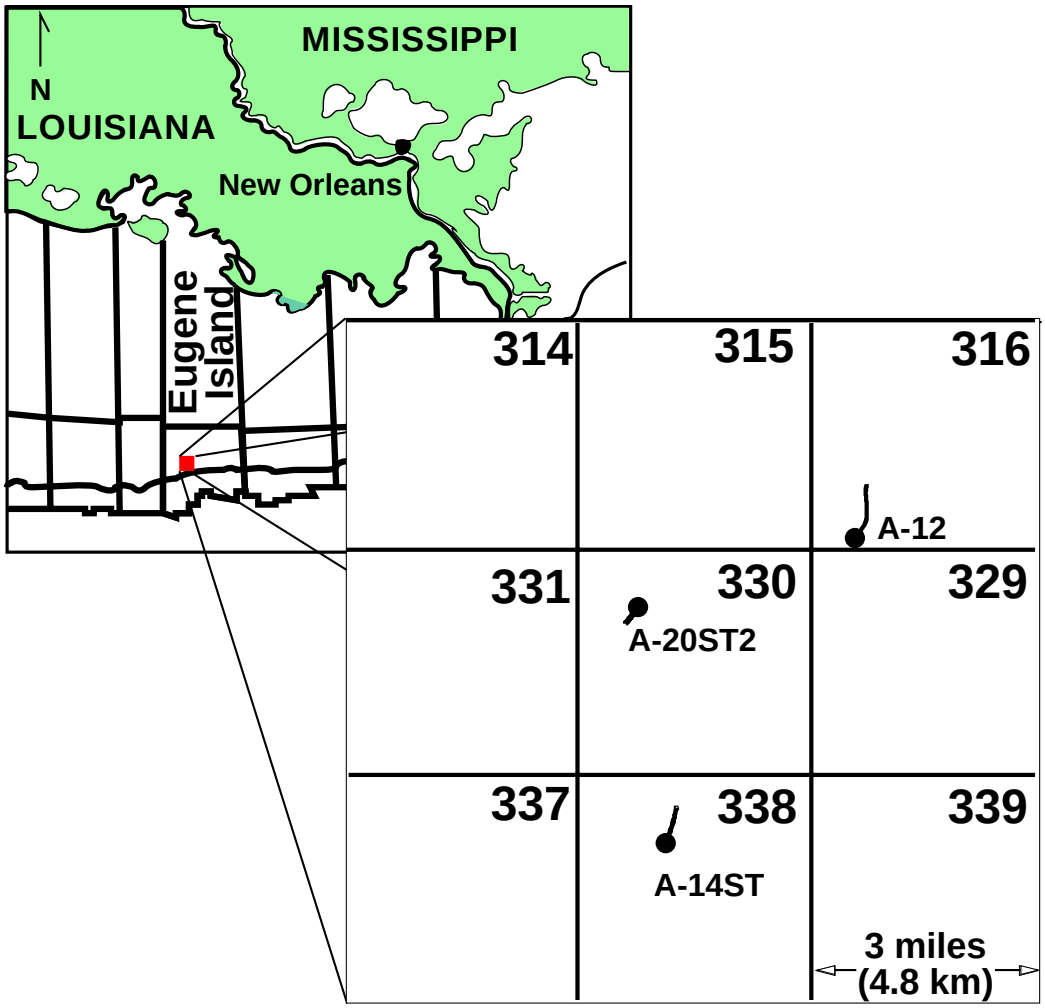

Figure 3.1: Basemap locates cored wells from which laboratory samples were taken. Circles indicate bottom hole location. The A-20ST2 (Pathfinder) well was cored in 1993; 343 feet of core was recovered (95% recovery). In 1994, 43.2 feet of core was recovered from the A-12 well (34% recovery). The A-14ST core was taken in 1993; 30.1 feet of core was recovered (72%). All of the 4-inch diameter cores were cut into 3-foot sections and then stabilized in the core barrels using a quick-hardening epoxy resin. Cores were then slabbed into one-third and two-thirds portions. Laboratory samples were taken from the two-thirds portion. Slabs were archived in cold storage at Core Labs (Houston) and then moved to Penn State, where they are stored in a humid, chilled room. The A-20ST2 core was sealed in wax to preserve moisture.

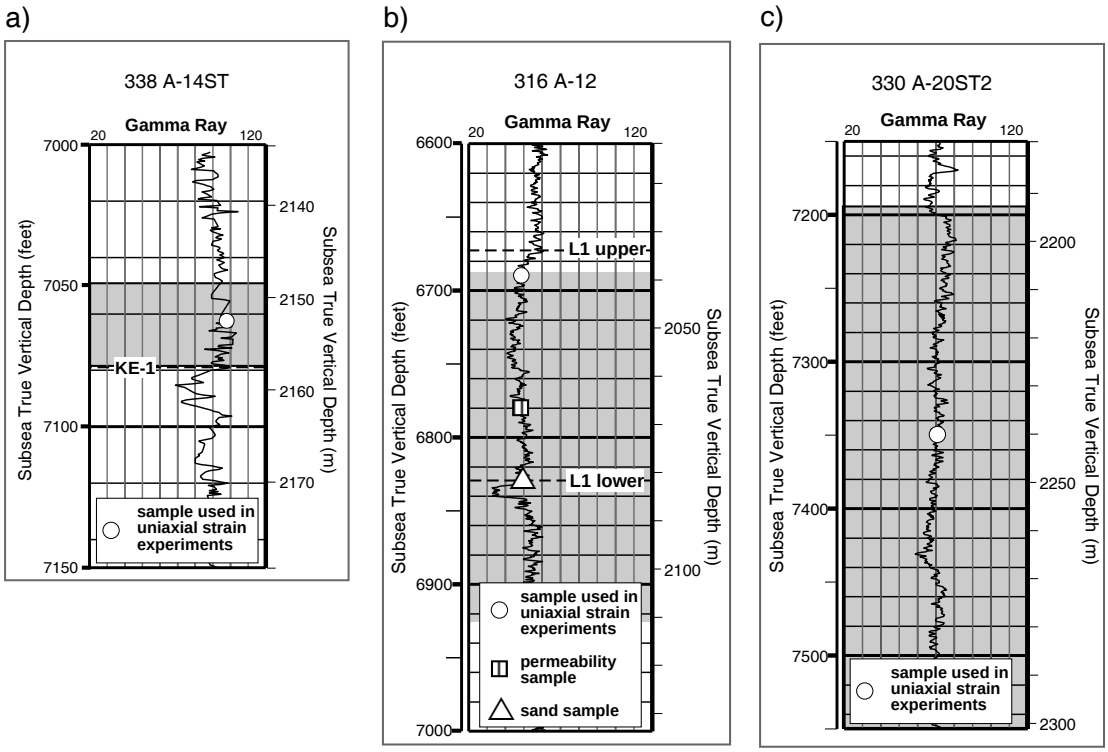

Figure 3.2: Cylindrical laboratory samples were drilled perpendicular to bedding at locations denoted with circles. Gray area represents entire cored interval. a) A-14ST (T99) sample is 51.56 mm long, 30.48 mm in diameter, with an initial porosity of 0.28. Sample contains 35% quartz, 51% clays. See Table 2 for detailed lithologic description. b) A-12 mud (T96) sample (located by circle) is 63.5 mm long, 31.01 mm in diameter. Initial porosity is 0.39. Sample was taken from core barrel #1 and contains 38% quartz, 39% clay, with small fractions of potassium feldspar, plagioclase, and calcite (Core Laboratories, 1994). A laser particle size analysis revealed 2.5% fine-grained, 15.4% very fine-grained, 62.1% silt-size, and 20.0% clay-size particles. Disaggregated sand (C43) sample was taken from the Lentic 1 lower sand (triangle). The C43 sample contains 0.8% medium-grained, 15.1% fine-grained, 65.7% very fine-grained, 14.8% silt-size, and 3.6% clay-size particles (Core Laboratories, 1994). Permeability sample P01 (taken parallel to bedding) is 41.28 mm long with a diameter of 30.99 mm. Permeability sample P03 (taken perpendicular to bedding) is 16.54 mm long, 31.04 mm in diameter. Permeability samples were taken from core barrel #4. c) A-20ST2 sample is 52.73 mm long, 30.94 mm in diameter, with an initial porosity is 0.37. Sample contains 35% quartz and 54% clay (Losh et al., 1994).

Table 3.2: Sample Description

Well	Sample Number	Subsea True Vertical Depth	Composition	*in situ* P_f (psi)	*in situ* σ_v (psi)	*in situ* K_0
338 A-14ST	T99	7063’ (2153 m)	35% quartz, 51% clays	3323 (22.9 MPa)	3170 (21.9 MPa)	0.54 (6795’)
316 A-12	T96	6690’ (2039 m)	38% quartz, 5% potassium feldspar, 9% plagioclase, 3% calcite, 1% dolomite, 39% clays (48% illite, 38% smectite, 7% kaolinite, 8% chlorite)	5080 (35.0 MPa)	1025 (7.1 MPa)	0.91 (6690’)
316 A-12	C43	6830’ (2082 m)	63%quartz, 7% potassium feldspar, 18% plagioclase, 2% dolomite, 1% siderite, 9% clays (76% illite, 22% smectite, 2% kaolinite)	5254 (36.2 MPa)	1005 (6.9 MPa)	0.43 (6798’)
316 A-12	P01 and P03	6781’ (2067 m)	40% quartz, 1% potassium feldspar, 9% plagioclase, 2% pyrite, 48% clays (45% illite, 35% smectite, 7% kaolinite, 12% chlorite)	5166 (35.6 MPa)	1045 (7.2 MPa)	0.43 (6798’)
330 A-20ST2	T77	7350’ (2240 m)	35% quartz, 8% potassium feldspar, 3% plagioclase, 54% clays (52% illite, 32% smectite, 15% kaolinite, 1% chlorite)	5730 (39.5 MPa)	1052 (7.3 MPa)	0.84 (7277’)

The A-20ST2 (T77) sample (Figure 3.2c) was taken between the *Cris S* mud and the Lentic 1 sand (Alexander and Flemings, 1995). Estimated fluid pressure in this mud interval is 39.5 MPa (5730 psi; 15.0 lb/gal EMW). Calculated S_v is 46.8 MPa (6782 psi). Therefore, *in situ* vertical effective stress in the A-20ST2 at 2240 m (7350 ft) is 7.3 MPa (1052 psi).

Experiment Description

K_0 tests

A K_0 test is a consolidation experiment conducted under uniaxial strain conditions. Our experiments were conducted at a constant room temperature of 73^{o}F in a triaxial computer-controlled servo-hydraulic load frame at Cornell University (Figure 3.3). An initial isotropic stress state at the onset of the experiment, at effective stress levels well below anticipated sample yield, minimizes pre-shearing of the sample (Mesri and Hayat, 1993). After the sample has stabilized (for a period of 24-48 hours), the experiment proceeds under uniaxial strain conditions.

Experiment duration was determined, in part, by the length of time necessary to reach yield. The durations of the T96 (A-12 mud) and T77 (A-20ST2) were 8 days and 13 days, respectively. The T99 experiment (A-14ST) was halted after 18 days, prior to sample yield, because of mechanical limitations.

All experiments were run under axial load control at a rate of 0.1 psi/min (approximate strain rate of 1×10^{-7} s^{-1}). A load control experiment is advantageous because as consolidation proceeds and the sample compresses, sample compressibility decreases. The decrease in compressibility causes the strain rate to decrease. In low-permeability sedi-

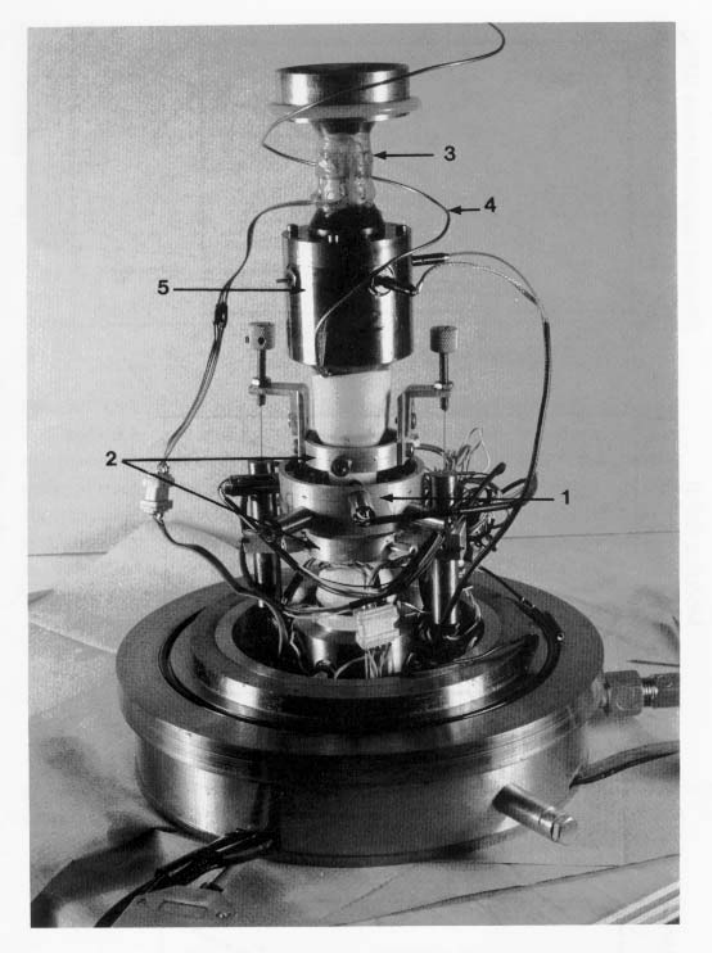

Figure 3.3: Photograph shows configuration for triaxial experiment. 1) LVDTs around the sample measure radial strain. 2) LVDT at top measures axial strain. 3) A servo-hydraulic load cell mounted on top of the apparatus measures axial stress. 4) Expelled fluid drains freely from both ends of the sample, through porous titanium plates. 5) Transducers embedded in the platens allow us to measure compressional velocity (v_p) during the experiment (from Karig, 1996).

ments such as these muds, a slower strain rate is preferable to allow more time for fluid dissipation (Karig, 1996). Sintered titanium disks with 2 μm pore spaces allow fluid drainage from the top and bottom of the cell during consolidation. Linear variable-displacement transducers (LVDT) measure axial strain. Karig (1996) presents a full description of the apparatus used in these experiments.

Jacob's (1949) relation provides a method for calculating porosity changes from strain, ε, during these experiments.

$$\varepsilon = \frac{d\phi}{1-\phi} \tag{3.1}$$

By substituting $d\phi = \phi_i - \phi$ and rearranging, we get an expression for porosity as a function of initial porosity (ϕ_i) and axial strain.

$$\phi = \frac{\phi_i - \varepsilon}{1-\varepsilon} \tag{3.2}$$

Initial porosity is calculated in the laboratory using initial bulk density (ρ_{bi}), pycnometer-derived grain density (ρ_g) and an assumed fluid (brine) density (ρ_f) of 1.07 g/cm^3.

$$\phi_i = \frac{\rho_g - \rho_{bi}}{\rho_g - \rho_f} \tag{3.3}$$

Void ratio (e), used to graphically determine consolidation state, is a function of porosity.

$$e = \frac{\phi}{1-\phi} \tag{3.4}$$

Unlike the mud samples (T77, T96, T99), the A-12 sand sample (C43) was non-cohesive. We consolidated the disturbed sand sample in a steel oedometer cell (Figure

3.4). The disaggregated nature of the sample prevented us from determining the maximum past stress, but we were able to measure K_0 for comparison to the mud samples. Porous plates provide drainage at both ends of the sample and an LVDT measures axial strain. During an oedometer test, the axial load is increased and held for a period of time, rather than increasing in constant load increments. A pressure transducer embedded in the cell wall measures lateral stress (Figure 3.4). At the beginning of each load increment, the increase in lateral stress approximates the increase in axial stress. As pore fluid flows from the sample, the measured lateral stress decreases and approaches the effective lateral stress (Karig and Hou, 1992). We wait for the measured lateral stress to stabilize before increasing the axial load, in order to get an accurate measurement of horizontal effective stress.

The A-12 sand sample remained non-cohesive at the end of the experiment, so it was difficult to obtain an accurate final weight. We used the final sample volume (measured in the cell), the dry sediment weight, and the grain density to calculate a final porosity of 0.348. We then back-calculated changes in porosity during consolidation.

Permeability tests

Muds in the E.I. 330 area act as seals to pressure and hydrocarbon migration. Permeability measurements in mud allow us to evaluate seal integrity and estimate timescales of overpressure dissipation. Laboratory experiments provide two methods of determining permeability. Direct determination involves observing the rate of fluid flow through a sample of known length. Permeability can also be measured indirectly during consolidation tests by observing the decline in strain after application of an instantaneous load.

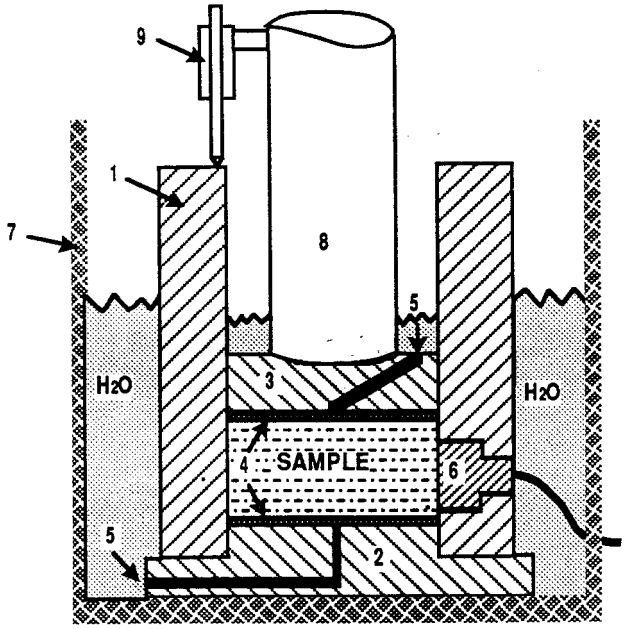

Figure 3.4: Sketch shows oedometer cell used for uniaxial strain experiment on the A-12 sand (adapted from Karig and Hou, 1992). Configuration consists of steel cell walls (1), basal (2) and upper platens (3), which contain filter discs (4) through which expelled pore fluid drains (5). Lateral stress is measured by a transducer (6) embedded in the cell wall. Outer container (7) holds water to keep the sample from absorbing air when the load is decreased. Axial load is applied with a ram (8) which is attached to an LVDT (9) to measure axial strain.

Direct (constant head test)

A constant head test allows direct determination of permeability. During this experiment, constant fluid pressure is held at one end of the sample; the outflow end is kept at atmospheric pressure. We calculate permeability from the flow rate through the sample. Specifically, we calculate hydraulic conductivity, K, from Darcy's Law.

$$\frac{Q}{A} = -K\left(\frac{\Delta h}{\Delta l}\right) \tag{3.5}$$

Using the definition of hydraulic head, h, and substituting the expression for hydraulic conductivity (Equation 3.6) into Equation 3.5, we get an expression for permeability, k (Equation 3.7).

$$K = \frac{k\rho_f g}{\mu} \tag{3.6}$$

$$k = \frac{Q\mu}{A}\frac{\Delta l}{\Delta P_f} \tag{3.7}$$

In Equation 3.7, A and Δl are the cross-sectional area and length of the sample, μ is fluid viscosity, Q is the measured flow rate under steady-state conditions, and ΔP_f is the difference in fluid pressure across the length of the sample.

Laboratory measurements of permeability in low-permeability sediments are often wrought with errors. As elucidated by Tavenas et al. (1983), the identification and elimination of potential errors are the key to accurate direct permeability measurements. Leakage through the external fitting is perhaps the largest and most unavoidable source of error. We attempt to quantify this error by running leak rate tests in the cell containing no sample. Osmosis and diffusion through the latex sleeve can also introduce error into the measurements. Surrounding the sample with silicone oil reduces osmotic effects. A third

source of error may be preferred flow between the latex sleeve and the sample (i.e. without having passed through sample) (Tavenas et al., 1983). A confining pressure (800, 1000 psi) on the sample minimizes this type of flow.

Gas bubbles which have come out of solution during unloading of the sample (i.e. as core was brought to the surface) may block pore throats and hinder flow, thus decreasing the permeability of the sediment (Bryant et al., 1975). Our experiments were run with an inflow fluid pressure ranging from 49 to 150 psi, to drive any exsolved gas bubbles back into solution. Osmotic effects caused by introducing freshwater into the marine sediment sample may also decrease the apparent permeability of the sample (Neuzil, 1986). Use of a saline brine (35 ppt) minimizes these effects in our experiments.

In order to account for the transient nature of the flow at the beginning of the test (Olsen et al., 1985), we allow the test to equilibrate and reach steady-state flow before measuring flow rate for calculations of permeability. However, it is difficult to pinpoint the transition from transient to steady-state flow. Ideally, we consider the system to be at steady-state when volume in equals volume out. In practice, it is difficult to quantify the volume expelled from the sample. We determine that the system has reached steady-state when the expelled volume begins to increase steadily and the input volume increases linearly with time.

Indirect (consolidation test)

Consolidation is the change in volume resulting from pore fluid expulsion under an applied load (Atkinson, 1992). Previous authors have used fluid expulsion during consolidation to calculate the permeability of a sediment (Terzaghi, 1925; Bryant et al.,

1975). During a consolidation experiment, after axial load is increased instantaneously and held, most of the observed strain results from fluid flow out of the sample. Hydraulic conductivity of the sample, which dictates the rate of fluid expulsion, is a function of the coefficient of consolidation (c_v), the coefficient of volume compressibility (m_v), and the unit weight of water (γ_w).

$$K = c_v m_v \gamma_w \tag{3.8}$$

The coefficient of consolidation is controlled by the distance from a drainage boundary (d) and T_{90}, the time at which 90% consolidation is achieved. T_{90} is determined graphically by the square root of time method (Taylor, 1948).

$$c_v = \frac{0.848 d^2}{T_{90}} \tag{3.9}$$

The coefficient of volume compressibility is the ratio of the change in sample height to increase in stress divided by the initial height of the sample, H_0.

$$m_v = \frac{1}{H_0}\left(\frac{H_0 - H_1}{\sigma_{v1} - \sigma_{v0}}\right) \tag{3.10}$$

The accuracy of the indirect method for determining permeability relies on a number of assumptions. The first assumption is that strains are small and one-dimensional. Deformation in the laboratory is restricted to uniaxial strain by constraining the sample laterally. The second assumption is sample saturation. Certain assumptions are also made about the physical properties of the sample. These assumptions include fluid and grain incompressibility, soil homogeneity, and a linear relationship between stress and strain. The assumption of grain and fluid incompressibility allows the interpretation of all strain

as a direct result of the sediment compressibility (i.e. directly related to the rate of fluid expulsion). From this assumption, it follows that all of the consolidation which occurs is primary, and that the sample does not creep. Preliminary creep tests on samples from the E.I. 330 area (Karig, pers. comm.) suggest that some creep is occurring during and after primary consolidation. Therefore, not all of the strain is due to fluid expulsion, and some error will be introduced into the permeability calculation. All fluid flow is presumed to follow Darcy's Law. The final assumption, which may be the greatest source of error, is that compressibility and permeability are constant during consolidation. We have stated previously that we infer compressibility to decrease during consolidation, thereby decreasing the strain rate during a constant load rate test. Therefore, the error of this final assumption is inherent in indirect calculations of permeability.

RESULTS

Determination of maximum past stress

A graphical method developed by Casagrande (1936) provides a means of determining the maximum past effective stress experienced by an undisturbed, uncemented sample, termed preconsolidation stress (σ_c) (Figure 3.5a). If the laboratory experiment replicates the deformation path followed by the sediment during burial, the observed stress at sample yield corresponds to the sample's preconsolidation stress (Karig and Morgan, 1994). Sample yield is defined as the break in slope of the stress-strain curve, which denotes the transition between elastic reconsolidation and first-time consolidation (Karig and Morgan, 1994).

The preconsolidation stress for the A-12 mud (T96) sample is 7.2 MPa (1046 psi)

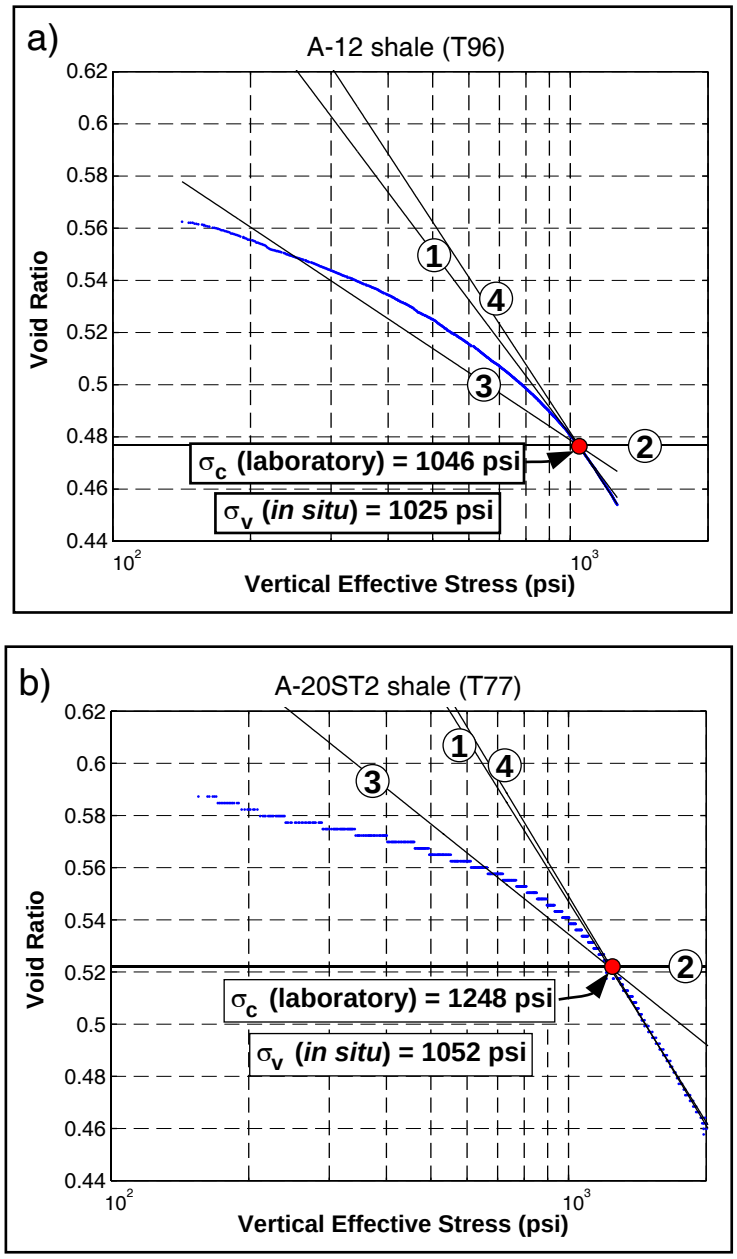

Figure 3.5: Maximum past stress (preconsolidation stress, σ_c, is determined using Casagrande's (1936) graphical method. First, we plot void ratio versus vertical effective stress on log-linear axes and determine the point of maximum curvature. The point of maximum curvature is determined mathematically, by discretely calculating the change in slope of the curve. We then draw a tangent (1) and a horizontal line (2) through that point. Third, we bisect (3) the angle formed by the tangent and horizontal lines and then draw a linear regression (4) through the first-time consolidation (post-yield) portion of the curve. The vertical effective stress at the intersection of the bisector (3) and the linear regression (4) denotes the maximum past effective stress experienced by the sample (e.g. σ_c). a) For the A-12 (T96), σ_c is within 0.2 MPa (25 psi) of *in situ* σ_v. b) In the A-20ST2 (T77), experimental σ_c is approximately 1.4 MPa (200 psi) greater than *in situ* σ_v.

(Figure 3.5a). For the A-20ST2 sample (T77), the experimentally-derived σ_c is 8.6 MPa (1248 psi) (Figure 3.5b). The A-14ST experiment was halted due to mechanical limitations, prior to reaching the sample's preconsolidation stress. Table 3 presents a summary of results from the K_0 experiments.

Stress ratio, K_0

K_0, referred to as the coefficient of earth pressure at rest (Brooker and Ireland, 1965) is the ratio between horizontal effective stress and vertical effective stress under uniaxial strain conditions (Jones, 1994). We calculate K_0 as the slope of the σ_h-σ_v curve.

$$K_0 = \frac{\Delta\sigma_h}{\Delta\sigma_v} \tag{3.11}$$

K_0 increased in the A-12 (T96) and A-20ST2 (T77) experiments following sample yield (Figures 3.6a,b). In the A-12 (T96) sample (Figure 3.6a), at vertical effective stress less than σ_c, K_0 is 0.52. At larger values of vertical effective stress, K_0 is 0.86. Similarly, in the A-20ST2 (T77), K_0 increased from 0.63 to 0.85 following σ_c (Figure 3.6b). In the A-14ST sample, which was not tested to sample yield, K_0 of reconsolidation was 0.37 (Figure 3.6c). In the disaggregated A-12 sand (C43) sample, K_0 for first-time consolidation was 0.43 (Figure 3.6d).

Permeability

Constant head permeability tests on samples from the A-12 well provided estimates of layer-parallel (P01) and layer-perpendicular (P03) mud permeability. During each test, a constant fluid pressure was held at the inflow end, while the outflow end of the sample was kept at atmospheric pressure. Therefore, ΔP_f, the fluid pressure difference

.

Table 3.3: Summary of Deformation Experiment results

Well	Sample	Subsea True Vertical Depth	σ_c (psi)	pre-yield K_0	post-yield K_0	C_r	C_c
338 A-14ST	T99	7063’ (2153 m)	N/A	0.371 ν=0.27	N/A	0.05	N/A
316 A-12	T96	6690’ (2039 m)	1046 (7.2 MPa)	0.52 ν=0.34	0.86 ν=0.46	0.10	0.27
316 A-12	C43	6830’ (2082 m)	N/A	0.434 ν=0.30	N/A	N/A	N/A
330 A-20ST2	T77	7350’ (2240 m)	1248 (8.6 MPa)	0.63 ν=0.39	0.85 ν=0.46	0.07	0.29

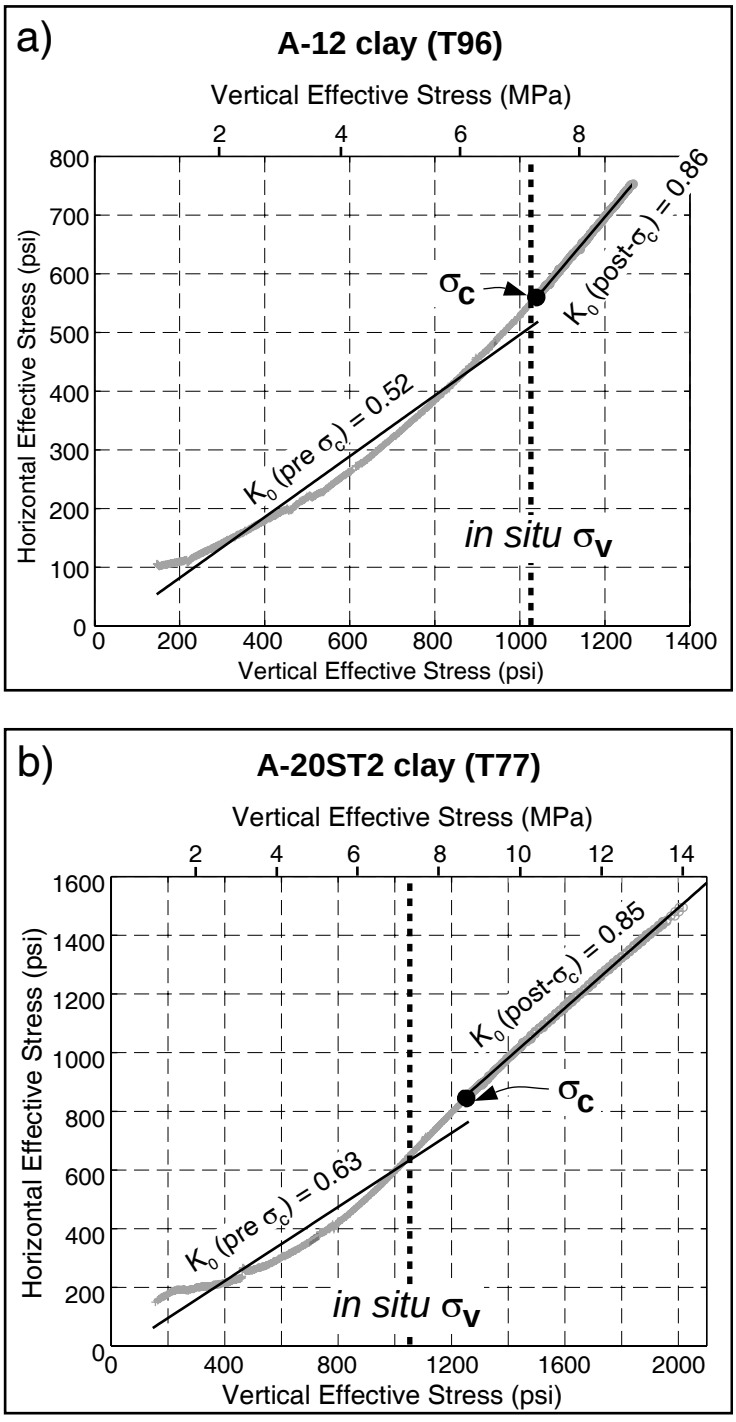

Figure 3.6: Stress ratio K_0 is calculated as the slope of horizontal versus vertical effective stress. a) In the A-12 (T96), pre-σ_c K_0 is 0.52; post-σ_c K_0 is 0.86. Dotted line denotes *in situ* σ_v; circle represents experimental σ_c. b) In the A-20ST2 (T77) sample, K_0 increased from 0.63 to 0.85.

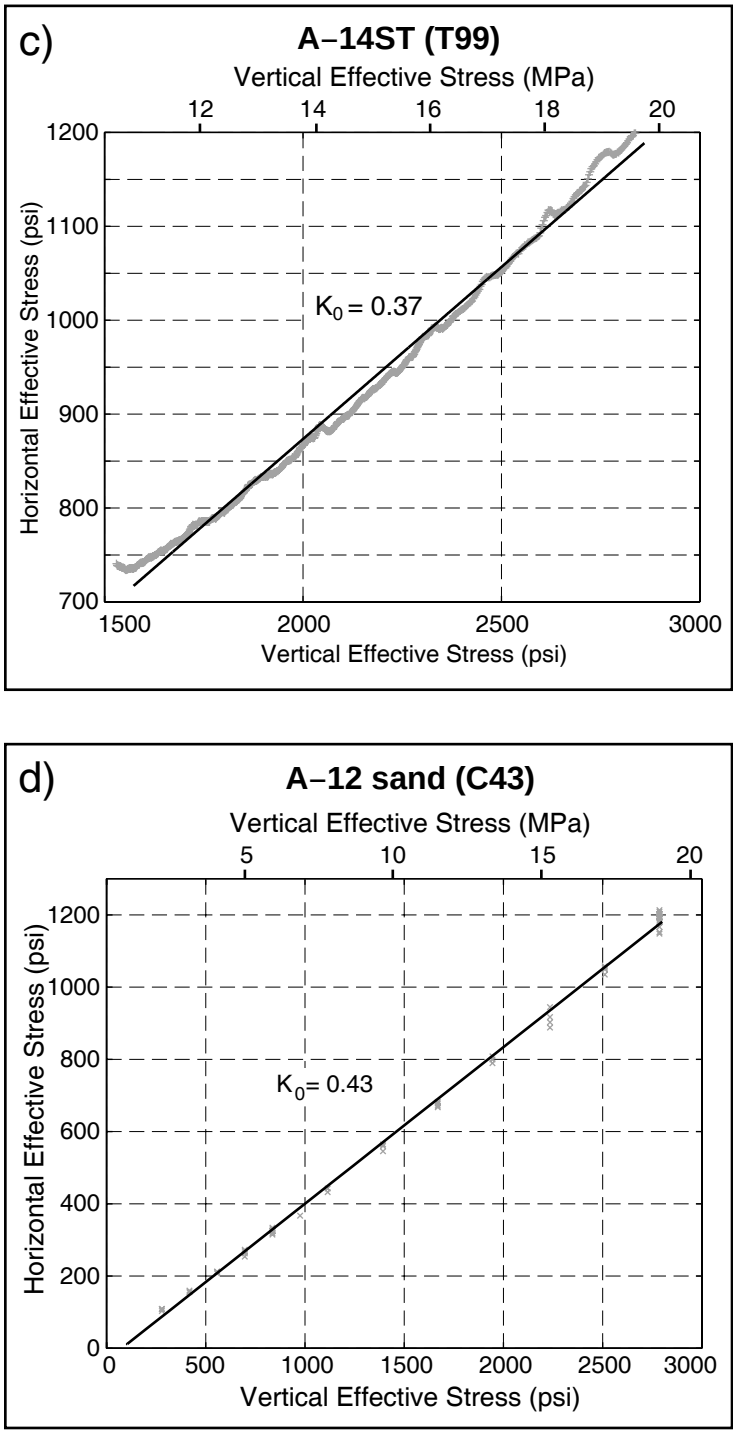

Figure 3.6: c) K_0 for the A-14ST (reconsolidation) is 0.37. d) K_0 for the A-12 (C43) disaggregated sand sample (first-time consolidation) is 0.43.

across the length of the sample, is equal to the fluid pressure at the inflow end.

During the P01 experiment, flow rate was monitored at ΔP_f of 0.34 and 0.66 MPa (49 and 96 psi) (Figure 3.7a). Confining pressure remained at 6.9 MPa (1000 psi) for the duration of the experiment. Layer-parallel permeability at ΔP_f of 0.34 MPa is 8.08 x 10^{-19} m^2 (8.19 x 10^{-4} mD). At ΔP of 0.66 MPa, permeability is 2.41 x 10^{-19} m^2 (2.44 x 10^{-4} mD). Average layer-parallel permeability at the two different fluid pressures, is 5.25 x 10^{-19} m^2 (5.32 x 10^{-4} mD).

The layer-perpendicular sample, P03 (Figure 3.7b), was tested at a confining pressure of 800 psi, for a series of fluid pressures. Layer-perpendicular permeability measurements are 1.42 x 10^{-19} m^2 at 0.35 MPa, 1.14 x 10^{-19} m^2 at 0.52 MPa, 9.29 x 10^{-20} m^2 at 0.70 MPa and 1.10 x 10^{-19} m^2 at 1.03 MPa, for an average of 1.15 x 10^{-19} m^2 (1.17 x 10^{-4} mD).

Two leak rate tests, run at a variety of ΔP_f, identified leak rates of 0.042 and 0.048 mL/hr. Accounting for the leak rate into the system changes our permeability values for P01 and P03 to 3.82 x 10^{-19} m^2 and 6.47 x 10^{-20} m^2 (3.87 x 10^{-4} and 6.56 x 10^{-5} mD), respectively.

Compression Index

Compression index (c_c) is the change in void ratio for a change in vertical effective stress, during primary (first-time) consolidation (Equation 3.12).

$$e = c_c \log(\sigma_v) + c \tag{3.12}$$

We calculate c_c as the slope of the void ratio-vertical effective stress curve, plotted on log-linear axes. The recompression index (c_r) of a sediment during reloading (e.g. at

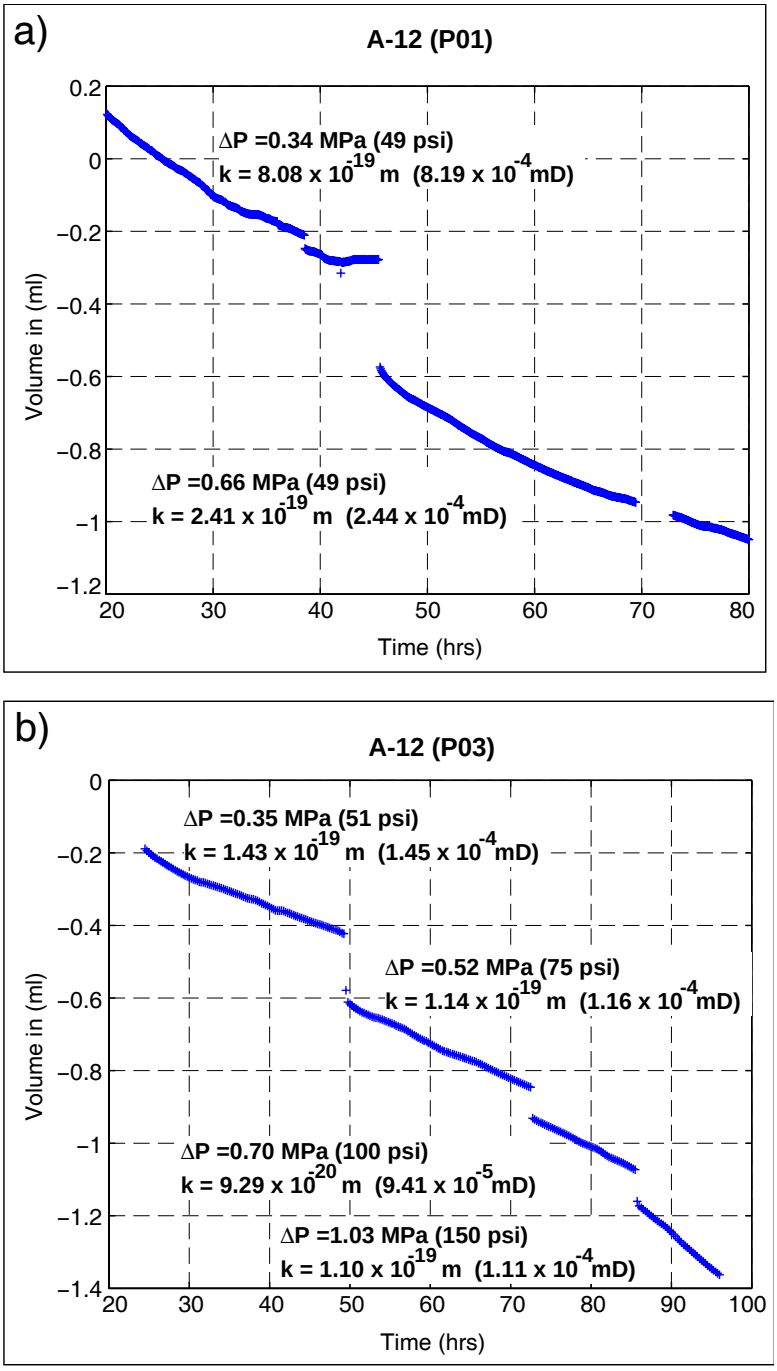

Figure 3.7: a) Direct measurements of layer-parallel (P01) permeability yield an average permeability of 5.25 x 10^{-19} m^2 (5.32 x 10^{-4} mD). Initial porosity of P01 sample is 0.40; final porosity was difficult to determine because sample was misshapen upon removal from cell. b) Average layer-perpendicular permeability (P03) is 1.15 x 10-19 m2 (1.17 x 10^{-4} mD). During the P03 experiment, porosity decreased from 0.48 to 0.38.

stresses less than σ_c) is consistently lower than the compression index (c_c) during first-time consolidation (Figure 3.8). Recompression index for the A-12 mud (T96) is 0.10; compression index is 0.27. Values for the A-20ST2 (T77) are 0.07 and 0.29, for c_r and c_c respectively. The A-14ST (T99) has the lowest recompression index of 0.05.

Velocity

Compressional wave velocity (v_p) was measured during K_0 experiments on the A-14ST, A-12 and A-20ST2 mud samples. Compressional waves at a frequency of 400 kHz were generated along the core axis (i.e. perpendicular to bedding). Measurements have an accuracy of ± 0.02 km/s (Karig, 1996). As vertical effective stress increases and the sediment compacts, v_p increases (Figure 3.9).

DISCUSSION

Assessment of consolidation state

We determine the maximum past stress experimentally by observing the change in deformation behavior during the experiment. Mud compaction is largely irreversible, because deformation is primarily plastic with a small elastic component. When a sample is brought from depth to the surface, it experiences a decrease in effective stress and a consequent rebound in void ratio (Figure 3.10, point 3). This rebound results from elastic expansion and opening of microcracks (Karig and Hou, 1992). As the sample is reloaded in the laboratory, the deformation path follows a slope similar to the unloading path, until the stress reaches the maximum past stress to which this sample has been subjected (Figure 3.10, point 4). Karig and Hou (1992) showed the similarity between the unloading and reloading deformation curves in laboratory experiments. Mesri and Choi (1985) demon-

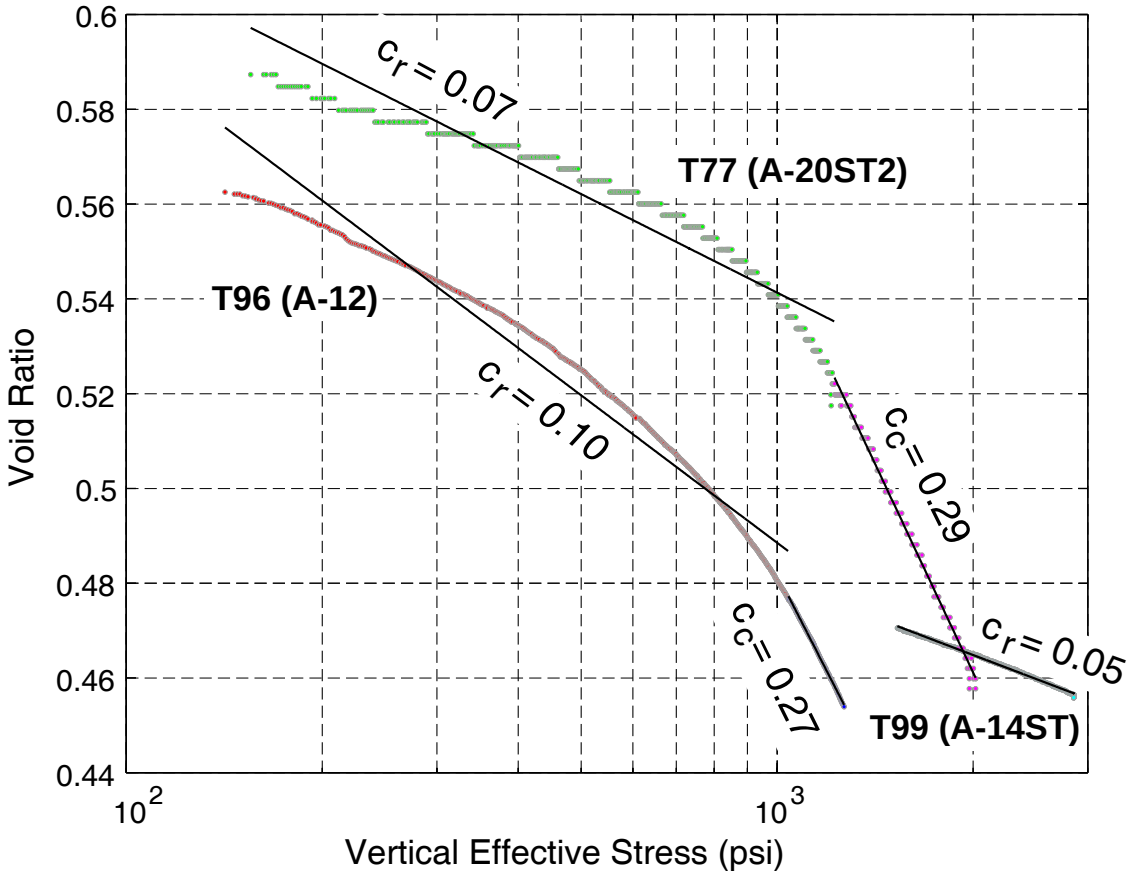

Figure 3.8: Compression index (c_c) is the slope of the void ratio- vertical effective stress curve during first-time consolidation. Recompression index (c_r), the slope during the reload phase, is less than c_c for each experiment.

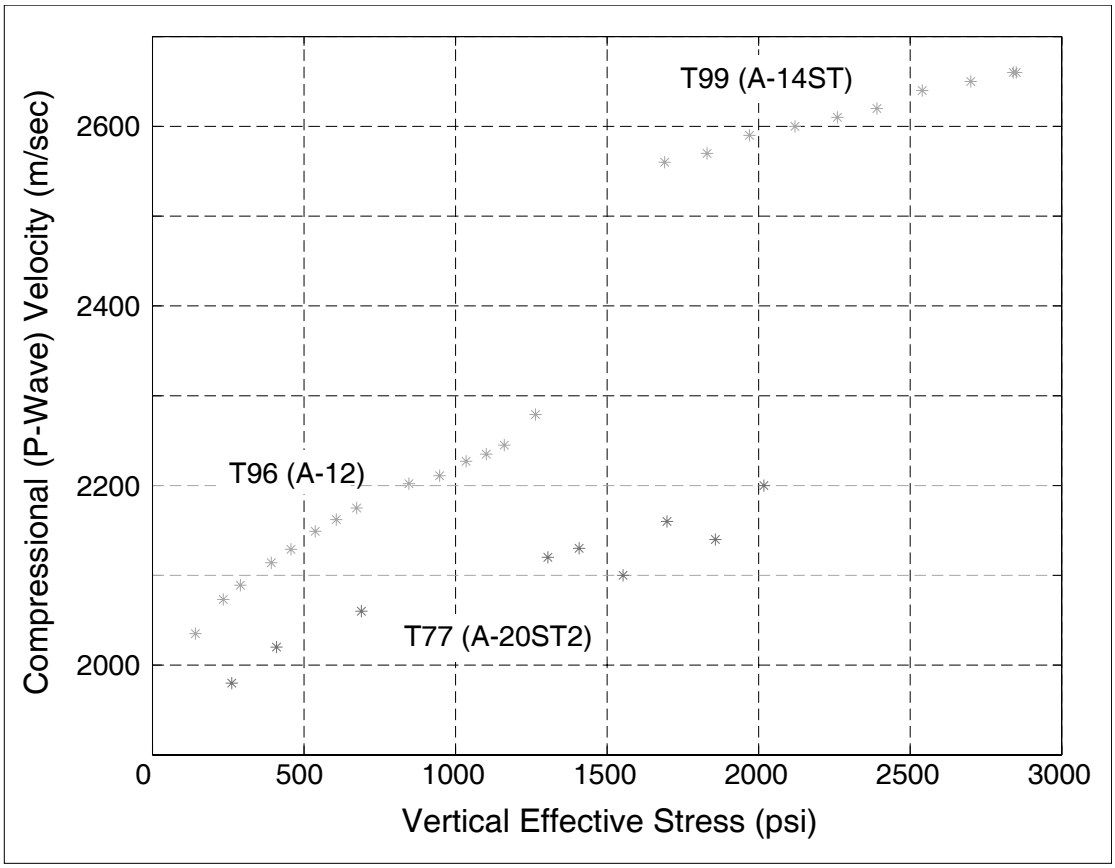

Figure 3.9: Compressional velocity increases with increasing vertical effective stress during all three K_0 tests.The change in velocity with vertical effective stress (i.e. the slope of linear regressions through these data) is 1.92 x 10^{-4} for the T96 (A-12), 1.04 x 10^{-4} for T77 (A-20ST2), and 8.71 x 10^{-5} for T99(A-14ST). The smaller slope of the A-14ST velocity-stress curve may be due to slower consolidation at higher effective stresses.

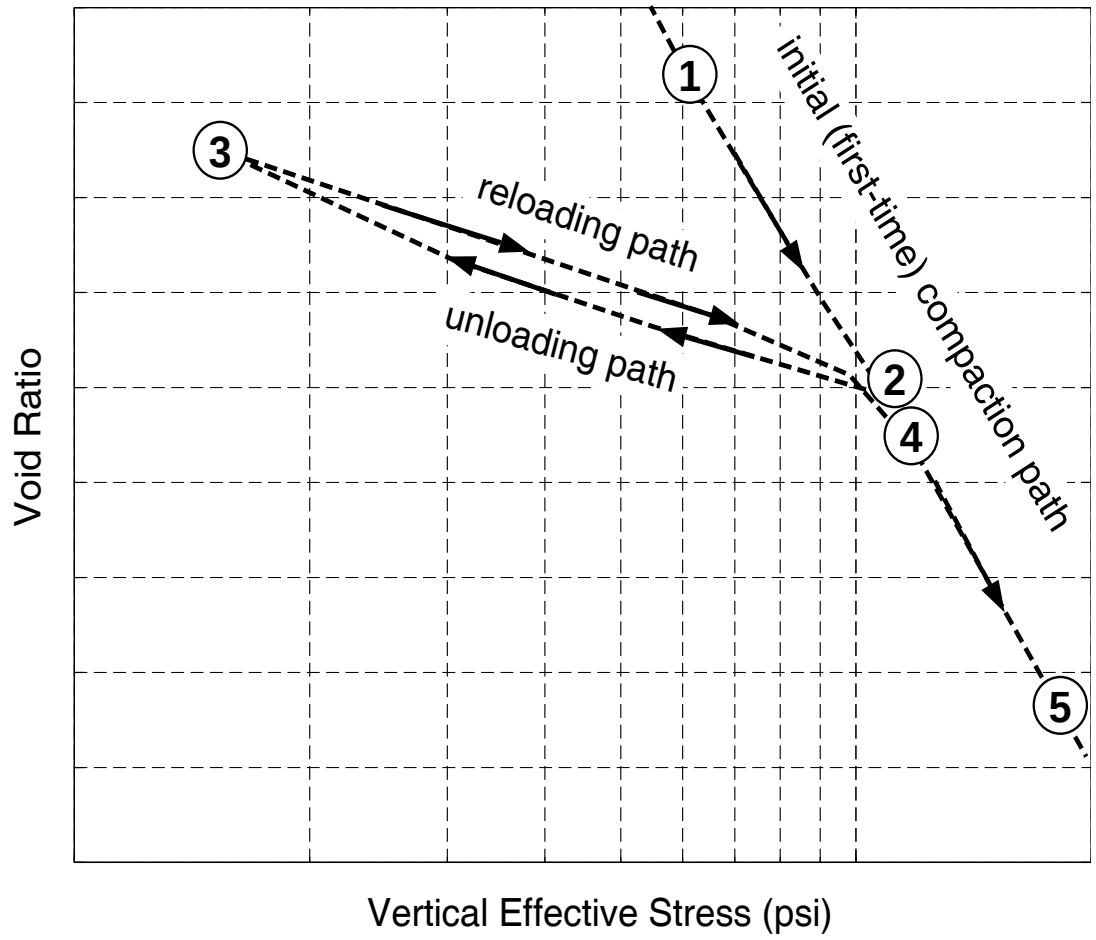

Figure 3.10: A generalized mud deformation path includes primary compaction (1 to 2). As effective stress decreases (2 to 3), sample experiences some porosity rebound, but does not decompact along the original deformation path. Upon reloading (3 to 4), sample will follow similar path until it reaches maximum past stress. Deformation at higher stresses (4 to 5) will track along a primary compaction path.

strated the uniqueness of the void ratio-effective stress relationship in determining maximum past stress experimentally. As the vertical effective stress increases past the maximum past stress, the slope of the void ratio-effective stress curve changes, reflecting a change from primarily elastic to primarily plastic deformation (Turcotte and Schubert, 1982; Atkinson, 1993). The plastic portion of the deformation is irreversible. On a traditional stress-strain plot, the elastic-plastic transition is manifested by a change from linear to non-linear behavior.

The comparison between laboratory-derived preconsolidation stress with *in situ* estimates of current vertical effective stress allows us to assess the consolidation state of the mud. A normally consolidated sediment has never been subjected to a higher stress than its current stress (Jones, 1994). An overconsolidated sediment is one which has been subjected to a greater effective stress than its current effective stress. The A-12 (T96) σ_c (7.2 MPa; 1046 psi) is within 0.2 MPa (25 psi) of the estimated *in situ* vertical effective stress (Table 3), indicating that this sediment is normally consolidated and therefore has experienced uni-directional strain.

The A-20ST2 sample appears to record a more complicated deformation path. The preconsolidation stress (e.g. maximum past vertical effective stress) of the A-20ST2 sample (8.6 MPa; 1248 psi) is approximately 1.4 MPa (200 psi) greater than the current *in situ* vertical effective stress. This difference implies that this sediment may have experienced a decrease in effective stress at depth.

The observation in the A-12 mud (T96) that σ_c is equal to the current *in situ* σ_v is of interest for several reasons. First, the water phase pressure in the overlying (Lentic 1 upper) sand (6.1 m above sample depth) is higher than the porosity-predicted fluid pres-

sure in the adjacent mud (Chapter 2; Stump and Flemings, 1998). The presence of fluid pressures in sand which are greater than predicted pressure in adjacent mud layers has been interpreted by some previous workers as evidence of unloading (Bowers, 1994; Hart et al., 1995). However, results from the uniaxial strain experiments on the A-12 mud imply that these sediments are currently at the maximum effective stress and therefore unloading (e.g. a late-stage decrease in effective stress) has not occurred. The A-20ST2 (T77) sample may be recording a more complicated deformation history (i.e. a decrease in vertical effective stress over time).

Cementation can strengthen a sample, increase the apparent preconsolidation stress of a sample, and be misinterpreted as overconsolidation. We attempt to assess the effects of cementation by cross-plotting mean effective stress ($p' = (2\sigma_h+\sigma_v)/3$) with differential stress ($q = \sigma_v - \sigma_h$) (Figure 3.11a). An uncemented, normally consolidated sediment (Figure 3.11a, dashed line) deforms along an approximately linear path in p'-q space, with a break in slope at sample yield. A cemented sample will likely show a decrease in differential stress for increasing mean effective stress, as cement breaks down (Figure 3.11a, dotted line). The deformation path of an overconsolidated, uncemented sample is not completely understood (Figure 3.11a, solid lines with question marks). The sample may demonstrate a constant differential stress for increasing mean effective stress, just prior to sample yield, or it may show only a slight increase in differential stress at the onset of deformation.

We plot results from the mud experiments (T99, T96, T77) in p'-q space to attempt to differentiate between effects of cementation and overconsolidation (Figures 3.11b,c,d). The A-12 signature (Figure 3.11b) appears to record an uncemented, normally consoli-

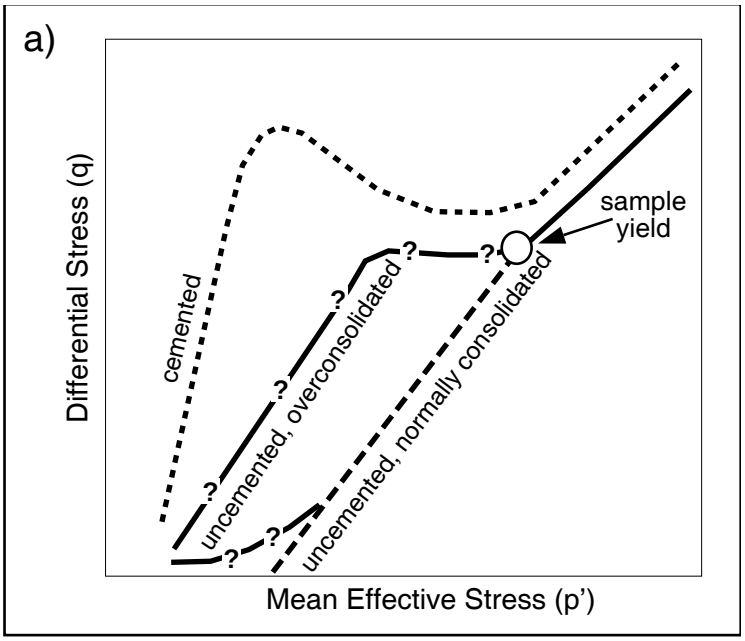

Figure 3.11: Cross-plots of mean effective stress (p') with differential stress (q) can illuminate the difference between cementation and a state of overconsolidation. a) A generalized figure (adapted from Karig, 1996) shows the p'-q signatures for cemented, uncemented normally consolidated, and uncemented overconsolidated sediments. b) A-12 (T96) sample shows a bilinear deformation path, indicative of uncemented, normally consolidated sediment.

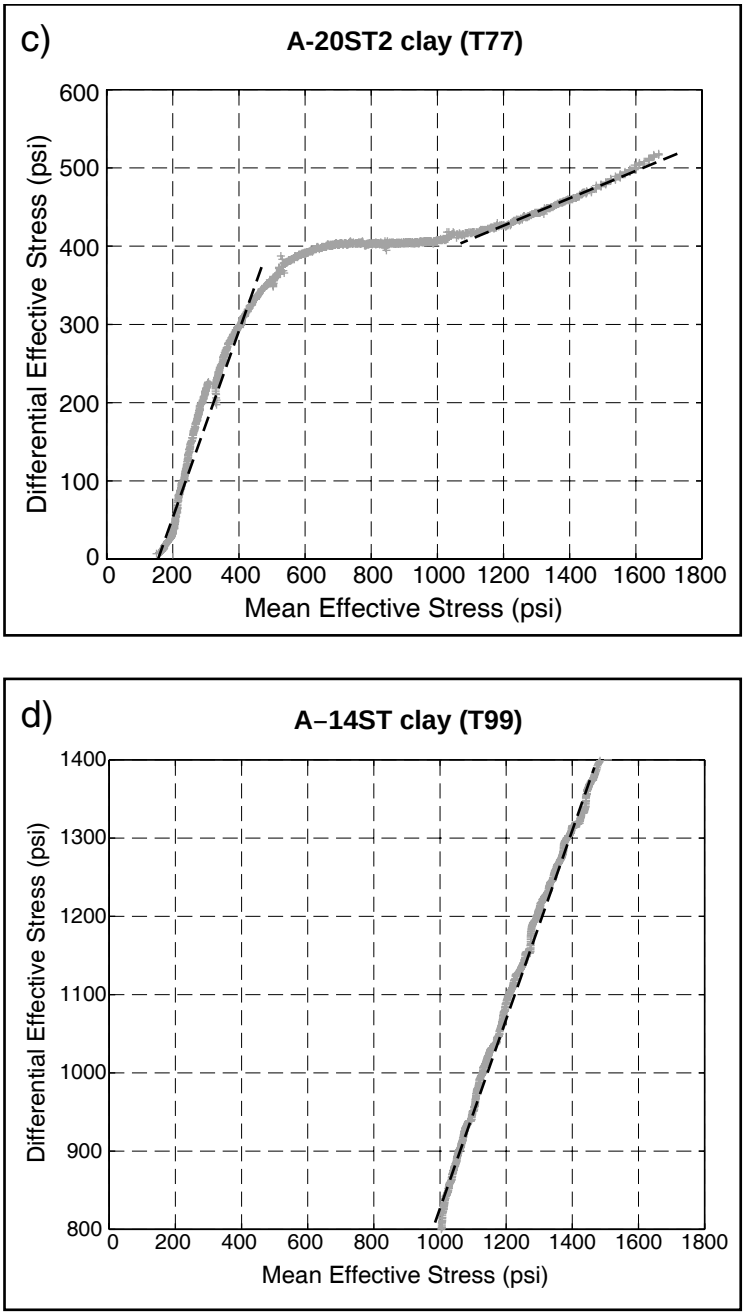

Figure 3.11: c) The A-20ST2 (T77) p'-q signature suggest that this sample may be overconsolidated, although cementation may be affecting deformation behavior. d) The A-14ST (T99) behavior is linear in p'-q space. This plot is inconclusive because the experiment was halted prior to sample yield.

dated path (i.e. bilinear with a break in slope at yield). The A-20ST2 p'-q signature (Figure 3.11c) appears to correlate well with one of the possible signatures for an overconsolidated sediment (Figure 3.11a). There is no marked decrease in differential stress, coincident with the breakdown of cementation. Mineralogical analyses of the A-12 and A-20ST2 did not indicate the presence of significant calcite cement (Core Laboratories, 1994; Losh et al., 1994), but also did not rule out the presence of authigenic clay. The A-14ST (T99) plot (Figure 3.11d) is inconclusive, because the experiment was not run to sample yield. Specific information about cement in the A-14ST core was not available.

Bryant et al. (1986a) suggest that the Casagrande method may underpredict the maximum past stress by as much as 35%. They propose an alternative method of computing regressions through the rebound and first-time compaction curves; the intersection of the two lines identifies the maximum past stress. However, Blum et al. (1996) observed no systematic difference between the Casagrande and Bryant methods in determining the preconsolidation stress of their samples.

Casagrande (1936) developed the graphical method for predicting preconsolidation stress from vertical effective stress and void ratio for use with traditional oedometer tests. During these tests, a limited number of parameters are measured. Wood (1990) presented other methods of constraining σ_c when more data are available. A 'yield surface', rather than a discrete point, can be identified using all three principal effective stresses (rather than one principal stress used in the Casagrande method).

A few potential sources of error are inherent in our calculations. First, we assume that geologic deformation is approximately uniaxial. Following this assumption, we consider uniaxial strain experiments to be a replication of sediment burial in a geologic basin,

and therefore presume the experimental yield stress to be indicative of the maximum past stress. In an extensional basin such as the Eugene Island 330 area, an assumption of uniaxial strain may cause the maximum past vertical effective stress observed in the laboratory to differ from the *in situ* maximum past vertical effective stress.

Second, we assume that the deformation experiments are run under drained conditions. That is, we assume that strain rates are sufficiently slow to allow excess fluid pressure to dissipate, such that the fluid pressure in the sample is constant. If this assumption is invalid, we are overestimating effective stress for a given porosity. Preliminary calculations indicate that for an average strain rate of 1×10^{-7} s^{-1} in a sample with permeability of 1×10^{-19} m^2 (1×10^{-4} mD), accumulated excess pressure is negligible ($P_f/S_v < 0.05$). As the A-12 mud permeability measurements are in the range of 1×10^{-19} m^2, we consider all of these tests to be representative of drained behavior.

Stress ratio, K_0

Lateral strain in normally-faulted basins such the E.I. 330 area can affect *in situ* stress ratio, by decreasing horizontal effective stress. Even if geologic strain is truly uniaxial, care should be taken when comparing laboratory-derived stress ratios with *in situ* measurements. Stress history can affect *in situ* σ_h, thereby changing the *in situ* stress ratio (Karig, 1996). A decrease in vertical effective stress will cause a decrease in horizontal effective stress, but the change in σ_h will not be equal to the change in σ_v. Therefore, the unloaded stress ratio will differ from the first-time consolidation stress ratio.

We compare K_0 calculated during deformation experiments to *in situ* measurements of stress ratio in the E.I. 330 area. We calculate stress ratio using measurements of

σ_h (from stress tests, leak-off tests, and fracture completions) and σ_v calculated from the wireline bulk density log and porosity-derived estimates of fluid pressure (Chapter 2). The post-σ_c K_0 values for the A-12 (T96) and A-20ST2 (T77) samples agree well with *in situ* stress ratios calculated from leak-off and stress test data.

A stress test in the A-20ST2 well provided an *in situ* estimate of horizontal effective stress, σ_h (Flemings et al., 1994). The measured *in situ* stress ratio in the A-20ST2 well is 0.84, which is nearly identical to the post-yield K_0 value (0.85). A leak-off test close to the A-12 well, provided a calculated *in situ* stress ratio at sample depth of 0.91 (Finkbeiner, 1998; Finkbeiner et al., in review). This *in situ* stress ratio is slightly higher than the experimental K_0 of 0.86. Stress ratio calculated from a fracture completion in the Lentic 1 sand adjacent to the A-12 cored interval is 0.43 (Finkbeiner, 1998), which is equivalent to the experimentally-derived K_0 value in the A-12 sand (C43).

As stated in Karig and Hou (1992), stronger sediments (i.e. sands) often have lower measured K_0 values, because they are capable of withstanding higher differential stresses. The observation that K_0 is greater in muds than in adjacent sands is very significant for drillers and completionists, because it implies that a fracture propagated within a sand will be contained by the mud. The mud K_0 values measured in our experiments are slightly higher than values of K_0 presented in previous studies (Table 4).

Both the A-12 and the A-20ST2 mud samples showed an increase in K_0 following yield. The sharp increase following yield results from a change in deformation. Prior to yield, during the reloaded phase, deformation is recoverable (elastic). Following yield, as the sample consolidates along its first-time compaction path, deformation is mostly plastic. Karig and Hou (1992) measured K_0 values of 0.35 and 0.62 for the elastic and first-

time consolidation phases of deformation in silty clays. A sand K_0 test revealed ratios of 0.21 and 0.53 for elastic and first-time consolidation, respectively (Karig and Hou, 1992).

In isotropic sediments, during elastic deformation under uniaxial strain conditions, stress ratio is a direct function of Poisson ratio. We recognize the anisotropy of clays, but estimate an average Poisson ratio using experimental K_0. Equation 3.13 is derived from Hooke's Law.

$$K_0 = \frac{\Delta\sigma_h}{\Delta\sigma_v} = \frac{\nu}{1-\nu} \tag{3.13}$$

By rearranging, we calculate the Poisson ratio of these samples from the experimental K_0 measured during the reload (elastic) phase of consolidation.

$$\nu = \frac{K_0}{1+K_0} \tag{3.14}$$

In the A-12 sample the K_0 of the reloaded phase is 0.52, corresponding to a Poisson ratio of 0.34. Dynamic Poisson ratio, calculated from a wireline dipole sonic tool at the depth of the A-12 mud sample, is 0.39.

In the A-20ST2, the pre-σ_c K_0 of 0.63 corresponds to a Poisson ratio of 0.39. Poisson ratio measured during a uniaxial stress test on a mud sample from the A-20ST2 well (Karig, pers. comm.) was 0.35.

The A-14ST K_0 value (0.37) suggests a Poisson ratio of 0.27. The difference between the A-14ST K_0 and those of the A-12 and A-20ST2 samples may be partially due to the fact that the A-14ST sample was not run to the sample's preconsolidation stress. As shown by Figures 3.6a,b, in the A-12 (T96) and A-20ST2 (T77), K_0 increased as σ_v approached σ_c.

.

Table 3.4: Comparison of post-yield K_0 values with previous work

Sediment type	Composition	K_0
A-12 mud (this study)	38% quartz, 39% clay, some potassium feldspar, plagioclase, calcite	0.86
A-20ST2 mud (this study)	35% quartz, 54% clay	0.85
Ottawa sand mixture (Karig and Hou, 1992)	90% quartz, 10% clay	0.53
silty clay (Karig and Hou, 1992)	50% silica powder (incl. quartz, potassium feldspar), 50% clay	0.62
Boston Blue Clay (Mesri and Hayat, 1993)	35% quartz, 30% clay, 23% plagioclase, 8% potassium feldspar	0.56
St. Alban clay (Mesri and Hayat, 1993)	25% quartz, 26% clay, 33% plagioclase, 11% potassium feldspar	0.49
Bearpaw Shale (Brooker and Ireland, 1965)	30% quartz, 65% clay, 5% potassium feldspar	0.70
London Clay (Brooker and Ireland, 1965)	15% quartz, 85% clay	0.67
Weald Clay (Brooker and Ireland, 1965)	30% quartz, 70% clay	0.54
Goose Lake Flour (Brooker and Ireland, 1965)	25% quartz, 75% clay	0.51

Permeability

Permeability calculations (5.32 x 10^{-4} mD, 1.17 x 10^{-4} mD) from constant head tests on samples from the A-12 well fall in the range of measurements made in previous studies (Figure 3.12). Dewhurst et al. (1998) measured an average permeability of 7.5 x 10^{-3} mD (7.4 x 10^{-18} m^2) for a silt-rich (40% clay) sample with 34% porosity. Measurements of permeability during consolidation tests on deepwater core from the Pigmy Basin, Gulf of Mexico yielded an average value of 3 x 10^{-4} mD (3 x 10^{-19} m^2) (Bryant et al., 1986b). Wetzel (1990) measured an average permeability of 8.6 x 10^{-3} mD (8.5 x 10^{-18} m^2) for turbidites taken from several hundred feet below the sea floor. Bryant et al. (1975) evaluated permeability from consolidation tests on various Gulf of Mexico sediments. For samples with composition and porosity similar to our samples, permeability ranged from 6.6 x 10^{-4} (6.5 x 10^{-19} m^2) to 9.6 x 10^{-4} mD (9.5 x 10^{-19} m^2) (Bryant et al., 1975).

The ratio of layer-parallel to layer-perpendicular permeability (4.5 for our data) may be due to the anisotropy of the mud. Vasseur et al. (1995) showed the difference between layer-parallel and layer-perpendicular permeabilities to increase for increasing levels of compaction. Taylor and Fisher (1993) also observed anisotropy in their permeability measurements of sediments from the Nankai accretionary prism.

Falling head and flow-pump tests are alternative methods for directly determining permeability. Olsen et al. (1985) prefer the flow pump method, because it generates a more easily distinguishable steady-state flow phase. The flow pump method also allows the measurement of permeability at various flow rates, which makes deviations from Darcy flow more apparent. These tests are also faster than constant or falling head tests and can be run with much lower gradients (Olsen et al., 1985). Tavenas et al. (1983) prefer

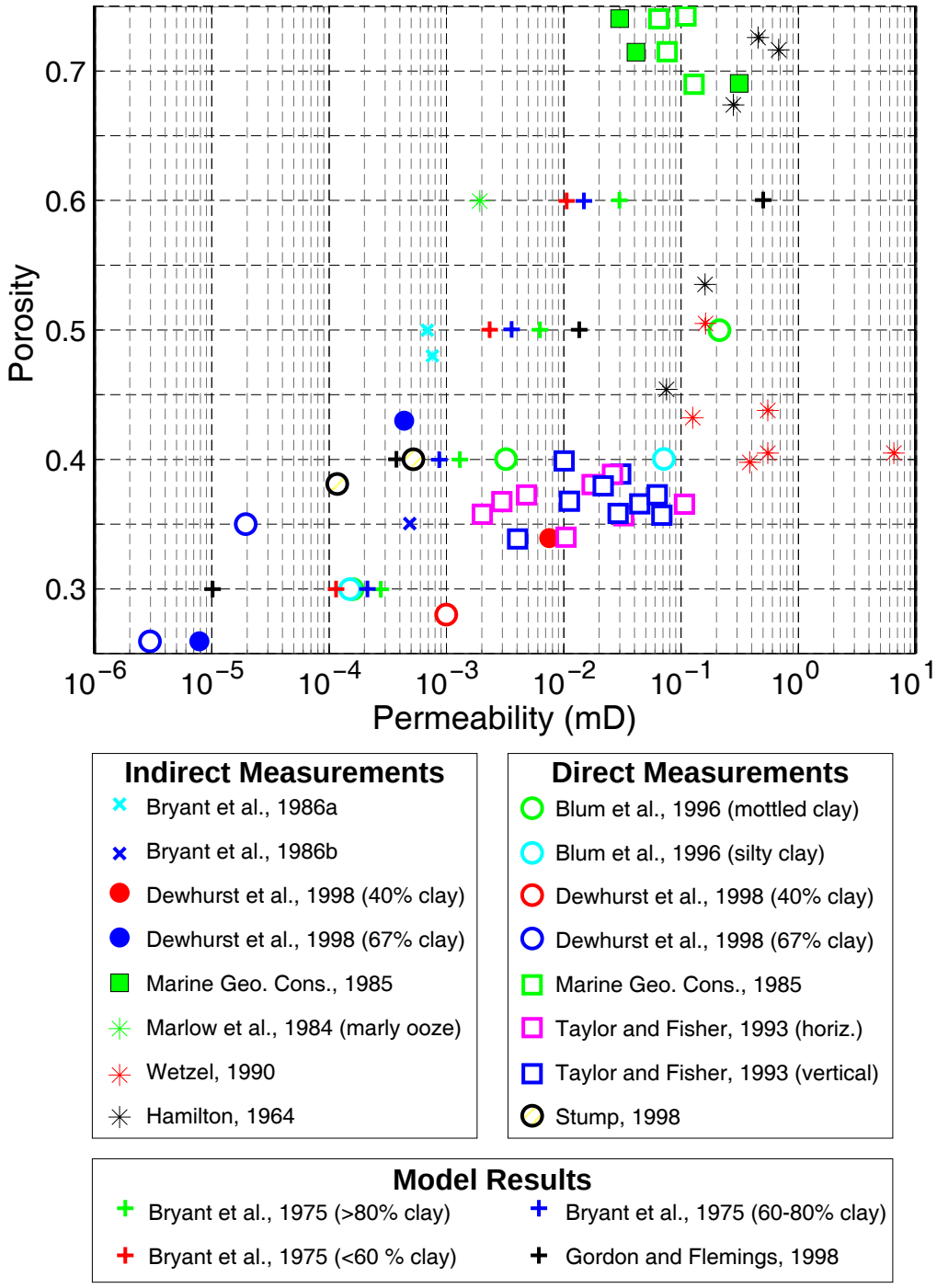

Figure 3.12: Comparison plot of porosity-permeability data published by previous authors shows that our permeability measurements (black circles) compare well with previous measurements made in similar sediments. Plus symbols (+) represent modeled results from Bryant et al. (1986a) and Gordon and Flemings (1998) for Gulf of Mexico muds. Indirect permeability measurements, made during consolidation tests are shown as asterisks (*), x's, and filled symbols. Empty symbols denote direct measurements of permeability (constant head and flow pump tests).

the falling head method in an oedometer to the constant head test, because the former is simpler, faster, and equally reliable.

Dewhurst et al. (1998) observed that direct measurements of permeability are generally 2 to 4 times lower than values estimated from consolidation tests. Consolidation-derived permeability is an average taken over a range of porosity values, while direct permeability is measured at the end of a load increment (i.e. at the compacted porosity only) (Dewhurst et al., 1998). Taylor and Fisher (1993) observed that their direct measurements of permeability exceeded values calculated from indirect methods by approximately an order of magnitude. As Mesri and Olson (1971) describe, the Terzaghi indirect method of permeability determination attributes all resistance to flow to permeability. If other factors impede flow, the consolidation (indirect) method will underestimate actual permeability (Mesri and Olson, 1971).

Regional *in situ* permeability may exceed laboratory estimates of permeability because of the influence of fractures. Neuzil (1994) recognized the differences between laboratory and regional estimates for Pierre shale and clay till, but also observed that several muds showed very similar values for laboratory and regional permeability.

The transformation from smectite to illite could also contribute to a decrease in permeability over time (Bethke, 1986). Therefore, *in situ* permeability is directly related to clay content and mineralogy.

Compression Index

The observed difference in c_c measurements for the A-20ST2 (T77) and A-12 (T96) samples may be attributed to differences in clay content. The A-12 sample contains

39% clay and records a c_c of 0.27. The A-20ST2 has a higher clay content of 54% and records a higher c_c (0.29).

Recompression indices (c_r) for the A-12 (T96) and A-20ST2 (T77) are less than compression indices (c_c) for those samples. The relationship between c_c and c_r is controlled by how much a sample swells during unloading. Miller et al. (1998) discuss *in situ* deformation paths resulting from unloading. Dewhurst et al. (1998) observed that clay-rich samples swell more (i.e. have a higher c_r) than quartz-rich samples. However, we do not observe this relationship in our samples. The sample with a higher clay content, A-20ST2 (T77), has a lower c_r than the A-12 (T96) sample (0.10).

Compression index calculated from a wireline mud porosity-effective stress analysis in the E.I. 330 area (Stump and Flemings, 1998) is 0.5, significantly greater than the laboratory-derived c_c for similar sediment. The higher compressibility calculated from the wireline relationship may be due to time-related effects. Over geologic time-scales, secondary consolidation and creep contribute to sediment compaction.

Velocity

The porosity-velocity relationships from these deformation experiments (Figure 3.13) correlate well with a relationship developed by Raymer et al. (1980) and enhanced by Raiga-Clemenceau et al. (1986).

$$\phi = 1 - \left(\frac{\Delta t_{ma}}{\Delta t}\right)^{1/f} \tag{3.15}$$

Issler (1992) calculated an acoustic formation factor, f, of 2.19 and a Δt_{ma} of 67 μs/ft for non-calcareous, low TOC shale. As shown by Figure 3.13, values calculated during our K_0 tests on the A-12 and A-20ST2 mud samples correlate well with Issler's (1992)

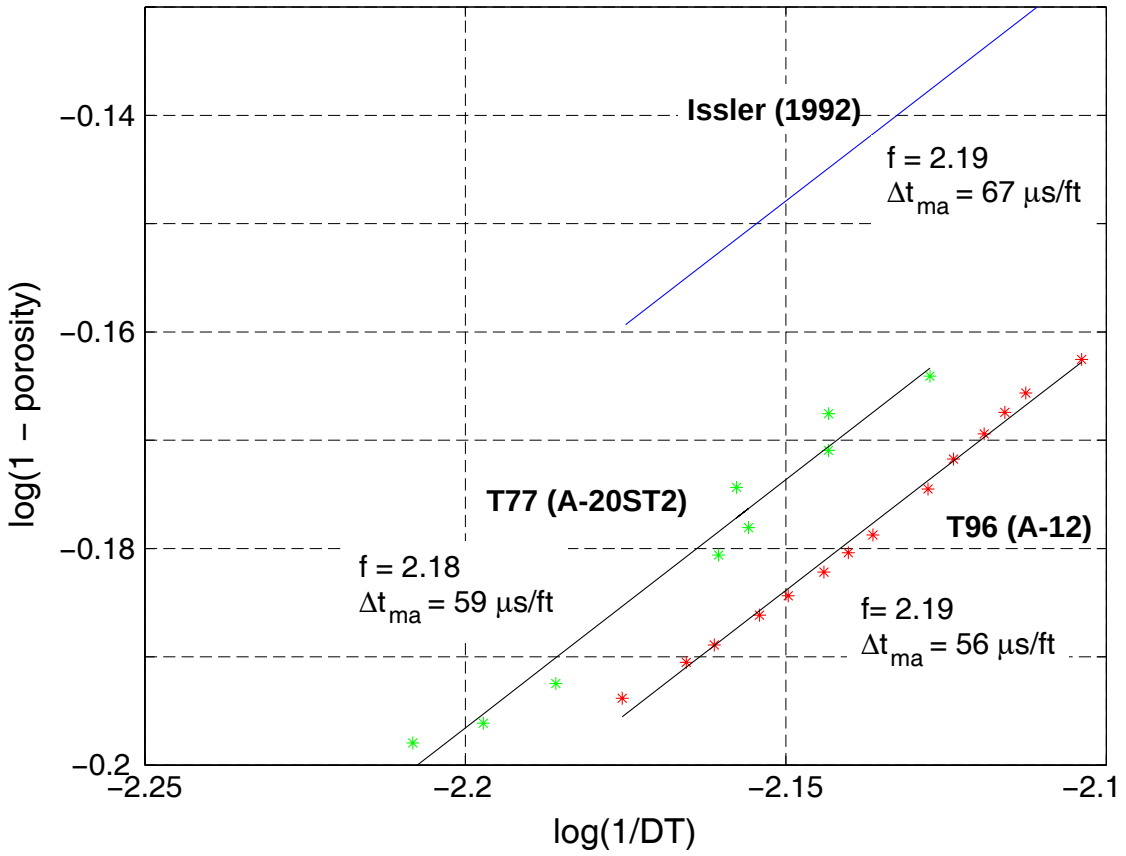

Figure 3.13: Cross-plot of porosity and compressional velocity data, for the determination of acoustic formation factor (f) and matrix velocity (Δt_{ma}) (Equation 3.15). Specifically, the slope of the regression line is 1/f. The y-intercept of the line is equal to (1/f)*log (Δt_{ma}). Linear regression of the T77 (A-20ST2) data reveals f = 2.18, Δt_{ma} = 59 μs/ft, with a correlation coefficient (R^2) of 0.9850. T96 (A-12) data yields an f of 2.19, Δt_{ma} of 56 μs/ft, and R^2 = 0.9962. For reference, Issler's (1992) relationship is shown.

values.

CONCLUSIONS

Deformation experiments conducted on two mud samples from the Eugene Island 330 area may suggest two different consolidation states for these sediments. The A-20ST2 uniaxial strain experiment shows possible evidence of an *in situ* decrease in vertical effective stress, implying that fluid pressure increased following compaction. However, the A-12 sample shows no evidence of a decrease in vertical effective stress. Experimental stress ratios following sample yield correlate well with *in situ* measurements. Constant head tests reveal mud permeability estimates of 5.32×10^{-4} and 1.17×10^{-4} mD.

ACKNOWLEDGMENTS

This research is supported by the Gas Research Institute (Contract # 5095-260-3558). I would like to thank Pennzoil and Texaco for donating the core used in these experiments. The A-20ST2 (Pathfinder) core was retrieved by the Global Basins Research Network (funded by DOE and industry partners). I would especially like to thank Dan Karig for both conducting these experiments and for critically reviewing this paper.

REFERENCES

Alexander, L.L., and P.B. Flemings, 1995, Geologic evolution of a Plio-Pleistocene salt-withdrawal minibasin: Eugene Island Block 330, offshore Louisiana: American Association of Petroleum Geologists Bulletin, v. 79, p. 1737-1756.

Atkinson, J., 1993, An introduction to the mechanics of soils and foundations: McGraw Hill, New York, 337 pp.

Bethke, C.M., 1986, Inverse hydrologic analysis of the distribution and origin of Gulf

Coast-type geopressured zones: Journal of Geophysical Research, v. 91, p. 6535-6545.

Blum, P., J. Xu, and S. Donthireddy, 1996, Geotechnical properties of Pleistocene sediments from the New Jersey upper continental slope, *in* G.S. Mountain, K.G. Miller, P. Blum, C.W. Poag, and D.C. Twichell, Eds., Proc. of the ODP, Scientific Results: College Station, TX, Ocean Drilling Program, v. 150, p. 377-384.

Bowers, G.L., 1994, Pore pressure estimation from velocity data: Accounting for overpressure mechanisms besides undercompaction: Society of Petroleum Engineers, SPE 27488, p. 515-529.

Brooker, E.W., and H.O. Ireland, 1965, Earth pressures at rest related to stress history: Canadian Geotechnical Journal, v. II, 1-15.

Bryant, W.R., W. Hottman, and P. Trabant, 1975, Permeability of unconsolidated and consolidated marine sediments, Gulf of Mexico: Marine Geotechnology, v. 1, p. 1-14.

Bryant, W., A. Wetzel, E. Taylor, and W. Sweet, 1986a, Consolidation characteristics and permeability of Mississippi fan sediments, *in* A.H. Bouma, J.M. Coleman, A.W. Meyer, et al., Eds., Init. Repts. DSDP 96: Washington, D.C., Government Printing Office, p. 797-809.

Bryant, W., A. Wetzel, and W. Sweet, 1986b, Geotechnical properties of intraslope sediments, Gulf of Mexico, Deep Sea Drilling Project Leg 96, Site 619, *in* A.H. Bouma, J.M. Coleman, A.W. Meyer, et al., Eds., Init. Repts. DSDP 96: Washington D.C., Government Printing Office, p. 797-809.

Casagrande, A., 1936, The determination of the pre-consolidation load and its practical significance: 1st Int. Conf. Soil Mech., Cambridge, Mass., v. 1, p. 60-64.

Core Laboratories, 1994, Sedimentology and Petrology, Conventional Core, No. A12 Well, Eugene Island Block 316: Reservoir Geology File No. 194117.

Dewhurst, D.N., A.C. Aplin, J-P. Sarda, and Y. Yang, 1998, Compaction-driven evolution of porosity and permeability in natural mudstones: Journal of Geophysical Research, v. 103, p. 651-661.

Finkbeiner, T., 1998, In situ stress, pore pressure, and hydrocarbon migration and accumulation in sedimentary basins, Ph.D. dissertation, Stanford University.

Finkbeiner, T., M. Zoback, B. Stump, and P. Flemings, in review, Stress, pore pressure, and dynamically constrained hydrocarbon columns in the South Eugene Island Field, Gulf of Mexico.

Flemings, P., M.D. Zoback, B.A. Bishop, and R.N. Anderson, 1994, State of stress in the Pathfinder Well, *in* R.N. Anderson, Ed., Global Basins Research Network Data Volume: Global Basins Research Network, part IV, Chapter 3, 548-586.

Gordon, D.S., and P.B. Flemings, 1998, Generation of overpressure and compaction-driven fluid flow in a Plio-Pleistocene growth-faulted basin, Eugene Island 330, offshore Louisiana: Basin Research, v. 10, p. 177-196.

Hamilton, E.L., 1964, Consolidation characteristics and related properties of sediments from experimental Mohole (Guadalupe site): Journal of Geophysical Research, v. 69, p. 4257-4269.

Hart, B.S., P.B. Flemings, and A. Deshpande, 1995, Porosity and pressure: Role of compaction disequilibrium in the development of geopressures in a Gulf Coast Pleistocene basin: Geology, v. 23, p. 45-48.

Issler, D.R., 1992, A new approach to shale compaction and stratigraphic restoration, Beaufort-Mackenzie basin and Mackenzie Corridor, northern Canada: American Association of Petroleum Geologists Bulletin, v. 76, p. 1170-1189.

Jacob, C.E., 1949, Flow of ground water, *in* H. Rouse, Ed., Engineering Hydraulics: New York, John Wiley and Sons, Inc.

Jones, M., 1994, Mechanical principles of sediment deformation, *in* A. Maltman, The geological deformation of sediments: Chapman and Hall, New York, p. 37-71.

Karig, D.E. and G. Hou, 1992, High-stress consolidation experiments and their geologic implications: Journal of Geophysical Research, v. 97, p. 289-300.

Karig, D.E. and J. Morgan, 1994, Tectonic deformation: stress paths and strain histories, *in* A. Maltman, The geological deformation of sediments: Chapman and Hall, New York, pp. 167-204.

Karig, D.E., 1996, Uniaxial reconsolidation tests on porous sediments: mudstones from Site 897 *in* R.B. Whitmarsh, D.S. Sawyer, A. Klaus, and D.G. Masson, Eds., Proceedings of the Ocean Drilling Program, Scientific Results: College Station, TX, Ocean Drilling Program, p. 363-373.

Losh, S., L. Eglinton, and J. Wood, 1994, Coring and inorganic geochemistry in the Pathfinder Well *in* R.N. Anderson, Ed., Global Basins Research Network Data Volume: Global Basins Research Network, Part III, Chapter 1, p. 183-194.

Marine Geotechnical Consortium, 1985, Geotechnical properties of northwest Pacific pelagic clays: Deep Sea Drilling Project Leg 86, Hole 576A, *in* G.R. Heath, L.H. Burckle, et al., Eds., Init. Repts. DSDP, 86: Washington, D.C., Government

Printing Office, p. 723-758.

Marlow, M.S., H.J. Lee, and A.W. Wright, 1984, Physical properties of sediments from Lesser Antilles margin along the Barbados Ridge: results from DSDP Leg 78A: Init. Repts. DSDP 78A, *in* B. Biju-Duval, J.C. Moore, et al. Eds.: Washington D.C., Government Printing Office, p. 549-558.

Mesri, G., and Y.K. Choi, 1985, The uniqueness of the end-of-primary (EOP) void-ratio effective stress relationship: Proc. of the 11th Internatl. Conf. on Soil Mech. and Foundation Eng., v. 2, p. 587-590.

Mesri, G., and T.M. Hayat, 1993, The coefficient of earth pressure at rest: Canadian Geotechnical Journal, v. 30, p. 647-666.

Mesri, G., and R.E. Olson, 1971, Mechanisms controlling the permeability of clays: Clays and Clay Minerals, v. 19, p. 151-158.

Miller, T.W. C.H. Luk, D.L. Olgaard, 1998, The interrelationships between overpressure mechanisms and in situ stresses: American Association of Drilling Engineers industry forum on pressure regimes in sedimentary basins and their prediction, September 2-4, Lake Conroe, TX.

Neuzil, C.E., 1986, Groundwater flow in low-permeability environments: Water Resources Research, v. 22, p. 1163-1195.

Neuzil, C.E., 1994, How permeable are clays and shales?: Water Resources Research, v. 30, p. 145-150.

Olsen, H.W., R.W. Nichols, and T.L. Rice, 1985, Low gradient permeability measurements in a triaxial system: Geotechnique, v. 35, p. 145-157.

Raiga-Clemenceau, J., J.P. Martin, and S. Nicoletis, 1986, The concept of acoustic formation factor for more accurate porosity determination from sonic transit time data: SPWLA 27th Annual Logging Symposium Transactions, Paper G.

Raymer, L.L., E.R. Hunt, and J.S. Gardner, 1980, An improved sonic transit time-to-porosity transform: SPWLA 21th Annual Logging Symposium Transactions, Paper P.

Roegiers, J-C., 1989, Elements of Rock Mechanics *in* M.J. Economides, and K.G. Nolte, Eds., Reservoir Stimulation: New Jersey, Prentice Hall.

Stump, B.B. and P.B. Flemings, 1998, Sediment loading and resulting pressure differences between overpressured sands and bounding shales of the Eugene Island 330 field (offshore Louisiana): Gas Research Institute, GRI-97/0266.

Tavenas, F., P. Leblond, P. Jean, and S. Leroueil, 1983, The permeability of soft clays. Part I: Methods of laboratory measurement: Canadian Geotechnical Journal, v. 20, p. 645-660.

Taylor, E., and A. Fisher, 1993, Sediment permeability at the Nankai accretionary prism, Site 808, *in* I.A. Hill, A. Taira, J.V. Firth, et al., Eds., Proc. of the ODP, Scientific Results: College Station, TX, Ocean Drilling Program, v. 131, p. 235-243.

Taylor, P., 1948, Fundamentals of Soil Mechanics: New York, John Wiley and Sons, Inc.

Terzaghi, K., 1925, Principles of soil mechanics, II- Compressive strength of clay: Engineering News Record, v. 95, p. 796.

Turcotte, D.L., and G. Schubert, 1982, Geodynamics: Applications of Continuum Physics to Geological Problems: New York, John Wiley and Sons, 450 pp.

Vasseur, G., I. Djeran-Maigre, D. Grunberger, G. Rousset, D. Tessier, and B. Veide, 1995, Evolution of structural and physical parameters during experimental compaction: Marine and Petroleum Geology, v. 12, p. 941-954.

Wetzel, A., 1990, Consolidation characteristics and permeability of Bengal fan sediments drilled during Leg 116, *in* J.R. Cochran, D.A.V. Stow, et al., Eds., Proc. of the Ocean Drilling Program, Scientific Results: College Station, TX Ocean Drilling Program, p. 363-368.

Wood, D.M., 1990, Soil behaviour and critical state soil mechanics: New York, Cambridge University Press, 461 pp.

Appendix D: Results from T99 (A-14ST mud)

Time (hrs)	stm (fraction)	astrs (psi)	hstrs (psi)	dstrs (psi)	porosity (V/V)
0.034	0.00000	1520.318	732.072	788.247	0.320
0.255	0.00005	1529.838	740.663	789.175	0.320
0.489	0.00006	1531.289	738.863	792.426	0.320
0.755	0.00007	1532.914	738.558	794.356	0.320
0.989	0.00008	1534.351	738.442	795.909	0.320
1.255	0.00009	1536.267	738.471	797.795	0.320
1.489	0.00010	1537.587	737.398	800.190	0.320
1.755	0.00011	1538.966	737.630	801.336	0.320
1.989	0.00013	1540.446	737.847	802.599	0.320
2.255	0.00014	1541.897	737.310	804.587	0.320
2.489	0.00015	1543.261	736.498	806.763	0.320
2.755	0.00016	1544.901	736.280	808.621	0.320
2.989	0.00017	1546.381	736.512	809.869	0.320
3.255	0.00018	1547.861	736.309	811.538	0.320
3.489	0.00020	1549.240	735.453	813.787	0.320
3.755	0.00021	1550.894	735.555	815.325	0.320
3.989	0.00022	1552.331	734.248	818.083	0.320
4.255	0.00024	1553.898	733.799	820.100	0.320
4.489	0.00025	1555.349	734.089	821.261	0.320
4.755	0.00027	1556.859	734.307	822.552	0.320
4.989	0.00028	1558.281	735.090	823.191	0.320
5.255	0.00029	1560.022	734.858	825.164	0.320
5.489	0.00030	1561.198	735.598	825.600	0.320
5.755	0.00045	1562.881	735.772	827.109	0.320
5.989	0.00046	1564.274	735.293	828.981	0.320
6.255	0.00046	1565.972	735.700	830.258	0.320

Appendix D: Results from T99 (A-14ST mud)

Time (hrs)	stm (fraction)	astrs (psi)	hstrs (psi)	dstrs (psi)	porosity (V/V)
6.489	0.00047	1567.322	735.700	831.622	0.320
6.755	0.00047	1568.802	735.729	833.073	0.320
6.989	0.00048	1570.442	735.816	834.626	0.320
7.255	0.00049	1571.878	735.076	836.803	0.320
7.489	0.00050	1573.184	735.526	837.659	0.320
7.755	0.00051	1574.853	735.917	838.921	0.320
7.989	0.00052	1576.537	736.832	839.705	0.320
8.255	0.00053	1578.017	736.135	841.882	0.320
8.489	0.00054	1579.323	736.715	842.622	0.320
8.755	0.00055	1580.934	737.746	843.188	0.320
8.989	0.00056	1582.428	738.762	843.667	0.320
9.255	0.00057	1583.923	739.153	844.784	0.320
9.489	0.00058	1585.418	739.545	845.872	0.320
9.755	0.00060	1586.898	740.082	846.830	0.320
9.989	0.00060	1588.320	740.880	847.425	0.320
10.255	0.00062	1590.018	741.548	848.470	0.320
10.489	0.00063	1591.542	741.838	849.704	0.320
10.755	0.00064	1593.181	741.272	851.895	0.320
10.989	0.00065	1594.444	742.012	852.446	0.320
11.255	0.00066	1595.982	742.027	853.955	0.320
11.489	0.00067	1597.520	741.969	855.552	0.320
11.755	0.00068	1599.117	742.012	857.105	0.320
11.989	0.00069	1600.336	742.578	857.758	0.320
12.255	0.00071	1602.164	742.941	859.223	0.320
12.489	0.00071	1603.514	744.015	859.499	0.320
12.755	0.00072	1605.023	745.103	859.920	0.320

Appendix E: Results from T77 (A-20ST2 mud)

Time	ε	σ_v (psi)	σ_h (psi)	q (psi)	p’ (psi)	ϕ	K_o
0.034	0.000	155.278	149.474	6.995	150.925	0.370	0.955
0.126	0.007	162.534	155.278	7.895	158.181	0.370	0.952
0.396	0.007	163.986	156.730	7.474	159.632	0.370	0.954
0.634	0.011	166.888	159.632	8.286	161.083	0.370	0.951
0.905	0.017	168.339	159.632	9.041	162.534	0.370	0.946
1.140	0.022	169.790	161.083	9.331	163.986	0.370	0.945
1.380	0.025	171.242	161.083	9.607	163.986	0.369	0.944
1.650	0.029	172.693	162.534	10.187	166.888	0.369	0.941
1.890	0.033	174.144	162.534	10.521	166.888	0.369	0.939
2.130	0.043	175.595	165.437	10.957	168.339	0.369	0.938
2.400	0.049	177.046	165.437	11.682	168.339	0.369	0.934
2.630	0.056	178.498	166.888	12.422	171.242	0.369	0.931
2.900	0.060	179.949	166.888	12.567	171.242	0.369	0.930
3.140	0.070	181.400	166.888	14.033	171.242	0.369	0.922
3.380	0.077	182.851	168.339	14.149	174.144	0.369	0.923
3.650	0.085	184.302	168.339	16.108	174.144	0.369	0.913
3.890	0.090	185.754	168.339	17.124	174.144	0.369	0.908
4.130	0.099	188.656	171.242	17.269	177.046	0.369	0.908
4.400	0.108	188.656	171.242	17.414	177.046	0.369	0.907
4.630	0.117	190.107	171.242	18.575	177.046	0.369	0.902
4.900	0.127	193.010	172.693	19.446	179.949	0.368	0.899
5.140	0.133	193.010	172.693	20.027	179.949	0.368	0.896
5.380	0.138	195.912	175.595	20.317	181.400	0.368	0.896
5.650	0.143	195.912	175.595	21.623	182.851	0.368	0.890
5.890	0.149	198.814	177.046	21.623	184.302	0.368	0.891

Appendix E: Results from T77 (A-20ST2 mud)

Time	ε	σ_v (psi)	σ_h (psi)	q (psi)	p’ (psi)	ϕ	K_o
6.130	0.154	198.814	177.046	22.203	184.302	0.368	0.889
6.400	0.161	200.266	177.046	22.929	184.302	0.368	0.885
6.630	0.167	201.717	178.498	23.364	187.205	0.368	0.884
6.900	0.172	204.619	181.400	23.800	188.656	0.368	0.884
7.140	0.177	204.619	181.400	24.235	188.656	0.368	0.882
7.380	0.181	206.070	181.400	24.961	188.656	0.368	0.879
7.650	0.189	208.973	182.851	25.831	191.558	0.368	0.877
7.890	0.196	208.973	182.851	26.122	191.558	0.368	0.875
8.130	0.195	211.875	184.302	26.702	194.461	0.367	0.874
8.400	0.193	211.875	185.754	27.573	194.461	0.367	0.870
8.630	0.195	214.778	187.205	28.008	195.912	0.367	0.869
8.900	0.202	216.229	187.205	29.604	197.363	0.367	0.863
9.140	0.207	217.680	187.205	30.040	197.363	0.367	0.862
9.380	0.212	217.680	187.205	30.765	197.363	0.367	0.859
9.650	0.219	220.582	188.656	31.926	200.266	0.367	0.855
9.890	0.224	222.034	188.656	33.232	200.266	0.367	0.851
10.100	0.232	223.485	188.656	33.958	200.266	0.367	0.848
10.400	0.240	224.936	188.656	35.409	200.266	0.367	0.842
10.600	0.246	224.936	188.656	36.135	200.266	0.367	0.839
10.900	0.251	226.387	188.656	37.586	201.717	0.367	0.834
11.100	0.256	229.290	191.558	38.892	204.619	0.367	0.831
11.400	0.259	230.741	191.558	39.763	204.619	0.367	0.828
11.700	0.265	232.192	191.558	41.069	204.619	0.367	0.823
11.900	0.270	233.643	191.558	42.375	204.619	0.367	0.818
12.100	0.274	235.094	191.558	43.971	206.070	0.367	0.813

Appendix F: Results from T96 (A-12 mud)

Time (hrs)	ε	ϕ	σ_v (psi)	σ_h (psi)	q (psi)	p’ (psi)
0.034	0.000	0.360	141.782	100.423	41.359	114.209
0.114	0.017	0.360	146.571	105.212	41.504	118.998
0.184	0.017	0.360	146.571	105.792	41.359	119.579
0.255	0.017	0.360	148.022	105.502	42.085	119.579
0.330	0.017	0.360	148.022	105.067	42.956	119.434
0.568	0.017	0.360	149.474	103.471	46.293	118.853
0.805	0.029	0.360	150.925	102.310	48.760	118.563
1.080	0.033	0.360	152.376	101.584	51.372	118.708
1.310	0.040	0.360	153.827	102.455	51.953	119.724
1.580	0.045	0.360	156.730	102.455	53.694	120.304
1.820	0.050	0.359	158.181	103.180	54.275	121.320
2.060	0.057	0.359	158.181	103.035	55.581	121.611
2.330	0.065	0.359	159.632	103.325	57.032	122.336
2.570	0.072	0.359	161.083	103.761	58.048	123.062
2.810	0.077	0.359	162.534	104.051	59.209	123.787
3.080	0.092	0.359	165.437	104.341	60.660	124.513
3.310	0.094	0.359	166.888	104.341	62.111	124.948
3.580	0.102	0.359	168.339	104.486	63.563	125.674
3.820	0.111	0.359	169.790	104.341	65.159	125.964
4.060	0.116	0.359	171.242	104.777	66.030	126.835
4.330	0.130	0.359	172.693	105.647	66.900	127.996
4.570	0.133	0.359	174.144	105.357	68.642	128.286
4.810	0.143	0.359	175.595	105.647	69.658	128.867
5.080	0.149	0.358	177.046	105.938	70.964	129.592
5.310	0.156	0.358	178.498	106.518	71.834	130.463

Appendix F: Results from T96 (A-12 mud)

Time (hrs)	ε	ϕ	σ_v (psi)	σ_h (psi)	q (psi)	p’ (psi)
5.580	0.164	0.358	179.949	106.953	72.995	131.334
5.820	0.182	0.358	181.400	106.808	74.592	131.624
6.060	0.183	0.358	182.851	106.953	75.753	132.204
6.330	0.192	0.358	184.302	106.953	77.349	132.640
6.570	0.201	0.358	185.754	107.244	78.510	133.365
6.810	0.208	0.358	187.205	107.534	79.526	134.091
7.080	0.216	0.358	188.656	108.260	80.687	135.107
7.310	0.228	0.358	190.107	107.969	82.428	135.397
7.580	0.238	0.358	193.010	108.550	83.734	136.413
7.820	0.247	0.357	193.010	108.840	84.750	136.993
8.060	0.252	0.357	194.461	108.260	86.056	136.993
8.330	0.261	0.357	195.912	108.405	87.507	137.574
8.570	0.277	0.357	197.363	108.985	88.233	138.444
8.810	0.278	0.357	198.814	109.856	89.684	139.751
9.080	0.288	0.357	201.717	109.856	91.135	140.331
9.310	0.296	0.357	203.168	110.001	92.587	140.766
9.580	0.304	0.357	204.619	110.001	94.183	141.347
9.820	0.322	0.357	206.070	110.146	95.344	141.927
10.100	0.324	0.357	207.522	110.436	96.505	142.653
10.300	0.334	0.357	208.973	110.291	98.246	142.943
10.600	0.341	0.357	210.424	111.742	98.246	144.540
10.800	0.348	0.356	211.875	111.452	99.843	144.685
11.100	0.357	0.356	213.326	112.033	100.858	145.120
11.300	0.363	0.356	214.778	112.323	101.874	146.571
11.600	0.377	0.356	216.229	112.613	103.325	146.571

Appendix G: P-Wave Measurements for T99 (A-14ST mud)

Travel time (μs)	ϕ
18.811	0.319
18.711	0.318
18.561	0.318
18.461	0.317
18.361	0.316
18.261	0.315
18.111	0.315
18.011	0.314
17.961	0.313
17.911	0.313
0.000	0.000

Appendix H: P-Wave Measurements for T77 (A-20ST2 mud)

ϕ	Travel time (μs)
0.0000	0.000
0.3699	0.000
0.3660	25.965
0.3634	25.315
0.3580	24.664
0.3402	23.264
0.3363	23.014
0.3306	23.114
0.3254	22.364
0.3201	22.363
0.3146	21.563

Appendix I: P-Wave Measurements for T96 (A-12 mud)

ϕ	Travel Time (μs)
0.3600	30.768
0.3551	30.068
0.3527	29.767
0.3486	29.287
0.3459	28.987
0.3426	28.617
0.3399	28.367
0.3374	28.117
0.3309	27.566
0.3266	27.316
0.3230	27.016
0.3199	26.816
0.3171	26.615
0.3122	26.087

Appendix J: Results from Permeability Test P01 (raw voltage data)

Time (hours)	ε (V)	σ_h (V)	Volume In (V)	σ_v (V)
0.035	4.139	-0.017	0.400	0.042
0.172	4.117	-2.515	0.400	0.091
0.406	4.094	-2.516	0.400	0.004
0.672	4.094	-2.517	0.400	0.004
0.906	-4.849	-2.547	-9.198	0.004
1.176	9.190	-4.994	-4.789	0.004
1.410	9.190	-4.996	-4.788	0.005
1.676	9.190	-4.996	-4.787	0.006
1.910	9.190	-4.996	-4.787	0.006
2.176	9.190	-4.996	-4.787	0.007
2.410	9.190	-4.996	-4.787	0.007
2.676	9.190	-4.997	-4.786	0.007
2.910	9.190	-4.998	-4.786	0.007
3.176	9.190	-4.999	-4.786	0.008
3.410	9.190	-5.001	-4.785	0.008
3.676	9.190	-5.000	-4.785	0.009
3.910	9.190	-5.001	-4.784	0.009
4.176	9.190	-5.002	-4.784	0.010
4.410	9.190	-5.003	-4.784	0.009
4.676	9.190	-5.004	-4.784	0.009
4.910	9.190	-5.003	-4.784	0.009
5.176	9.190	-5.004	-4.784	0.009
5.410	2.766	-5.006	-4.784	-0.753
5.681	2.700	-5.006	-4.785	-0.753
5.918	2.666	-5.006	-4.784	-0.753

Appendix J: Results from Permeability Test P01 (raw voltage data)

Time (hours)	ε (V)	σ_h (V)	Volume In (V)	σ_v (V)
6.156	2.637	-5.006	-4.784	-0.753
6.426	2.610	-5.008	-4.784	-0.753
6.664	2.588	-5.008	-4.784	-0.753
6.901	2.569	-5.007	-4.784	-0.753
7.172	2.547	-5.008	-4.784	-0.753
7.410	2.531	-5.008	-4.784	-0.753
7.681	2.513	-5.009	-4.784	-0.753
7.918	2.499	-5.010	-4.784	-0.753
8.156	2.486	-5.009	-4.783	-0.753
8.426	2.471	-5.009	-4.783	-0.753
8.664	2.458	-5.009	-4.783	-0.753
8.901	2.446	-5.009	-4.784	-0.753
9.172	2.432	-5.008	-4.784	-0.753
9.410	2.421	-5.008	-4.784	-0.753
9.681	2.410	-5.008	-4.784	-0.753
9.918	2.401	-5.009	-4.784	-0.753
10.156	2.394	-5.008	-4.784	-0.753
10.426	2.384	-5.009	-4.784	-0.753
10.664	2.376	-5.008	-4.784	-0.753
10.901	2.369	-5.010	-4.784	-0.753
11.172	2.359	-5.009	-4.784	-0.753
11.410	2.353	-5.009	-4.784	-0.753
11.681	2.346	-5.010	-4.784	-0.753
11.918	2.340	-5.010	-4.784	-0.753
12.156	2.335	-5.010	-4.784	-0.753

Appendix J: Results from Permeability Test P01 (raw voltage data)

Time (hours)	ε (V)	σ_h (V)	Volume In (V)	σ_v (V)
12.426	2.328	-5.010	-4.784	-0.753
12.664	2.322	-5.010	-4.784	-0.753
12.901	2.318	-5.010	-4.784	-0.753
13.172	2.312	-5.010	-4.784	-0.753

Appendix K: Results from Permeability Test P03 (raw voltage data)

Time (hours)	P_f (psi)	σ_v (V)	Volume In (v)	σ_h (V)	ε (V)
0.034	0.000	0.336	2.870	-3.044	3.217
0.234	0.000	-0.122	2.870	-3.998	2.648
0.505	0.000	-0.421	2.871	-3.996	2.457
0.743	0.000	-0.499	2.871	-3.995	2.373
0.980	0.000	-0.499	2.871	-3.995	2.338
1.251	0.000	-0.499	2.871	-3.996	2.316
1.489	0.000	-0.499	2.871	-3.996	2.305
1.759	0.000	-0.499	2.871	-3.997	2.295
1.997	0.000	-0.499	2.871	-3.997	2.289
2.234	0.000	-0.499	2.871	-3.996	2.283
2.505	0.000	-0.499	2.871	-3.997	2.281
2.743	0.000	-0.499	2.872	-3.998	2.278
2.980	0.000	-0.499	2.872	-3.996	2.275
3.251	0.000	-0.499	2.872	-3.997	2.271
3.489	0.000	-0.499	2.872	-3.997	2.268
3.759	0.000	-0.499	2.872	-3.998	2.265
3.997	0.000	-0.499	2.872	-3.998	2.263
4.234	0.000	-0.499	2.872	-3.998	2.260
4.509	35.000	-0.499	5.437	-3.997	2.261
4.747	35.000	-0.499	5.295	-3.997	2.261
4.984	35.000	-0.499	5.065	-3.998	2.256
5.255	35.000	-0.499	4.922	-3.998	2.257
5.493	35.000	-0.499	4.811	-3.998	2.249
5.730	35.000	-0.499	4.718	-3.996	2.248
6.001	35.000	-0.499	4.607	-3.997	2.244

Appendix K: Results from Permeability Test P03 (raw voltage data)

Time (hours)	P_f (psi)	σ_v (V)	Volume In (v)	σ_h (V)	ε (V)
6.239	35.000	-0.499	4.537	-3.998	2.241
6.509	35.000	-0.499	4.439	-3.997	2.240
6.747	35.000	-0.499	4.367	-3.997	2.239
6.984	35.000	-0.499	4.296	-3.998	2.241
7.255	35.000	-0.499	4.218	-3.998	2.240
7.493	35.000	-0.499	4.162	-3.998	2.238
7.730	35.000	-0.499	4.110	-3.997	2.239
8.001	35.000	-0.499	4.038	-3.998	2.238
8.239	35.000	-0.499	3.962	-3.998	2.235
8.509	35.000	-0.499	3.895	-3.998	2.232
8.747	35.000	-0.499	3.831	-3.998	2.235
8.984	35.000	-0.499	3.773	-3.997	2.235
9.255	35.000	-0.499	3.137	-3.998	2.235
9.493	35.000	-0.499	3.140	-3.999	2.232
9.730	35.000	-0.499	3.142	-3.998	2.234
10.001	35.000	-0.499	3.144	-3.998	2.233
10.239	35.000	-0.499	3.145	-3.998	2.234
10.509	35.000	-0.499	3.147	-3.997	2.234
10.747	35.000	-0.499	3.149	-3.998	2.231
10.984	35.000	-0.499	3.119	-3.998	2.230
11.255	35.000	-0.499	3.074	-3.998	2.233
11.493	35.000	-0.499	3.054	-3.999	2.233
11.730	35.000	-0.499	3.040	-4.000	2.234
12.001	35.000	-0.499	3.017	-4.000	2.232
12.239	35.000	-0.499	3.000	-4.000	2.231

Appendix K: Results from Permeability Test P03 (raw voltage data)

Time (hours)	P_f (psi)	σ_v (V)	Volume In (v)	σ_h (V)	ε (V)
12.509	35.000	-0.499	2.994	-4.000	2.230
12.747	35.000	-0.499	2.975	-4.000	2.231
12.984	35.000	-0.499	2.939	-4.000	2.230
13.255	35.000	-0.499	2.892	-4.000	2.230
13.493	35.000	-0.499	2.828	-3.999	2.232
13.730	35.000	-0.499	2.789	-3.999	2.232
14.001	35.000	-0.499	2.744	-3.999	2.231
14.239	35.000	-0.499	2.707	-3.999	2.232